

# Using Active Contours for Automated Tracking of UV and EUV Solar Flare Ribbons

Colin D. Gill



Presented for the degree of MSc  
Department of Pyhsics and Astronomy  
The University of Glasgow  
2009

# Declaration

This thesis is my own composition except where indicated in the text.  
1st August 2009.

# Acknowledgements

My first thanks go to Prof. John Brown and Dr. Lyndsay Fletcher for offering me a masters project within Glasgow University Astronomy & Astrophysics Group, without them both I would not be in postgraduate research right now, and for that they both have my greatest thanks. I would like to thank Dr. Lyndsay Fletcher for her supervision throughout the year, answering my many stupid questions and her seeming endless enthusiasm. My thanks also go to Prof. Stephen Marshall who has jointly supervised me, and has been my guru for active contours and all things image processing as well as providing programming help. Again without Prof. Marshall's willingness this Masters project would not have been possible.

I would like to thank Laura Robertson for her support, understanding and encouragement. Thanks to my office mates in 538, Iain Kendall, Luo Rui and Satoru Sakai, together with Hamish Reid and Hugh Potts for their programming help and general advice.

# Abstract

Solar flare UV and EUV images show elongated bright “ribbons” that move over time. If these ribbons are assumed to locate the footpoints of magnetic field lines reconnecting in the corona then it is clear that studying their evolution can provide an important insight into the reconnection process. We propose an image processing method based on active contours (commonly referred to as “snakes”), for tracking UV and EUV flare ribbons in images from the transition region and coronal explorer (TRACE). Our method aims to provide an efficient, accurate and automatic tool to aid in the study of flare ribbon evolution in large datasets.

Chapter 1 provides an introduction to the Sun and solar activity, with a more focussed section on solar flares where the mechanism for the creation of flare ribbons is discussed. We also outline the motivation for solar physics research as a whole and more specifically the motivations behind this project. In this chapter we introduce the TRACE satellite as the source the images used in this project, with a summary of its hardware and the UV and EUV channels which the images used in this project are captured in.

Chapter 2 introduces some basics of image processing, such as applying spatial filters. We also look at the different approaches to image segmentation including a more in depth study of active contours. The role of image processing in solar physics and the driving forces for image processing development in solar physics are summarised. The final section of this chapter presents a review of previous methods used for the tracking of solar flare ribbons, including manual, semi-automatic and fully automatic methods.

The first part of Chapter 3 details the pre-processing steps applied to the TRACE data before its use by our algorithm. The second part of this chapter introduces our algorithm, with a general overview and detailed discussion of the constituent parts. We also show results from initial tests carried out using a simulated test image, and demonstrate how different parameters of the algorithm can affect its result.

Chapter 4 shows results obtained from using our algorithm on TRACE flare images. Some modifications to the algorithm were deemed necessary after applying it to only a small number of flare images, the initial part of this chapter covers the reasons for the modifications and the modifications themselves. The remainder of the

chapter presents results of the algorithm applied to a number image sequences from different flares. The results are presented and discussed for each flare separately, with one flare being used as an example of how the parameters of the algorithm can be adapted to suit different flares and images.

Chapter 5 discusses to what extent the aim of the project has been achieved and presents a summary of the problems encountered in applying our algorithm to flare images. This chapter finishes with a look at some ideas for future work, both for our algorithm specifically, and for general efforts at flare ribbon tracking.

# Contents

<b>List of Figures</b>	<b>4</b>
<b>List of Tables</b>	<b>10</b>
<b>1 Introduction</b>	<b>11</b>
1.1 Solar Research Motivation . . . . .	12
1.2 Solar Structure . . . . .	13
1.3 Solar Flares . . . . .	15
1.3.1 GOES Classification of Solar Flares . . . . .	18
1.3.2 UV and EUV Ribbons in Two-Ribbon Flares . . . . .	19
1.4 The TRACE Mission . . . . .	22
1.4.1 TRACE Instrumentation . . . . .	23
1.4.2 TRACE Spectral Response . . . . .	25
1.5 Summary . . . . .	26
<b>2 Image Processing in Solar Physics</b>	<b>27</b>
2.1 Image Processing Background . . . . .	27
2.1.1 The Application of Image Processing Filters . . . . .	28
2.1.2 Image Segmentation . . . . .	31
2.1.3 Snakes: Active Contour Models . . . . .	35
2.2 Image Processing in Solar Physics . . . . .	38
2.2.1 Introduction . . . . .	38
2.2.2 Pre-processing and Enhancement . . . . .	39
2.2.3 Automatic Feature Detection and Classification . . . . .	39
2.2.4 Methods for the Tracking of Solar Flare Ribbons . . . . .	40
2.3 Summary . . . . .	45
<b>3 The Snake Algorithm</b>	<b>47</b>
3.1 Image Pre-processing . . . . .	47
3.1.1 Standard Pre-processing . . . . .	47
3.1.2 Non-Standard Pre-Processing . . . . .	49
3.2 Formulation of our Algorithm . . . . .	51

3.2.1	Basic Design . . . . .	51
3.2.2	Formulation of Model Energy Function . . . . .	54
3.2.3	Formulation of Data Energy Function . . . . .	55
3.2.4	Edge Detection . . . . .	56
3.2.5	Optimisation: Simulated Annealing . . . . .	57
3.2.6	Correct Truncation of the Snake . . . . .	58
3.3	Factors Affecting Snake Performance . . . . .	60
3.3.1	Changing the Weighting of Energy Sub-Functions . . . . .	60
3.3.2	Effect of Noise . . . . .	62
3.3.3	Laplacian of Gaussian . . . . .	63
3.3.4	Pressure . . . . .	64
3.4	Summary . . . . .	65
<b>4</b>	<b>The Snake Algorithm with Real Flare data</b>	<b>67</b>
4.1	Modifications . . . . .	67
4.1.1	Splitting into a Two-stage Process . . . . .	67
4.1.2	Truncating the Snake . . . . .	68
4.2	Finding the Error in the Snake Tracking Result . . . . .	69
4.3	Finding Ribbons in the Last Image of the Sequence . . . . .	71
4.3.1	Flare 20th January 2001, 20:46 - 21:16, M7.7, 1600 Å . . . . .	71
4.3.2	Flare 14 July 2000, 09:43 - 11:02, X5.7, 195 Å . . . . .	79
4.3.3	Flare 10th April 2001, 04:46 - 06:01, X2.3, 1600 Å . . . . .	82
4.3.4	Flare 25 June 2000, 07:36 - 08:40, M 1.9, 1600 Å . . . . .	84
4.3.5	Flare 12 November 1999, 08:39 - 09:49, 1600 Å . . . . .	86
4.3.6	Flare 8th February 2000, 08:33 - 09:37, M1.3, 1600 Å . . . . .	88
4.3.7	Summary of parameters used . . . . .	91
4.4	Tracking Flare Ribbons Through the Image Sequence . . . . .	92
4.4.1	Flare 20 January 2001, 20:46 - 21:16, M7.7, 1600 Å . . . . .	92
4.4.2	Flare 14 July 2000, 09:43 - 11:02, X5.7, 195 Å . . . . .	102
4.4.3	Flare 10th April 2001, 04:46 - 06:01, X2.3, 1600 Å . . . . .	111
4.4.4	Flare 25 June 2000, 07:36 - 08:40, M1.9, 1600 Å . . . . .	117
4.4.5	Flare 12 November 1999, 08:39 - 09:49, M1.7, 1600 Å . . . . .	124
4.4.6	Flare 8th February 2000, 08:33 - 09:37, M1.3, 1600 Å . . . . .	132
4.4.7	Image Characteristics that Affect the Parameters Used . . . . .	139
4.5	General Rules for Application . . . . .	140
4.6	Summary . . . . .	141
<b>5</b>	<b>Discussion and Conclusions</b>	<b>142</b>
5.1	Was the Aim Accomplished? . . . . .	142
5.2	Problems Encountered . . . . .	143

---

5.3	Different TRACE Passbands . . . . .	144
5.4	Future Work and Improvements . . . . .	145
5.5	Summary . . . . .	147
	<b>Bibliography</b>	<b>152</b>

# List of Figures

1.1	Schematic of a simple loop flare, useful for demonstrating the mechanism behind the various emission seen from flares, taken from Dennis & Schwartz (1989) . . . . .	17
1.2	Diagram showing the temporal evolution of emission in different wavelengths in the phases of a solar flare, from Benz (1993) . . . . .	18
1.3	The evolution of a flare as described by the CSHKP model. Note how as the flare progresses the site of reconnection rises and the footpoints spread. Taken from Hori et al. (1997) . . . . .	21
1.4	The TRACE telescope, (Handy et al. 1999) . . . . .	24
1.5	TRACE UV spectral response, (Handy et al. 1999) . . . . .	25
1.6	TRACE EUV thermal response, (Handy et al. 1999) . . . . .	25
2.1	Examples of spatial filters . . . . .	29
2.2	Illustration of a filter being applied to an image . . . . .	30
2.3	Demonstration of the difference between convolution and correlation .	31
2.4	An illustration of the principles of 1st order and 2nd order edge detection. The graphs show how $I$ , $\frac{\delta I}{\delta x}$ , and $\frac{\delta^2 I}{\delta x^2}$ vary with $x$ , along the cross section of the image shown. . . . .	33
2.5	TRACE images of solar flare ribbons in the 1600 Å passband, showing the original image (a), and the absolute value of the output image from a Laplacian of Gaussian edge filter with $\sigma = 3.5$ (b). . . . .	34
2.6	Image showing the image forces of (a) a conventional snake, and (b) a GVF snake. . . . .	38
2.7	An example showing an image degradation by cosmic ray hits (a), and the cleaned result (b), from (Marshall et al. 2006). . . . .	39
2.8	Flow chart summarising steps used in the automatic tracking of flare ribbons, from Qu et al. (2004b). . . . .	43
2.9	One of the original (i.e. unprocessed) images used by Qu et al. (2004b) in developing their algorithm, from Qu et al. (2004b). . . . .	43
2.10	Images showing the results of region growing (a), and region growing combined with boundary based methods (b), from Qu et al. (2004b). . . . .	43

2.11	Images showing the results of morphological closing (a), and small part removing and hole filling (b), from Qu et al. (2004b). . . . .	44
2.12	Images showing the results of component labeling (a), and showing the created flare “model” (b), from Qu et al. (2004b). . . . .	45
2.13	Graphical illustrations of the differences in ribbon separation and the calculate E-field between the automated algorithm developed by the author and a human observer, from Qu et al. (2004b). . . . .	46
3.1	Flow chart showing the basic design of our snake algorithm. . . . .	52
3.2	Figure showing snakes as they move over the simulated test image onto the simulated test ribbon. . . . .	54
3.3	Diagram showing snake with the simulated annealing temperature set too high, thus the snake moves past the feature. The snake in blue started at the bottom of the image, and the snake in red started at the top of the image. The image shown is a simulated test image. . .	58
3.4	Images showing an original image (a), together with reconstructed scale images output from the $\hat{a}$ trous algorithm from the smallest scale (b) through to the largest scale (d). . . . .	60
3.5	Diagram showing snake early in its progress, where the data energy function dominates over the model energy function. . . . .	61
3.6	Diagram showing snake early in its progress, where the model energy function dominates over the data energy function. . . . .	61
3.7	Diagram showing snake early in its progress, with the data and model energy functions weighted equally, the result is a snake which is attracted to the strong edges in the image but maintains a certain amount of rigidity. . . . .	62
3.8	Diagram showing snake in its final configuration, where it fits the test ribbon well. Image (a) shows a snake which is slightly more rigid than the snake in image (b), this rigidity prevents the snake from obtaining as close a fit as the snake in image (b). . . . .	63
3.9	Images showing snake results using different values for $\sigma$ in the LoG, and how this parameter can influence the end result of our algorithm. Images, shown using $\sigma = 1.0, 2.5, 5,$ and $6.5$ . . . . .	65
4.1	An image from a flare on 12 November 2000 in the TRACE 1600 Å band showing a clear difference in length between the two ribbons. . .	69
4.2	Images showing how the reconstructed scale image method for locating the end points of the ribbons fails. . . . .	70
4.3	Images showing the discontinuous and bifurcated nature of the the lower flare ribbon from 20 January 2001 in the TRACE 1600 Å band	75

4.4	First run of the snake algorithm on the last image in the time sequence from the 20th January 2000 flare. . . . .	76
4.5	Second run with last image from the flare on 20th January 2001. Both snakes still do not fit the ribbons well. . . . .	77
4.6	Third run with last image from 20 Jan 2001. Both snakes now fit their respective ribbons reasonably well. . . . .	78
4.7	Images showing snakes on last image from 14th July 2000, (a) overlaid on original image, and (b) overlaid on edge image. . . . .	80
4.8	Images showing snakes on last image from 14th July 2000, (a) overlaid on original image, and (b) overlaid on edge image. In these images the snakes do not cover the left most section of ribbon emission. . . .	81
4.9	Images showing snake result on last image from 10th April 2001, (a) overlaid on original image, and (b) overlaid on edge image. . . . .	83
4.10	Images showing snakes on last image from 25th June 2000, (a) overlaid on original image, and (b) overlaid on edge image. . . . .	85
4.11	Images showing snakes on last image from 12th November 1999, (a) overlaid on original image, and (b) overlaid on edge image. . . . .	87
4.12	The last image in the 8th of February 2000 flare. The outline of the upper ribbon has been manually traced. . . . .	89
4.13	Images showing snakes on last image from 8th February 2000, (a) overlaid on original image, and (b) overlaid on edge image produced with a value of $\sigma = 5.0$ . . . . .	90
4.14	Graph showing the error in the upper and lower snake in tracking the upper and lower ribbon for images from the 20th January 2001 flare image sequence, second sequence. . . . .	95
4.15	Graph showing the error in the upper and lower snake in tracking the upper and lower ribbon for images from the 20th January 2001 flare image sequence. . . . .	96
4.16	An image (a), and and edge image (b), showing the tracked ribbon positions for an image from the 20th January 2001 flare for the first application of the algorithm on the image sequence. . . . .	97
4.17	Images showing the tracked ribbon positions for images from the 20th January 2001 flare. Image (a) no. 005, (b) no. 010. . . . .	98
4.18	Images showing the tracked ribbon positions for images from the 20th January 2001 flare. Image (a) no. 020, (b) no. 030. . . . .	99
4.19	Images showing the tracked ribbon positions for images from the 20th January 2001 flare. Image (a) no. 040, (b) no. 050. . . . .	100

4.20	The first image of the 20th Jan 2001 flare sequence, with the tracked ribbon positions for images numbered 0, 10, 20, 30, 40 and 50 shown in red, cyan, blue, pink, green and yellow respectively. . . . .	101
4.21	Graph showing the error in the upper and lower snake in tracking the upper and lower ribbon, for both the “new” and “standard” methods, for images from the 14th July 2000 flare image sequence. . . . .	104
4.22	Images showing the tracked ribbon positions for images from the 14th July 2000 flare. Image (a) uses the “standard” method for edge image production, and image (b) uses the “new” method for edge image production. . . . .	105
4.23	Images showing the tracked ribbon positions for images from the 14th July 2000 flare. Image (a) no. 000, (b) no. 010. . . . .	106
4.24	Images showing the tracked ribbon positions for images from the 14th July 2000 flare. Image (a) no. 020, (b) no. 030. . . . .	107
4.25	Images showing the tracked ribbon positions for images from the 14th July 2000 flare. Image (a) no. 040, (b) no. 050. . . . .	108
4.26	Image showing the tracked ribbon positions for image no. 060, from the 14th July 2000 flare. . . . .	109
4.27	The first image of the 14th July 2000 flare sequence, with the tracked ribbon positions for images numbered 0, 10, 20, 30, 40, 50 and 60 shown in red, cyan, blue, pink, green, yellow and red respectively. . .	110
4.28	Graph showing the error in the upper and lower snake in tracking the upper and lower ribbon for images from the 10th April 2001 flare image sequence. . . . .	112
4.29	Images showing the tracked ribbon positions for images from the 10th April 2001 flare. Image (a) no. 000, (b) no. 001. . . . .	113
4.30	Images showing the tracked ribbon positions for images from the 10th April 2001 flare. Image (a) no. 002, (b) no. 003. . . . .	114
4.31	Image showing the tracked ribbon positions for image no. 004, from the 10th April 2001 flare. . . . .	115
4.32	The first image of the 10th April 2001 flare sequence, with the tracked ribbon positions for images numbered 0, 1, 2, 3, 4, 5 and 6 shown in red, cyan, blue, pink, green and yellow respectively . . . . .	116
4.33	Graph showing the error in the upper and lower snake in tracking the upper and lower ribbon for images from the 25th June 2000 flare image sequence. . . . .	118
4.34	Images showing the tracked ribbon positions for images from the 25th June 2000 flare. Image (a) no. 000, (b) no. 005. . . . .	119

4.35	Images showing the tracked ribbon positions for images from the 25th June 2000 flare. Image (a) no. 010, (b) no. 015. . . . .	120
4.36	Images showing the tracked ribbon positions for images from the 25th June 2000 flare. Image (a) no. 020, (b) no. 025. . . . .	121
4.37	Images showing the tracked ribbon positions for images from the 25th June 2000 flare. Image (a) no. 030, (b) no. 035. The inset in image (b) shows how the upper snake is held away from the ribbon by a point-like feature. . . . .	122
4.38	The first image of the 25th June 2000 flare sequence, with the tracked ribbon positions for images numbered 0, 5, 10, 15, 20, 25, 30 and 35 shown in red, cyan, blue, pink, green, yellow, red and cyan respectively. . . . .	123
4.39	Graph showing the error in the upper and lower snake in tracking the upper and lower ribbon for images from the 12th November 1999 flare image sequence. . . . .	125
4.40	Images showing the tracked ribbon positions for images from the 12th November 1999 flare. Image (a) no. 000, (b) no. 010. . . . .	126
4.41	Images showing the tracked ribbon positions for images from the 12th November 1999 flare. Image (a) no. 020, (b) no. 030. . . . .	127
4.42	Images showing the tracked ribbon positions for images from the 12th November 1999 flare. Image (a) no. 040, (b) no. 050. . . . .	128
4.43	Image no. 065 from the 12th November 1999 flare, showing the tracked ribbon positions. Part of the upper snake in the central part of the ribbon can be seen to be trapped above the main ribbon by a smaller secondary part of the ribbon forming a peaked shape. . . . .	129
4.44	Images showing the tracked ribbon positions for images from the 12th November 1999 flare. Image (a) no. 060, (b) no. 070. . . . .	130
4.45	The first image of the 12th November 1999 flare sequence, with the tracked ribbon positions for images numbered 0, 10, 20, 30, 40, 50, 60, 70 and 80 shown in cyan, blue, pink, green, yellow, red, cyan and blue respectively. . . . .	131
4.46	Graph showing the error in the upper and lower snake in tracking the upper and lower ribbon for images from the 8th February 2000 flare image sequence. . . . .	133
4.47	Images showing the tracked ribbon positions for images from the 8th February 2000 flare. Image (a) no. 000, (b) no. 005. . . . .	134
4.48	Images showing the tracked ribbon positions for images from the 8th February 2000 flare. Image (a) no. 010, (b) no. 015. . . . .	135

---

4.49	Images showing the tracked ribbon positions for images from the 8th February 2000 flare. Image (a) no. 020, (b) no. 025. . . . .	136
4.50	Images showing the tracked ribbon positions for images from the 8th February 2000 flare. Image (a) no. 030, (b) no. 035. . . . .	137
4.51	The first image of the 8th February 2000 flare sequence, with the tracked ribbon positions for images numbered 0, 1, 2, 3, 4, 5, 15 and 35 shown in red, cyan, blue, pink, green, yellow, red and cyan respectively. . . . .	138

# List of Tables

4.1	Table showing the parameters used for the snake algorithm for the last image in teh sequence for different flares. . . . .	91
4.2	Table showing the parameters used for the snake algorithm for the image sequences of different flares. . . . .	140

# Chapter 1

## Introduction

To the average observer the stars seem cold, distant and of little consequence to everyday life on Earth. There is of course one exception, the closest star to Earth, the Sun. Due to its relative proximity,  $1.496 \times 10^8$  km (compared to the next nearest star Proxima Centauri, which is about 270,000 times further away!), the Sun is of great importance to everyday life with the ability to exert a wide and diverse influence over the Earth, a fact not lost on many of our ancient ancestors.

Interest in the Sun has not waned over the years, with many active solar research groups in universities around the world. A major part of the appeal of solar physics research lies in the active nature of the Sun, including solar flares in particular. This thesis presents the development of an algorithm to aid in the study of solar flare physics. The algorithm aims to automatically track an observed feature of solar flares called flare ribbons, bright lines of emission that were first viewed in the  $H\alpha$  emission line. We aim to develop an algorithm that can accurately track these flare ribbons in a time series of UV or EUV images from the Transition Region and Coronal Explorer satellite (TRACE), and can be adapted for future missions, such as NASA's Solar Dynamics Observatory (SDO), due to launch in November 2009 (Anon. 2009a). The development of such a tool is necessary to enable the study of flare ribbon behaviour over large datasets, which is not practically possible using manual tracking methods. To develop such an algorithm we look to the field of image processing for a suitable solution. Initial stages of development will make use of a simplified test image to gain some familiarity with the application of our chosen solution. We then apply the algorithm to a small number of flare images from the TRACE satellite, after which we will review its suitability for the task and make any modifications or additions before applying the algorithm to a number of image sequences from different flares. We undertake a qualitative and quantitative review of its performance before our final discussion and conclusions.

This introductory chapter begins with an overview of the Sun and the motivation behind solar research. We then take a look at some of the basic properties of solar

flares, and the motivation behind the development of a ribbon tracking algorithm. The final part of this chapter gives a brief overview of the TRACE satellite, which is the source of images used in this project.

## 1.1 Solar Research Motivation

Current solar physics research has a number of motivations. As well as studying solar phenomenon in their own right, solar research helps in understanding the Sun's influence on our climate, predicting space weather, providing an understanding of stars, and providing an understanding of plasma in conditions not possible in the laboratory.

That the Sun can influence our climate has been long appreciated, but exactly how much influence it exerts is a topic of much current debate. One variable thought to influence our climate is the total solar irradiance. The total solar irradiance has steadily increased from the Sun's birth, but also fluctuates with the solar activity cycle (Stix 2004). During recent solar activity cycles the irradiance was seen to differ by approximately 0.1% with the Sun being brighter at solar maxima. Research in this area seeks to understand and quantify changes in the total solar irradiance and understand its effect on our planet, in particular our climate.

Space weather is used to describe the changing conditions of the ambient plasma, magnetic fields and radiation in the heliosphere. The solar wind is the major source of this ambient plasma. It is a stream of plasma ejected from the upper solar atmosphere into interplanetary space, and consists of two components; the slow solar wind and the fast solar wind. The slow solar wind moves at a velocity of about 400 km/s and the fast solar wind has a velocity of around 800 km/s (Feldman et al. 2005). Solar activity can affect the solar wind, which in turn can cause large fluctuations in space weather conditions. This can result in geomagnetic storms in the Earth's atmosphere, which can have a number of different disruptive effects, including damaging national power grids. Less violent changes in space weather can cause the Earth's atmosphere to contract or expand which in turn seriously affects the orbits of satellites close to the Earth. Energetic particles accelerated by flares and coronal mass ejections (CMEs) can physically damage satellites and cause serious harm to astronauts. The study of the causative solar eruptive events is of obvious importance in the role of space weather predictions, abilities to predict these events and understand their effect on the solar wind and space weather in general will enable quicker and more accurate prediction of disruptive space weather. Solar flares contribute to space weather directly, and can also be associated with coronal mass ejections which are the main driver of Geomagnetic disturbances and greatly influence space weather in general.

As the closest star to Earth by some considerable distance the Sun provides a unique opportunity for understanding stellar structure and evolution. Close study of the Sun has allowed us to determine properties of its interior, surface and upper atmosphere that are considerably more difficult to discover in other stars.

Finally as a plasma laboratory the Sun has no comparison in our solar system; it enables the study of plasma in conditions that are not easily reproduceable on Earth. Plasma fusion on Earth has been a goal of many plasma physicists for decades, the knowledge gained by studying the Sun is invaluable to this aim as well as for the study of plasma in general. Solar plasma studies can also aid in the understanding of other astronomical plasmas.

## 1.2 Solar Structure

The Sun is a main sequence star of spectral class G2V and is considered average in terms of size and energy output. It is around 4.5 billion years old, at an average distance of  $1.496 \times 10^8$  km away from the earth, with a radius of  $6.95 \times 10^5$  km, a mass of  $1.989 \times 10^{30}$  kg and a luminosity of  $3.844 \times 10^{26}$  W (Stix 2004).

The Sun's mass is comprised of approximately 70% hydrogen and 28% helium, with the remaining 2% consisting of heavier elements. The Sun's energy is produced in its core through the nuclear fusion of hydrogen into helium via the proton-proton chain. Hence the amount of hydrogen relative to helium changes with time. The core of the Sun extends to approximately  $0.2 R_{\odot}$ , and is a very hot dense plasma with a temperature in excess of 13 MK and a number density of around  $10^{32} \text{ m}^{-3}$ . Energy from the core is radiatively transported out to around  $0.7 R_{\odot}$ , where the temperature gradient becomes sufficiently steep for convection to become the dominant energy transportation mechanism. It is thought that the solar magnetic field is generated just below the convection zone as a result of fluid shear between the plasma of the convective zone and the plasma of the radiative zone. The motion of plasma in the convective zone is thought to twist and concentrate the magnetic field lines into "flux ropes", which rise to the solar surface where they are responsible for solar activity.

The visible surface of the Sun is the photosphere, as it presents a transition between the optically opaque interior and the transparent solar atmosphere. This layer of the Sun is only a few hundreds of km thick, has a number density of around  $10^{23} \text{ m}^{-3}$ , and its emission is very close to that of a blackbody at a temperature of around 5800 K. Observation of the photosphere reveals the presence of sunspots, and at a smaller scale, granulation. Sunspots appear darker than their surroundings as they are cooler than the surrounding plasma. This is thought to be due to the suppression of convection by the strong magnetic fields present in the sunspot.

The study of sunspots is perhaps one of the oldest solar physics disciplines, with early observers including Galileo Galilei. The lifetime of a sunspot is typically a few weeks, enabling their use as tracers for differential solar rotation. Sunspots appear in groups, which are usually restricted to latitudes  $\pm 40^\circ$ , with their number and positions evolving with the 11 year solar activity cycle caused by the reversal of the solar magnetic field. Sunspots locate the base of active regions that extend from the photosphere high into the solar atmosphere. Granulation describes the seething small scale pattern of small granules that covers the photosphere. Individual granules are the tops of convection cells rising from the solar interior. They are roughly 1000 km across and have a typical lifetime of around ten minutes. The granules appear bright at the centre where hot material from below emerges at the photosphere, and appear darker at the edges where the cooler plasma flows back into the solar interior. Supergranulation is an observed pattern superimposed onto the smaller scale granulation, which was first discovered using Doppler velocity measurement of horizontal flows on the photosphere (Leighton et al. 1962). Supergranulation has been attributed to a larger scale convection, with the typical size of a supergranule of 30000 km and a typical lifetime of around 15–30 hours (Stix 2004; Zirin 1988).

Overlying the photosphere is the chromosphere, where the temperature initially drops with increasing altitude to around 4000 K before increasing to reach around 20,000 K at its outer limit. Emission from the chromosphere is predominantly from spectral emission lines in optical and UV wavelengths, in particular from the  $H\alpha$  line of the Balmer series, which gives the chromosphere its red appearance responsible for its name (chroma meaning colour). The majority of chromospheric features have been discovered through observation in either  $H\alpha$  or Ca II. Such features include: spicules, chromospheric network, prominences and filaments. Filaments and prominences refer to cool dense clouds of chromospheric plasma that are suspended higher in the solar atmosphere by strong magnetic flux tubes. The different names refer to the same feature when viewed on the solar limb (prominences) or on the solar disk (filaments). Spicules represent smaller scale and more transient structures of chromospheric plasma that extend into the higher solar atmosphere as long thin jets. The chromospheric network is a web-like pattern of enhanced clumpy emission which is thought to be the result of concentrated magnetic field at supergranular boundaries in the underlying photosphere (Simon & Leighton 1964).

The boundary between the outer layer of the solar atmosphere, the corona, and the chromosphere is a few hundreds of km thick and is named the transition region. The transition region does not have a defined altitude but instead exists as an encompassing layer around the chromosphere and chromospheric plasma including spicules and filaments, and therefore moves with these features. Across this layer the density drops and the temperature rises sharply from approximately  $10^4$  K at

lower altitudes, to around  $10^6$  K at the higher altitudes where it meets the corona. As a result of the wide temperature range there are a large number of ionisation species giving rise to emission in the UV spectrum from around 50 nm to 160 nm.

The corona is the outer layer of the solar atmosphere and extends out to several solar radii. It is extremely hot and tenuous, with temperatures reaching 3 MK and densities low in the corona of around  $10^{15}$  m<sup>-3</sup>. The question of how the corona is heated to such high temperatures has long troubled solar physicists, and remains open to debate. The corona is visible in white light, which is Thomson scattered photospheric radiation (i.e. scattered by free electrons), whilst there is also emission in other wavelengths such as EUV and X-rays. The appearance of the corona varies with the solar activity cycle, and at solar minimum the corona is confined to lower latitudes with coronal holes present at the poles. Coronal holes appear in images as dark areas devoid of coronal emission. They are associated with regions of open magnetic field where coronal plasma streams out into interplanetary space to form the solar wind. At solar maximum coronal holes are no longer restricted to polar latitudes and the structure of the corona is generally more complex and dynamic (Stix 2004). The generated magnetic field in the solar interior rises due to magnetic buoyancy through the solar interior and photosphere up into the corona (Zirin 1988). Active regions are areas where this magnetic field appears strong and complex, and extend from the photosphere where sunspots occur, through to the corona. Coronal loops are large scale structures of plasma held aloft in magnetic flux tubes. They appear in active regions, where they are categorised as active region loops and also in the quiet Sun (i.e. anywhere that is not an active region), where they are categorised as quiescent loops. Another type of loop is the post flare loop, which will be discussed in the following section. Active regions are, as the name would suggest, the seat for solar activity in the corona, including coronal mass ejections and solar flares.

### 1.3 Solar Flares

Solar flares are characterised as an intense rapid release of energy from the reconfiguration of stressed coronal magnetic fields. Energy is released in the form of electromagnetic radiation, energetic particles, and bulk plasma motion. The first recorded observation of a flare was made independently by R. C. Carrington and R. Hodgson in 1859, who both reported observed areas of intense brightening in a sunspot group they were studying at the time. The witnessed event was a white light flare, an event that is sufficiently bright to be visible against the photosphere in optical wavelengths, and is a reasonably rare occurrence. Until relatively recently flare observations were carried out in a small number of spectral lines, most com-

monly  $H\alpha$ . The advent of space based flare observations has increased the range of wavelengths used for the study of flares. Flares are currently observed across the electromagnetic spectrum, including  $\gamma$  rays, X-rays, white light,  $H\alpha$ , UV, EUV and radio waves, from space based and/or ground based observatories.

The largest flares can release the order of  $10^{26}$  J. The source of these prodigious amounts of energy is commonly accepted to be the reconfiguration of stressed magnetic fields through the process of magnetic reconnection. Several theoretical models of reconnection have been proposed by Parker (1963), Petschek (1964) and Sturrock et al. (1984) and are still of much interest and debate. The actual process of magnetic reconnection, i.e. the way in which the stored magnetic energy is so quickly released (over time-scales of minutes to tens of minutes) as the field reconfigures, remains one of the fundamental questions of solar flare physics. Equally challenging is the related question of how so much of that released energy is converted into the kinetic energy of charged particles.

Flares typically occur in active regions close to sunspots, where the magnetic fields are often concentrated, twisted and sheared. More complex sunspot groups generally indicate a greater complexity in the local magnetic field and therefore a greater frequency of flares (Tandberg-Hanssen & Emslie 1988). The frequency of flare occurrence varies with the solar activity cycle; at solar maximum several flares per day are commonly observed, while at solar minimum weeks can pass without a single flare observation. The larger flares are a less frequent occurrence than smaller flares.

Flares can be grouped according to their morphology, giving us compact (or single loop) flares and two-ribbon flares. A compact flare is thought to occur in a small loop in the lower corona, and is confined to the plasma contained in the loop (Tandberg-Hanssen & Emslie 1988). Two-ribbon flares occur immediately after the disappearance of a filament (Stix 2004), these flares exhibit arcades of “post-flare loops” as seen in EUV and soft X-rays, that are the result of heated plasma contained by post-reconnection magnetic field loops. At the bottom of these loops, where they intersect the chromosphere and transition region, bright point-like sources of emission appear, termed footpoints. The footpoints of adjacent loops form elongated clumpy areas of emission along the length of the flare known as flare ribbons. These ribbons have long been observed in the chromospheric emission of  $H\alpha$  (Michalitsanos & Kupferman 1974; Svestka 1976; Henoux & Rust 1980; Kurokawa 1989; Qu et al. 2004b), and more recently in high resolution in UV and EUV by TRACE (Fletcher & Hudson 2001; Warren 2001; Fletcher et al. 2004; Su et al. 2006; Saba et al. 2006). The ribbons lie to either side of a recently disappeared filament and of the magnetic neutral line, and are observed to move away from each other as the flare progresses. After the flare a new filament is often seen to form at the same location, whose

sudden disappearance results in another flare, referred to as a homologous flare (Tandberg-Hanssen & Emslie 1988). It is observed that the horizontal component of the magnetic field appears to be rearranged by the occurrence of the flare (Stix 2004). Pre-flare it is nearly parallel with the filament, and post-flare it appears almost perpendicular to the direction of the disappeared filament.

**Figure has been removed due to copyright reasons.**

Figure 1.1: Schematic of a simple loop flare, useful for demonstrating the mechanism behind the various emission seen from flares, taken from Dennis & Schwartz (1989)

The general picture of flare emission and the processes responsible for the emission is neatly summarised in Figure 1.1. The important mechanisms for this thesis are those giving rise to UV continuum emission from the footpoints that form flare ribbons, this is discussed in more detail in Section 1.3.2. The temporal evolution of the emission from a flare can be separated into a number of distinct phases, which in order are; pre-flare phase, impulsive phase, flash phase and decay phase, although “flash phase” is less frequently used now.

Figure has been removed due to copyright reasons.

Figure 1.2: Diagram showing the temporal evolution of emission in different wavelengths in the phases of a solar flare, from Benz (1993)

The pre-flare or rise phase is seen in most, but not all flares, and begins with the start of magnetic energy release in the corona, which causes the gradual heating of plasma resulting in emission of EUV, soft X-rays and radiowaves. The impulsive flare phase follows, which typically lasts for a few minutes and consists of multiple short bursts of emission 1-10 s in duration seen in  $\gamma$ -rays, hard X-rays, EUV and microwaves. It is during this phase that the majority of the energy is released through the acceleration of a large number of particles, which are the source of the wide range of emission observed. After the impulsive phase comes the flash phase where heat is further dissipated through the coronal plasma. This phase sees a fall off in soft X-ray emission but still sees an increase in UV,  $H\alpha$  and certain wavelengths of radio. The final phase of the flare, the decay phase, sees a steady reduction of emission in nearly all wavelengths, as seen in Figure 1.2, associated with the plasma returning to its pre-flare state.

### 1.3.1 GOES Classification of Solar Flares

The currently accepted method for flare classification is based on the peak soft X-ray flux (in the range 1-8 Å) of a flare as observed by the GOES satellites. When a certain flare is being referred to it is common practice to detail the date and time of the flare as well as its GOES classification. This system uses classifications of A, B, C, M and X, with each class further subdivided into 10 sub-classes. Flares in class A have an observed peak flux above  $10^{-8}\text{Wm}^{-2}$ , with each subsequent class having a lower limit greater than the previous class by one order of magnitude, so that X class flares must have an observed peak flux greater than  $10^{-4}\text{Wm}^{-2}$ . The subclasses represent an increase in the observed flux by an integer multiple of the lower limit of the parent class, so that a flare classified a A6 will have an observed

peak flux of  $6 \times 10^{-8} \text{Wm}^{-2}$ . The largest ever recorded flare occurred on the 4th November, 2003. The original GOES classification for this flare was X28, however this represented the flux at which the GOES detectors were saturated rather than the actual flux of the flare. After studying the effect of this flare on the earth's atmosphere, it has been suggested that a more accurate classification would place the flare between X40 and X45 (Brodrick et al. 2005).

### 1.3.2 UV and EUV Ribbons in Two-Ribbon Flares

That magnetic energy released high in the corona is transported down into the chromosphere and transition region is a point of consensus amongst different flare models, even if the exact nature of the energy transportation is not. Competing models cite accelerated beams of particles (Brown 1973; Brown et al. 1990), thermal conduction from the hot loop plasma (Smith & Lilliequist 1979; Brown et al. 1979), or Alfvén waves (Fletcher & Hudson 2008) as the means for energy transportation. As a result of this sudden energy deposition the chromospheric plasma is heated, and emits over many wavelengths, including  $\text{H}\alpha$ , UV, and EUV.

Particle beam models proposed include electron and proton beams. Electron beam models envisage a stream of fast electrons accelerated away from the reconnection site in the corona, where they are guided down into the lower solar atmosphere by the newly reconnected field lines via the Lorentz force. As these electrons pass through the low density corona they undergo very few collisions, and so the beam retains the bulk of its energy. As the beam comes into contact with the denser plasma of the transition region and the chromosphere the electrons experience a high number of Coulomb collisions, such that the electron beam is stopped and heats the surrounding plasma. The heated plasma then evaporates, or more correctly ablates, into flux tubes along the newly reconnected field lines, thus forming post-flare loops. Footpoint and ribbon emission is seen also in the form of hard X-ray bremsstrahlung radiation as the result of Coulomb collisions between the precipitating fast electrons and the dense plasma of the chromosphere and transition region. Proton beam models replace fast electrons with fast protons, and require fewer accelerated particles than electron beam models for the equivalent hard X-ray emission (Emslie & Brown 1985). High energy proton beam models account for hard X-ray emission as proton-electron bremsstrahlung, whilst low energy proton beam models require some indirect cause for the observed hard X-ray emission (Brown et al. 1990). Brown et al. (1990) suggest that high energy proton beam models are not consistent with a number of observations. The favoured model sees electron beams as the cause for the hard X-ray emission, with the possibility of low energy proton beams adding to the plasma heating process (Aschwanden 2004).

Conduction driven heating models are based on the heating of plasma local to the site of reconnection in the corona. The heated plasma expands and forms a thermal conduction front with a steep temperature gradient across its leading edge. The thermal conduction front propagates along the newly reconnected magnetic flux tube into the transition region and chromosphere, heating the local plasma (Smith & Lilliequist 1979; Aschwanden 2004).

Sakao (1994) presents the simultaneity of hard X-ray footpoints in HXT observations of 6 flares from the Yohkoh satellite as evidence for electron beam driven heating. This inference is based on the premise that conduction front driven heating or proton beam driven heating could only produce simultaneous footpoints if the reconnection event is located exactly at the midpoint of the flare loops due to the slower propagation speeds of the energy transport in these models. Other evidence for electron beam driven heating includes the observed time delay between electrons responsible for higher energy hard X-rays and electrons responsible for lower energy hard X-rays. This time delay is predicted for the typical electron beam model described above, and has been observed in a large number of different flares reported in a number of papers (Aschwanden et al. 1995; Aschwanden & Schwartz 1995; Aschwanden et al. 1996a,b). A high degree of spatial and temporal correlation between observations of hard X-ray footpoint emission indicative of the impact of a particle beam with a “thick target”, and UV and EUV footpoint emission indicative of heated plasma, can also be interpreted as observational evidence for electron beam driven heating. Conduction driven heating is suggested where the UV and EUV emission is observed with no corresponding hard X-ray emission, as observed by Czakowska et al. (2001), in the stages of the flare after the impulsive phase.

The suggestion of Alfvén waves as the accelerator of high energy electrons in solar flares is still new (Fletcher & Hudson 2008). The appeal of this model is that it fits with recent observations of rapid changes in the line-of-sight component of photospheric magnetic fields and provides an explanation for the large numbers of electrons implied by flare hard X-ray emission, which is one of the major criticisms of the previously discussed electron beam models.

All of these models of energy transport from the reconnection region to transition region and chromosphere have the energy being transported along the newly reconnected magnetic loops, and heating the plasma local to the two footpoints. The result of the heating of the plasma at the footpoints is emission in  $H\alpha$ , UV and EUV. Adjacent footpoints from adjacent loops are observed to form elongated ribbons, which have long been studied in  $H\alpha$ , and more recently studied in UV (Fletcher et al. 2004), and EUV (Fletcher & Hudson 2001). New magnetic field lines that reconnect at ever higher altitudes result in loop footpoints that are ever further apart, as seen in Figure 1.3 which shows a 2D schematic of flare evolution

**Figure has been removed due to copyright reasons.**

Figure 1.3: The evolution of a flare as described by the CSHKP model. Note how as the flare progresses the site of reconnection rises and the footpoints spread. Taken from [Hori et al. \(1997\)](#)

according to the “CSHKP” magnetic reconnection model. The CSHKP model is named after the contributions from [Carmichael \(1964\)](#); [Sturrock \(1966\)](#); [Hirayama \(1974\)](#); [Kopp & Pneuman \(1976\)](#). As the energy released in the flare is channelled along the newly reconnected magnetic loops to the loop footpoints, new regions of heated plasma are observed through their emission, with the emission from the previous regions of heated plasma fading as the plasma cools. This effect results in the observed drifting separation of the flare ribbons, showing a migration of the site of plasma heating rather than the bulk movement of any plasma.

Many flare footpoint studies overlay tracked ribbon positions onto magnetograms or white light images, enabling the observation of the ribbon positions relative to magnetic field and features such as sunspots throughout the flare. This combination of flare ribbon positions and magnetic field information provide an important insight into magnetic field configuration and evolution during flares useful for the validation or challenging of theoretical flare and reconnection models. With the assumption that the flare ribbons locate the footpoints of newly reconnected fields lines, as discussed above, it is possible to infer the amount of magnetic flux involved in reconnection as the flux present in the area of the magnetogram which has been mapped out between subsequent ribbon positions. With the time difference between images it is possible to calculate reconnection rates for the flare as a whole and for the intervals between images. This method is employed by [Fletcher & Hudson \(2001\)](#), [Fletcher et al. \(2004\)](#) and [Saba et al. \(2006\)](#) with UV ribbons, and by [Qiu et al. \(2002\)](#), [Wang et al. \(2003\)](#), [Qu et al. \(2004b\)](#), and [Asai et al. \(2006\)](#) using  $H\alpha$  flare ribbons. These calculated magnetic reconnection rates can be used to constrain theoretical reconnection models, as suggested in [Wang et al. \(2003\)](#). [Fletcher & Hudson \(2001\)](#) observe that the EUV ribbons from the “Bastille day 2000” flare imply different amounts of reconnecting magnetic flux responsible for the production of the two ribbons, an observation that does not fit well with flare models such as the CSHKP model, but could also be explained by instrumental calibration. They also observe one of the ribbons evolving from a less regular contorted morphology into a more regular, straighter morphology as the flare progresses, suggesting field

lines closer to the reconnection site are more sheared and tangled than those further away. Saba et al. (2006) observe a GOES M1 class flare on 23 November, 2000, where the ribbons show no separation, but instead grow in width and lengthen in an antiparallel and roughly circular motion, which the authors attribute to photospheric flows shearing magnetic field lines.

All of the papers discussed here present findings from one observed event each. Carrying out similar research on a large datasets is clearly desirable but doing so using manual methods for tracking the ribbon positions presents a significant and unappealing challenge. The use of automated techniques, as in Qu et al. (2004b), to track flare ribbons will enable a significant reduction in the user intervention and the cost necessary for the use of these larger datasets. The focus of this project is to produce an algorithm capable of automated tracking of flare ribbons in TRACE UV and EUV data, and like Qu et al. (2004b), we look to image processing to provide a suitable technique.

## 1.4 The TRACE Mission

The TRACE satellite belongs to the NASA Small Explorer (SMEX) program, managed by a SMEX department at the Goddard Space Flight Centre. The SMEX program aims to launch relatively simple, focused, and cost effective space science missions, weighing up to 250 kg with total costs (up to day 30 of the mission) of \$35 million. The focused aim for TRACE was to surpass the previous best in time and spatial resolution for UV and EUV imaging of the transition region and the corona. TRACE was successfully launched from Vandenberg Air Force Base on 2nd April 1998 Universal Time, with the first telemetry being received an hour and a half after launch. Since then TRACE has continued to be a success providing the solar research community with over 17 million images as of October 2003 (Schrijver & Tarbell 2004). TRACE images have also been a success with members of the public, with its images among the most popular space images after those taken with the Hubble Space Telescope.

The success of TRACE is due in no small part to the experience gained in previous successful missions such as SOHO, NIXT and SXT. Hardware, designs and personnel from these missions have been paramount to the successful design, construction and operation of TRACE on the limited SMEX budget. SOHO provided some spare flight hardware, the designs of the MDI instrument were used as the basis for the TRACE telescope, designs and project teams were, and in the case of the project team, are being used from the NIXT and SXT missions (Handy et al. 1999).

The TRACE satellite has a Sun-synchronous polar Earth orbit, which closely fol-

lows Earth's day-night terminator. This affords it an uninterrupted viewing season of around 9 months, followed by a 3 month eclipse period (Schrijver et al. 1999). This uninterrupted viewing season combined with internally stabilised telescope pointing enables TRACE to follow many features of interest throughout their evolution.

The science goal for TRACE is to observe the detailed magnetic field present in the transition region and corona through imaging the plasma present in these volumes of the solar atmosphere. By choosing wavebands centred on particular emission lines corresponding to particular ionisation states of carbon and iron it is possible to observe plasma at different temperatures. TRACE is able to switch between the different wavebands very quickly, take images with small exposure times and has small lag times between exposures, thus enabling the study of different temperatures of plasma with near simultaneity. With a pixel size of 0.5 arc sec TRACE has a spatial resolution of 1 arc sec, relating to a distance of 725 km on the Sun and providing the highest resolution of current UV images of the Sun. This unique view of plasma structures enables observers to track the emergence of plasma structures as they evolve from low in the transition region to high in the corona.

The principal reason for choosing TRACE data for this study is the high time and spatial resolution of these data. In order to gain the most accurate description of a flare ribbon's temporal evolution it stands to reason that one would want to use data of sufficient spatial resolution to accurately represent its position and structure and of sufficient temporal resolution to view changes in its evolution. Golub et al. (1999) observe that structure is seen down to the resolution limit of TRACE, as such using other data would not allow us to observe the finer structure of a flare ribbon.

### 1.4.1 TRACE Instrumentation

The design of the TRACE telescope uses the design of the MDI telescope on-board SOHO (Solar and Heliospheric Imager) as its blueprint, which is a 30cm aperture Cassegrain design as presented in Figure 1.4. The telescope field-of-view is 8.5 arc min square which approximately relates to one tenth of the solar disk. Telescope pointing is designed to be internally stabilised to within 0.1 arc sec to counter spacecraft jitter, however pointing errors of up to 10 arc sec have been observed when the solar limb is not in view, as discussed in Fletcher & Hudson (2001).

The telescope is split into four quadrants along its optical axis, with each quadrant of mirror having a specific multi-layer coating designed to selectively reflect desired wavelengths. Three of the quadrants are thus optimised for EUV, and each of these for an individual passband, these being 171, 195 and 285 Å respectively. The remaining quadrant is optimised for UV, and used for the passbands in the

**Figure has been removed due to copyright reasons.**

Figure 1.4: The TRACE telescope, (Handy et al. 1999)

1200-7000 Å range of wavelengths. At the entrance of the telescope a filter is used to prevent light of unwanted wavelengths from entering the telescope optics. The UV quadrants of this filter are thin-film aluminium filters, with the UV quadrant consisting of a 10mm thick UV broadband filter. Sitting behind the entrance filter is the quadrant selector, which blocks the passage of UV or EUV for three of the quadrants and so choosing the fourth quadrant as the passband for observation. When the UV quadrant is selected there are other mechanisms for selecting the particular UV band for imaging.

The TRACE CCD is 1024 by 1024 pixels in size, with each pixel corresponding to 0.5 arc sec, and is sensitive to wavelengths  $\lambda \geq 4000$  Å. To enable the CCD to image in UV and EUV it has a thin 1500 Å coating of lumogen. Incident UV and EUV photons excite this coating causing it to fluoresce in visible light. This visible light is then recorded by the CCD. Pre-mission testing determined that the lumogen would appreciably degrade during use due to the constant bombardment by EUV photons, but in practise the degradation has been far less than predicted, extending the useful lifetime of TRACE. Anything but uniform degradation of the lumogen will need to be accounted for in the flat field correction (discussed chapter 4). Each pixel in the TRACE CCD corresponds to approximately  $1.31 \times 10^5$  km<sup>2</sup> on the solar surface, and thus the entire CCD can image  $1.37 \times 10^{11}$  km<sup>2</sup>. Exposure times are controlled by a mechanical shutter blade with two openings: a small opening enables exposures in multiples of 1.6 ms by making a number of passes in front of the CCD, whereas the larger opening exposes the entire CCD at once and provides exposure times from 20 ms up to 260 s. TRACE telemetry typically contains around 700 Mbyte worth of images per day, with images being compressed by a variable amount using a JPEG algorithm.

### 1.4.2 TRACE Spectral Response

Plasma imaged by TRACE ranges from  $6 \times 10^3 - 1 \times 10^7$  MK, and can be situated anywhere from the photosphere through to high in the corona, making possible the study of solar phenomena from their emergence from the solar interior through their evolution and possible migration into the upper solar atmosphere. The TRACE passbands used in this project are 195 Å and 1600 Å, with each passband it is

possible to image chromospheric flare ribbons.

The 1600 Å channel includes a range of wavelengths from approximately 1450 Å up to 2000 Å, with the peak transmission of the combined optics and filters at approximately 1625 Å. The transmission over this range of wavelengths can be seen in Fig. 1.5.

**Figure has been removed due to copyright reasons.**

Figure 1.5: TRACE UV spectral response, (Handy et al. 1999)

The wavelengths included in the EUV channels are dependent on the use of the two additional thin film aluminium filters sitting just in front of the CCD, with the range being reduced with the use of one filter, and reduced further with the use of both filters. Without these additional aluminium filters in use the range of wavelengths that contribute to the 171 Å channel start at approximately 165.5 Å, with the peak contribution at approximately 174 Å, up to about 187 Å. The reason this channel is referred to as the 171 channel is to maintain consistency with the terminology of SOHO.

Figure 1.6 shows the temperature response of the three EUV passbands, the peak responses of which lie at approximately 1 MK, 1.5 MK a 2 MK for the 171 Å, 195 Å and 284 Å channels respectively (Schrijver et al. 1999). It should also be noted that there are considerable contributions to each channels response from other sub-peaks at different temperatures due to emission from particular ionisations for example from Fe XXIV.

**Figure has been removed due to copyright reasons.**

Figure 1.6: TRACE EUV thermal response, (Handy et al. 1999)

## 1.5 Summary

This chapter has introduced the aim of the project and outlined the motivations behind it. We have discussed some important background information relevant to the project motivation and the understanding of solar flares. As the source of

---

our solar flare images the TRACE satellite and its instrumentation is summarised, introducing the wavebands and associated temperatures of plasma in which we see UV and EUV flare ribbons. In the following chapter we continue to provide relevant introductory and background material, with the focus shifted to the subject of image processing and its application in solar physics, and in particular image processing techniques applicable to the automated detection and tracking of image features.

# Chapter 2

## Image Processing in Solar Physics

This chapter gives an introduction to the image processing background and techniques relevant to this project. This includes an overview of image pre-processing and image segmentation, with a section focussed on active contours. It follows with a brief overview of the application of image processing techniques to solar physics and a more concentrated discussion on flare ribbon tracking.

### 2.1 Image Processing Background

Image processing is conducted for two reasons: (1) To aid human interpretation of an image, (2) to store, transmit or represent image data for autonomous computer based interpretation (Gonzalez & Woods 2007). An image can be defined as a two dimensional function  $I(x, y)$ , where the value at any point in the two dimensional plane space indexed by coordinates  $x$  and  $y$  is referred to as a grey level value or intensity. In the case of digital images, the intensity  $I$  and the  $x$  and  $y$  coordinates are finite discrete values. At each coordinate there is an associated image element more commonly referred to as a pixel. Image processing (or more specifically digital image processing) is a series of actions applied to the input image function to produce an output. The output can be a modified version of the original image, but is not exclusively so. This fairly broad definition encompasses image analysis and computer vision, which are commonly accepted as disciplines in their own right. To draw some distinctions between these disciplines it is helpful to consider a broad spectrum of such techniques, ranging from the most simplistic low level to the most advanced high level techniques. In this scheme a low level process is one in which the output is a modified version of the input image, such as a smoothing filter. These processes are often used to enhance an image for further analysis either by a human observer or other computer based algorithms. Mid-level processes aim to extract certain features through segmentation of the image, here the outputs are normally something other than a modified image, for example information about objects identified in the

image. Higher level processes involve interpretations arrived at by combining the information gathered from the image with a relevant knowledge base. An example of a high-level process would be a motorway lane guidance system in a car. Techniques at this most advanced end of the spectrum fall into the discipline of 3D computer vision, at the opposite simplest end are 2D image processing techniques, and lying between the two is image analysis. The boundaries between these disciplines are blurred. The development of our algorithm lies near the boundary between image processing and image analysis.

One of the earliest applications of digital image processing was the coding and decoding of newspaper pictures sent across the Atlantic through submarine telegraph cables. The Bartlane cable picture transmission system was one of the early advances in this process and greatly reduced transmission times (Gonzalez & Woods 2007). Such systems however do not really fit into the current idea of digital image processing as they do not make use of computers. The advent of digital image processing, as we know it today, relied on the combination of available digital images, available computer hardware and suitable motivation. One of the first instances where these factors were brought together was with the American Ranger 7 moon probe in 1964, which transmitted digital images of the moon back to Earth (Gonzalez & Woods 2007). Distortions in the images were corrected using a computer program at NASA's Jet Propulsion Laboratory (JPL). JPL was soon to become a hub for pioneering image processing with many later missions to the moon providing more digital imagery in need of restoration and enhancement. Medical imaging was also an area of early image processing development, in particular with the development of the CAT (Computer Axial Tomography) scan. Early applications of image processing were also found in astronomy and in remote sensing satellite imagery of the Earth. With the growth of digital imaging devices and computers has come the growth and development of image processing, and its modern day methods and applications are diverse and numerous.

### 2.1.1 The Application of Image Processing Filters

Simple low level image processing filters are often used to modify images to make them more suitable for their intended use. This is referred to as "pre-processing". Such filters can be employed to reduce noise, smooth or sharpen an image, increase or decrease the brightness, or enhance a particular type of feature. The application of such filters may occur in the spatial domain. The central position of the filter is passed over each image pixel in turn, with the result at each pixel location forming the output into a new image. The result is determined by a pre-defined function that uses the values of the input image pixels contained within the filter. Examples

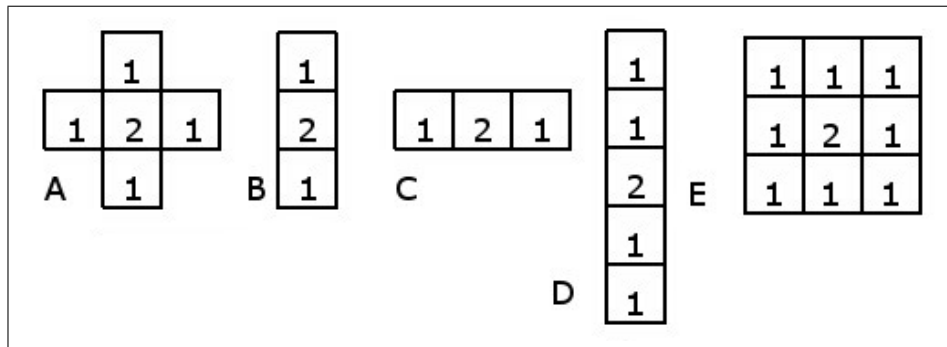


Figure 2.1: Examples of spatial filters

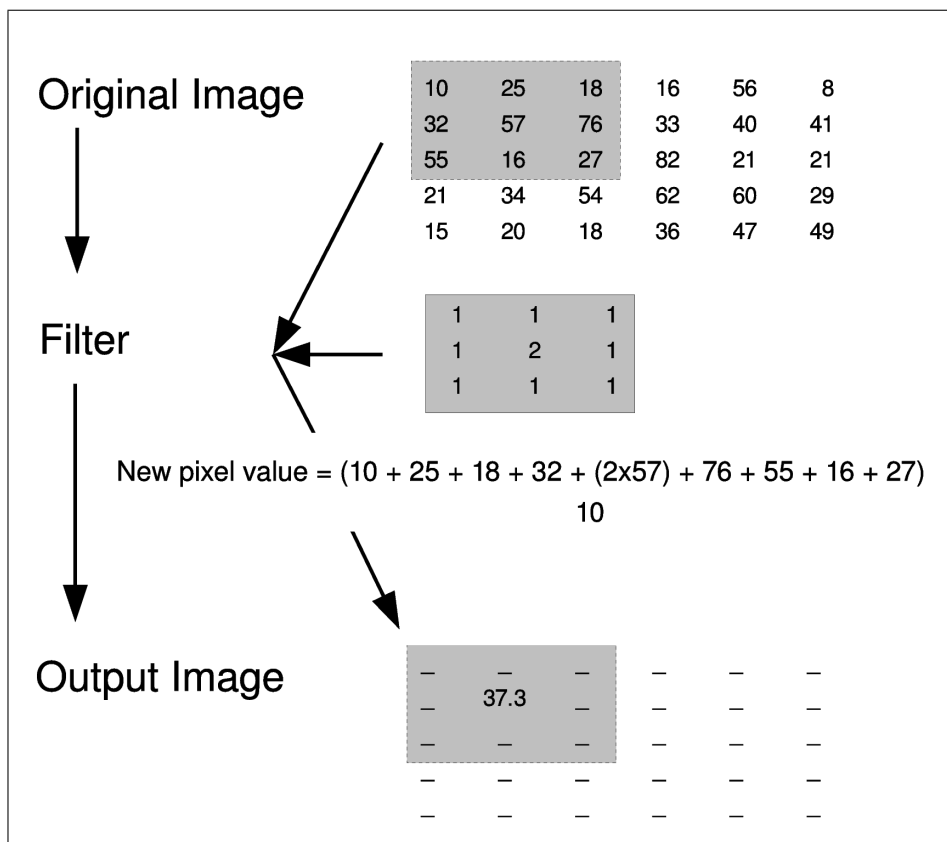


Figure 2.2: Illustration of a filter being applied to an image

of such filters are shown in Figure 2.1. The values shown within the filters refer to a weight applied to the image pixel value associated with each filter position. For example, consider a filter three pixels in width, one in depth, with the values arranged  $[1,2,1]$  as in filter C from Figure 2.1. Where this filter passes over three image pixels the new middle pixel is defined to be the sum of the left and right pixel, plus twice the middle pixel, all divided by 4. This process is demonstrated with a larger 3 by 3 filter in Figure 2.2

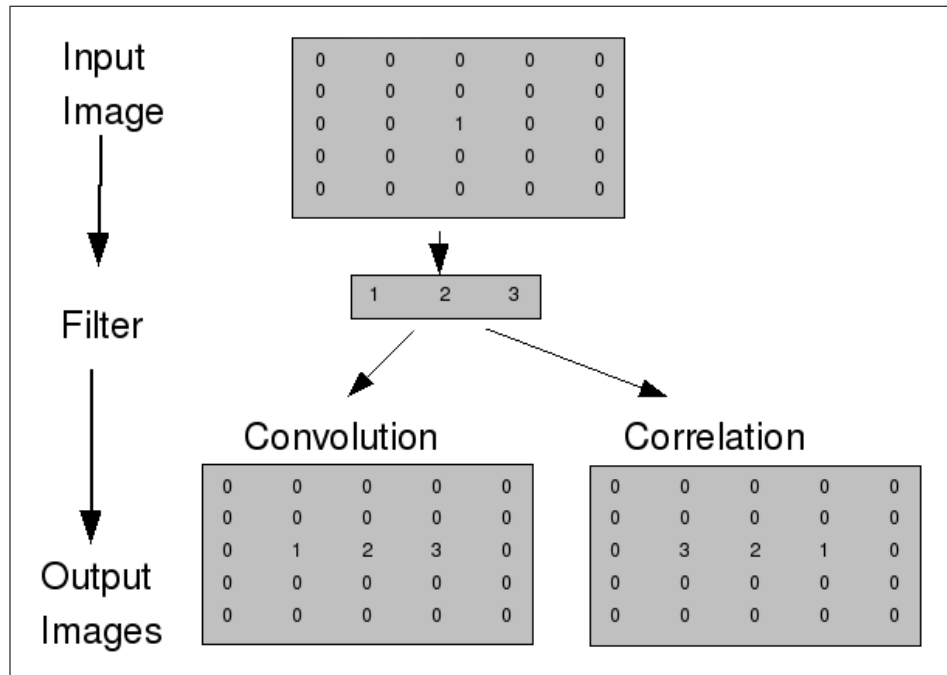


Figure 2.3: Demonstration of the difference between convolution and correlation

The process of applying a spatial filter in this way is referred to as correlation or convolution. If a convolution filter is applied to an image where the central pixel is one and all others are zero, the result would be the values of the filter in order. Applying the same filter through correlation over the same image would result in the reverse of the filter: This is demonstrated in Figure 2.3. Where the filter is symmetrical the result of correlation and convolution are the same. It is possible to combine the effects of multiple spatial filters into one such filter, which may be especially advantageous if computing time must be kept to a minimum.

### 2.1.2 Image Segmentation

Image segmentation is concerned with dividing an input image into a number of regions or objects. It is used extensively in the initial stages of autonomous object recognition algorithms and computer vision. The performance of image segmentation is central to the performance of these algorithms, as any errors at the initial stage propagate through to the end result. There are two fundamental properties that segmentation relies upon; intensity discontinuity and intensity similarity. Discontinuity in image intensity is often the result of a boundary or edge between one object and another. Therefore through the identification of an object's edge it is possible to separate this object from the rest of the image. The property of intensity similarity relies on the observation that the pixels representing an object are likely to have similar intensity values to each other and dissimilar to other neighbouring pixels. By grouping together pixels with similar intensities it is likely that the area

of the image covered by a particular object can be determined. These fundamental observations lead to two different approaches to image segmentation; edge-based and region-based segmentation.

### Edge Based Image Segmentation

Edge-based segmentation techniques aim to detect large local variations in image intensity by using a measure of the image gradient. The gradient can be calculated by taking the derivative of the image function, which in digital images is determined by using the differences in pixel intensities over a neighbourhood. The image gradient is large where there is a large change in image intensity over a small distance. Edge detection methods can use first and second order derivatives. The former tends to produce thicker edges and is less sensitive to finer variations (such as noise) than the latter. The response of first order and second order edge detection operators is shown in Figure 2.4. The general application of edge-based segmentation methods involves smoothing the input image to reduce noise, the use of an edge-detection process and a final stage that aims to select pixels that represent the true edge and reject others (for example where there is a redundancy in the representation of an edge). With the use of first order derivative edge detection methods (such as the Roberts cross, Prewitt, Sobel operators and the Canny edge detection method, (Gonzalez & Woods 2007)), edges are located by finding the maxima in the image gradient. This is normally carried out by thresholding the edge image. Second order derivative-based edge detection methods locate edges with “zero-crossings”, which relate to a zero in the second order derivative of the image gradient. These must be found in the image output from the edge detection operator. Figure 2.5 shows an image of a solar flare from TRACE, and the absolute of its corresponding output from a second order derivative edge detection filter called the Laplacian of Gaussian (LoG). As the output from the LoG filter will consist of both positive and negative values, the absolute of the output is taken for viewing purposes. In the output image the zero crossings can clearly be seen as a line of black pixels sandwiched between brighter pixels. Second order derivative-based edge detection operators are based on the Laplacian operator, and include the Laplacian of Gaussian (or Marr-Hildreth) and the Difference of Gaussian methods, (Gonzalez & Woods 2007).

The use of simpler edge detection algorithms produce edges that can be broken throughout their length. Attempts to “repair” such breakages result in more advanced edge detection methods such as the canny edge detection method (Gonzalez & Woods 2007), and such methods can significantly improve the results for image segmentation. Active contours (snakes), which we employ in this study, are based on edge detection approaches to image segmentation.

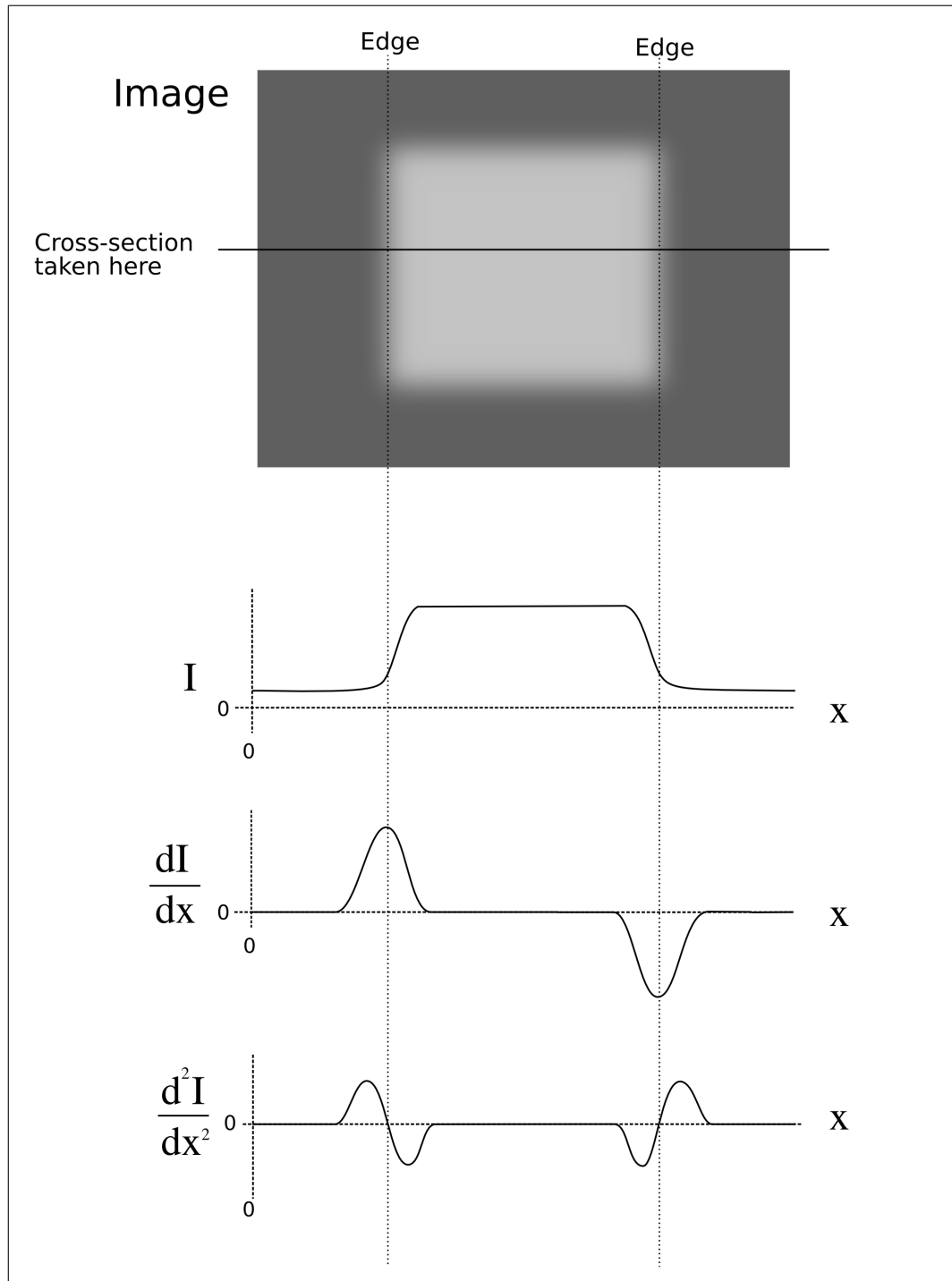
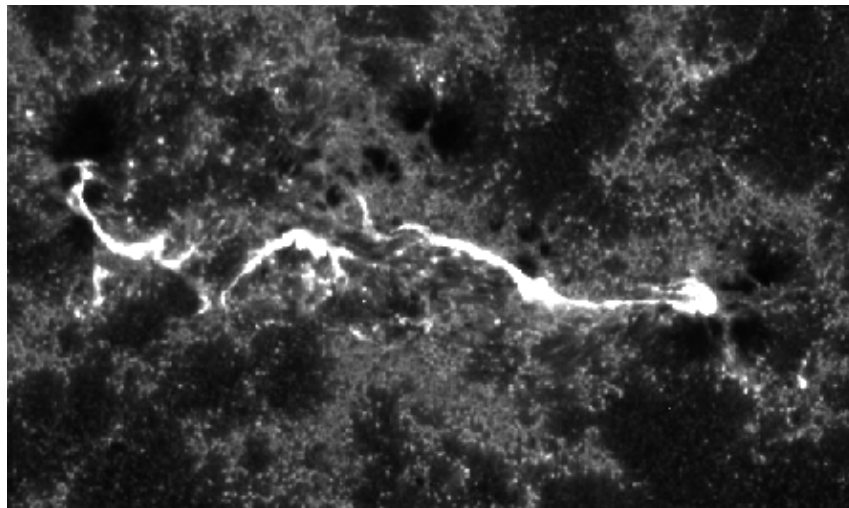


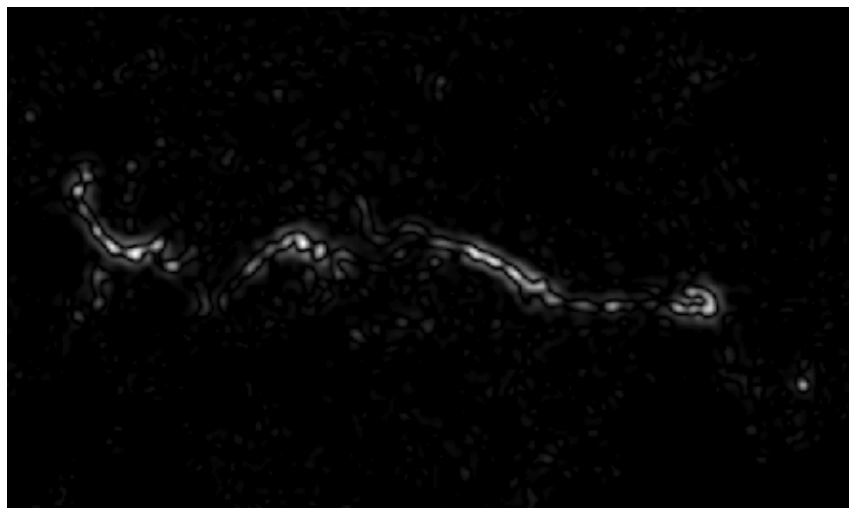
Figure 2.4: An illustration of the principles of 1st order and 2nd order edge detection. The graphs show how  $I$ ,  $\frac{\delta I}{\delta x}$ , and  $\frac{\delta^2 I}{\delta x^2}$  vary with  $x$ , along the cross section of the image shown.

### Region Based Image Segmentation

Region based image segmentation aims to group pixels in the image with similar pixel intensities. Two common approaches to region based image segmentation are thresholding and region growing. Thresholding techniques are one of the simplest approaches to image segmentation. The method compares each pixel's intensity to



(a)



(b)

Figure 2.5: TRACE images of solar flare ribbons in the 1600 Å passband, showing the original image (a), and the absolute value of the output image from a Laplacian of Gaussian edge filter with  $\sigma = 3.5$  (b). Notice in image (b) zero value pixels sandwiched between the brighter pixels, these are the zero-crossings and locate the edges in the image.

a pre-defined threshold. If the pixel's intensity is higher than the threshold it is assigned to one group, if it is lower it is assigned to another group. Due to its simplicity and computational efficiency this method is widely used, but it has limitations. If there are distinct populations of pixels in an image this method can work well, however if the populations of pixels overlap it becomes increasingly difficult to choose an appropriate threshold value and it is likely that pixels will be incorrectly categorised. Defining multiple thresholds and careful selection of the threshold value, using statistics, mitigate this problem up to a point. Further improvements can be achieved by using adaptive thresholding methods, which compute a local threshold based on the statistics of a local image area.

Region growing methods are also simple to implement and can offer an improvement over simple thresholding techniques. Region growing starts with a defined seed pixel or group of pixels to which neighbouring pixels are considered for addition based on a set of criteria. This process is repeated until the region ceases to grow or pre-defined stopping criteria are met. Criteria for the inclusion of a pixel can be its intensity value exceeding a percentage of the original seed pixel's intensity. The formulation of the acceptance criteria requires careful thought and should be tailored to the specific problem and image properties. Stopping criteria are usually based on region size and shape.

### 2.1.3 Snakes: Active Contour Models

Active contours or snakes were first proposed in 1988 in the seminal paper on the subject by Kass et al. (1988). The development was a response to low-level bottom-up methods for edge detection and motion tracking in use and development at the time. The aim was to utilise higher-level knowledge about the object being detected in combination with the lower-level image data to produce a more optimal result. Kass et al. (1988) describes snakes as: 'an energy-minimising spline guided by external constraint forces and influenced by image forces that pull it toward features such as lines and edges.' The inclusion of higher level information makes the use of snakes particularly advantageous when trying to determine the outline of an object in an image that has indistinct, discontinuous or tenuous edges. The active nature of snakes also make them particularly suitable to tracking deformable features (Menet et al. 1990). In such cases relying solely on low level image data can result in broken and discontinuous object boundaries.

In its simplest description a snake is a line comprising a certain number of nodes. There are two distinct phases in the application of snakes; the first is the formulation of the energy function, the second is the minimisation of this function. The energy function consists of data energy and model energy sub-functions. During the energy minimisation process the snake evolves by changing the position of its nodes. The energy of a node is the sum of its "data" and "model" energy. The model energy represents the high-level information and the data energy represents the low-level image information. The model energy places restrictions on the shape that the snake can take. For example, if one knew an object was elliptical in nature, the model energy parameters could restrict the snake to favour elliptical forms. The model energy of a snake usually takes the form of an elastic energy and a bending energy (Davies 2005). The elastic energy aims to restrict excessive growing or shrinking of the distance between nodes, and the bending energy aims to prevent the snake from forming excessive sharp corners and spikes. The data energy may be a function of the

image intensity and/or the image gradient at the position of a node on the image. If only the data energy of the snake is considered, the snake has no access to the high-level information, rendering it susceptible to the sharp image gradients associated with noise. The energy minimisation process should result in a compromise between the data energy that attempts to fit the underlying image, and the model energy that seeks to impart a smooth and ordered structure on the snake.

The application of snakes requires the selection of an initial position such that its subsequent evolution will allow its convergence on the object boundary. Take the example of a closed snake used to detect the outline of a circular object. If the snake has been created such that it shrinks onto object boundaries an appropriate initial position would have all points of the snake outside the object boundary. Similarly a snake that evolves by expanding outwards would need to have an initial position inside the object boundary. This expanding or contracting evolutionary behaviour of a snake can be dictated by choosing a suitable formulation of the model energy parameters or by the addition of an external force/pressure parameter. The total energy for the snake is computed by summing the energies of the individual nodes. Applying a snake to an image aims to minimise this total energy. Shortly after the publishing of (Kass et al. 1988) a new algorithm was proposed by Williams & Shah (1990) with the primary goal of creating a faster process for the energy minimisation. The process of the proposed “greedy algorithm” as it was named is used as a template for the development of our snake. The “greedy” approach takes each node of the snake in turn and considers a new position for this node. If the new position of the node reduces the overall energy of the snake it is moved to the new position, but if it does not it remains where it is. Each node in turn is considered, and the process is repeated, until an upper limit on the number of iterations or no further reduction in energy can be achieved. This process normally has the result that a snake can find a local minimum in its energy function, but this is not necessarily the global minimum (Davatzikos & Prince 1995). Although this may sound like a disadvantage of using snakes, it should be noted that this is a necessity if trying to find two different edges in the same image, as these two edges represent two different local minima. Williams & Shah (1990) also review different ways of calculating the snakes model energy, and introduce the concepts of continuity and curvature terms for the model energy function, their work in this area is again used as the basis for our snake.

There are some well-known problems with the use of snakes, one of which is due to the localised nature of image gradients. This localised nature means that a snake must get within a few pixels of an image edge before its effect is felt and the snake is drawn to the edge. This is known as the initialisation problem. This is not a problem if the initialisation of the snake is performed by a user who can ensure

that the snake is initialised suitably close to the object boundary. One common response to the initialisation problem is to smooth the image so that an object's edges are expanded and so increasing the "capture range" of the edges, however there is a limit to the extent to which the image can be smoothed before losing all relevant detail and in most cases the increase in capture range is not sufficient to completely resolve the issue. Another problem often encountered is fitting a snake to the concave regions in an object's boundary (Davatzikos & Prince 1995). A response to both of these problems makes use of "pressure forces" as in Cohen (1991). Such forces can be employed in a closed snake to cause it to expand or contract onto image edges, and in an open snake to move in a certain direction until it reaches image edges. These pressure forces can also be used to help a snake "inflate" into concave regions. There is a drawback to using pressure forces, as the forces employed must be sufficiently strong to propel the snake onto the image edges and possibly pass over weaker image edges, whilst remaining sufficiently weak so as not to propel the snake over the stronger image edges (Tek & Kimia 1995). Xu et al. (1994) observe that if the parameters and initial position are not chosen correctly "the contour fails to converge to desirable edges" and a circular trial and error approach is then necessary. A different approach to the initialisation problem is that of (Leroy et al. 1996) who propose multi-resolution algorithms that employ images of different resolutions to provide a capturing force for the snake when at large distances from image edges. This method also brings the added benefit of reduced computational time, and whilst it resolves initialisation problems it creates a snake which is sensitive to the progression from the coarse to fine resolutions. A development by (Xu et al. 1994) seeks to counter the effects of the model energy function that act as a force normal to the snake at every point along its length. This method has had considerable success and produces a snake that is no longer sensitive to its initialisation and model energy terms, but has the limitation that the resulting snake is no longer as smooth and subsequently performs poorly where there are gaps in image edges. This drawback renders the approach unsuitable for our application. Of the more promising advances in snakes is the gradient vector flow snake as proposed by (Xu & Prince 1998). This method claims to resolve initialisation and concavity issues. It does this by defining a Gradient Vector Flow (GVF) field that points toward the object boundary when close by and varies smoothly over homogeneous areas of an image. The results are image forces that propel a snake to an image edge from anywhere on the image, and where present, into the apex of concave regions in the object boundary. To visualise the GVF field and the motion of a GVF snake see Figure 2.6.

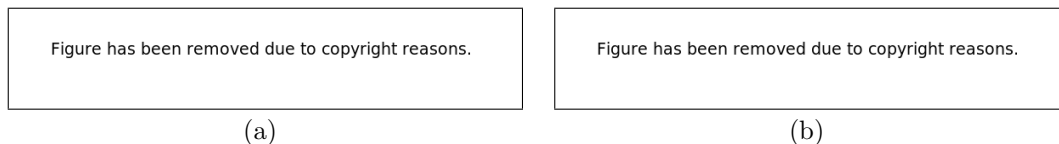


Figure 2.6: Image showing the image forces of (a) a conventional snake, and (b) a GVF snake. Note how the forces of a conventional snake are restricted to a small region surrounding the image feature and would prevent a snake from entering the concave region of the image feature, but the GVF snake forces extend to the image boundary and would draw a snake into the concave region. Images from Xu & Prince (1998).

## 2.2 Image Processing in Solar Physics

### 2.2.1 Introduction

Astronomy has always been an active area for image processing research, mainly due to problems caused by a lack of photons available for imaging most astronomical objects. Within astronomy the area of solar physics does not suffer from such a lack of photons, instead image processing developments have been driven by other factors. One of these factors is the large quantities of image data currently available and the even larger volumes of data soon to arrive. The planned Solar Dynamics Observatory (SDO) mission is expected to collect 1.4 TByte of data per day (Paton et al. 2008), which equates to 2 petabytes over its 5 year mission (Hurlburt et al. 2009). Making full use of this amount of data presents a formidable task best approached with the use of autonomous or semi-autonomous analysis. The importance of automating the analysis of this vast dataset is indicated by NASA's funding of a "large international consortium" to develop automated feature recognition software specifically for application to SDO images (Martens et al. 2009). The other factor is the increasing need for space weather forecasting that has arisen with an increase in activities in space. Space weather forecasting requires near real-time analysis, which can be most efficiently achieved by using autonomous computer based algorithms, examples include CACTus (Robbrecht & Berghmans 2004; Robbrecht et al. 2006, 2009) and SolarMonitor.org (Gallagher et al. 2002, 2007). The increasing importance of image processing in solar physics is demonstrated by a large number of published articles detailing the application and formulation of image processing techniques and a biennial event - the "Solar Image Processing Workshop" (Anon. 2009b), which was first held in 2002. The main applications of image processing in solar physics can be categorised into image pre-processing and enhancement, together with feature detection and classification.

Figure has been removed due to copyright reasons.

Figure has been removed due to copyright reasons.

(a)

(b)

Figure 2.7: An example showing an image degradation by cosmic ray hits (a), and the cleaned result (b), from (Marshall et al. 2006).

### 2.2.2 Pre-processing and Enhancement

Image pre-processing and enhancement are mainly employed prior to further analysis of image data. They can be used to correct for degradation or to enhance a feature of interest. For example when looking for a coronal mass ejection (CME) in coronagraph images, some images may suffer degradation as a result of high energy cosmic rays hitting the instrument's charge coupled device (CCD). Such degradation can present a problem for further image analysis whether by human observer or subsequent computer based algorithms. Figure 2.7(a) shows an image degraded by cosmic ray hits, and Figure 2.7(b) shows the result of a cleaning algorithm developed by Marshall et al. (2006) using soft morphological filters. Another example of image pre-processing is the spatial correction of images where the capture process has resulted in a distorted image, as in Zharkov et al. (2005). Geometrical transforms may also be used to aid visualisation and interpretation (Robbrecht & Berghmans 2004). Image enhancement is often used in automated feature recognition before the actual image segmentation stage and is used to amplify the signature of a particular feature, as in Bernasconi et al. (2005), where advanced sharpening methods are used to increase the contrast between solar filaments and the image background before attempting the detection of filaments. There are many standardised pre-processing methods routinely employed in solar physics, as well as new methods being developed.

### 2.2.3 Automatic Feature Detection and Classification

Automated feature recognition and classification algorithms have been developed and applied to a large number of solar phenomena including; coronal loops, coronal holes, CMEs, filaments, prominences, sunspots, bright points, granular boundaries, supergranular boundaries, active regions and flares. In the recent past the main method employed for identifying such features in solar imagery has involved an experienced observer visually inspecting the images and manually recording the observed features. The labour intensive and subjective nature of such an approach has led the solar physics community to seek collaboration with the image processing and computer vision specialities. The development of automated software for this task promises to complete analysis quicker, provide a more objective analysis and reduce

the input needed by the observer. The time and resources taken for the compilation and analysis of large datasets can be reduced drastically by employing automated algorithms. It is common practise for these algorithms to have several pre-processing steps aimed at achieving the optimal image prior to segmentation. Work dedicated to producing this optimal image is worthwhile owing to the inherent difficulty of image segmentation. The methods of region growing and thresholding discussed in Section 2.1.2 represent the simpler approaches to image segmentation and are commonly used either on their own or in conjunction with other segmentation methods. This is particularly the case where the feature in question appears as a reasonably coherent area of darker or lighter pixels in the image, such as sunspots (Chapman & Groisman 1984; Steinegger et al. 1990; Chapman et al. 1994; Preminger et al. 2001; Curto et al. 2003; Zharkov et al. 2005; Colak & Qahwaji 2008), or solar filaments (Qu et al. 2005; Aboudarham et al. 2008; Scholl & Habbal 2008; Shih & Kowalski 2003; Gao et al. 2002). More advanced methods are needed where the features being analysed are not well defined or homogeneous, for example active regions where methods include; disjunctive granulometric filtering as used by Shih & Kowalski (2003), the use of the fractal dimension with fuzzy-based segmentation by Revathy et al. (2005), wavelet analysis by Delouille et al. (2005) and mulitscale methods by Conlon et al. (2008); Hewett et al. (2008). Solar flare ribbon tracking is an area with only a few published methods, Saba et al. (2006) and Qu et al. (2004b), both use region growing or thresholding as the principal method for detection, although Qu et al. (2004b) supplement this with edge based detection.

## 2.2.4 Methods for the Tracking of Solar Flare Ribbons

### Manual Approach

The simplest approach to flare ribbon tracking is to manually trace the position of the flare ribbons in each image. This is usually done using a computer: With the image on screen the user can trace the mouse cursor over the ribbons and record a series of mouse clicks to define each ribbon in turn. The problem with this method is not its accuracy, but the time taken to produce the result. This limits studies to smaller datasets, which in turn restricts the statistical analysis possible. Another manually based approach is used by Fletcher et al. (2004) to track the individual footpoints that make up a flare ribbon. The method requires the user to identify a bright footpoint in the ribbon with a mouse click, a tracking box is drawn around the feature and a 2D Gaussian curve is fitted to the intensity profile of the bright feature. The tracking box is carried over into the next image, and a 2D Gaussian is fitted to the brightest feature within the tracking box. The box is then repositioned so its centre is at the centre of the Gaussian and the process is repeated. If the

bright feature moves more than a specified distance the process stops and the user must again select the feature manually. This is repeated for all bright points in the images. In this way the motion of the footpoints builds a picture of the ribbon movement as a whole.

### **Semi-Automated Approach**

Saba et al. (2006) present a semi-automated approach to the analysis of flare ribbon evolution, with a clear emphasis on the inferences of the data obtained rather than on the methodology employed. As our primary interest in this thesis is with image processing methods, we will focus on their methodology. The images used are TRACE 1600 Å of a flare that occurred on 23 November, 2000, together with MDI magnetograms from Solar and Heliospheric Observatory (SOHO). The first step of this semi-automated process is to identify the flare ribbons. This was performed by a simple thresholding method where all pixels above a certain level were added to a mask defining a flare ribbon and those that fell below the threshold were defined as not belonging to a ribbon. The threshold level was chosen by an observer through trial and error and inspection of image intensity histograms. The output was a mask for each image showing the pixels that belonged to a ribbon. Additional masks were created by comparing two ribbon masks from separate images, the newly created masks being the growing difference mask, the fading mask and the union mask. The growing difference mask highlights pixels present in the current ribbon mask but not in the previous; the fading mask shows pixels that are present in the previous ribbon mask but are not present in the current; and the union mask shows all pixels that are present in the previous ribbon mask and all pixels present in the current ribbon mask. Each ribbon mask was manually examined and any unwanted artefacts were manually removed. Magnetic reconnection rates were calculated by using the pixels from the growing difference mask and overlaying these onto the associated magnetogram. The magnetograms were co-registered with the TRACE images prior to the overlaying of the masks. The co-registration was carried out with the region immediately around the flare only, as the different perspectives of the SOHO and TRACE satellites meant additional local distortion of the images would have been necessary to produce a complete match over the whole image. At each point in time represented by an image, the sum of the magnetic flux intercepted by the pixels of the corresponding growing difference mask was calculated. No comparison with manual methods for tracing flare ribbons is presented, although efforts are taken to examine the errors. A quick estimate of the errors that could result in the calculated magnetic reconnection rate is computed by shifting the magnetograms by 2 pixels and repeating the process. The resulting reconnection rates were found to be within 20% of the original values. The threshold value (originally set at 500 DN)

was changed within the range of 400 to 550 DN and again the magnetic reconnection rates were found to be within 20% of the original calculated values. The authors conclude that such a method can be a useful tool for ribbon analysis, and that it can provide a more objective approach than a user-dependent point and click approach. They also realise the limitations of basing the detection of ribbons on a threshold alone, and point out that application of this method is only useful when carried out by someone who has studied the flare in detail and concede subjective intervention may be needed.

### **Fully Automated Approach**

A fully automated approach to flare ribbon tracking is discussed in Qu et al. (2004b). This paper, titled “Automatic solar flare tracking using image processing techniques”, briefly describes how the authors are able to detect and characterise a solar flare in  $H\alpha$ , as presented in their paper published earlier in the same year (Qu et al. 2004a). They then used this result of the detection algorithm for tracking the flare ribbon evolution. This result was the location of the centre of the solar flare, which was obtained through the location of a “key pixel” in a flare image. The key pixel was identified as having the maximum grey level difference between its value in the current image and the previous image.

Pre-processing was carried out to remove noise and align the images. The first image in a sequence was segmented to find the flare ribbons. The segmentation process used region growing, boundary based detection, morphological processing, small-part removal and hole filling. With the flare ribbons identified in the initial image the algorithm then tracked the evolution of these ribbons over the remaining images in the sequence. The algorithm is summarised in the flow chart produced by Qu et al. (2004b) and reproduced here in Figure 2.8. The following detailed description of this algorithm is set out in these 6 distinct sections.

**Figure has been removed due to copyright reasons.**

Figure 2.8: Flow chart summarising steps used in the automatic tracking of flare ribbons, from Qu et al. (2004b).

The pre-processing methods employed include a median filter and a soft morphological filter. As full-disk images were used for this algorithm the images were aligned by matching estimates of the disk centre between images. The algorithm selected a region of interest of pre-determined size centred on the key pixel, and

created a new set of images from this. These new images were normalised to the average image intensity of the entire image sequence. One of the images used by Qu et al. (2004b), is shown in Figure 2.9.

Figure has been removed due to copyright reasons.

Figure 2.9: One of the original (i.e. unprocessed) images used by Qu et al. (2004b) in developing their algorithm, from Qu et al. (2004b).

The algorithm then identified the flare ribbons in the initial image, which was achieved by applying region growing followed by boundary based methods. Region growing selected the brightest pixel in the image as the seed, and accepted new adjacent pixels into the seed region if their intensity was 80% (or more) of the seed. Multiple regions were grown resulting in a number of rough edged patchy regions in the image. The boundary based methods were then employed to add to the result of the region growing. This process relied on the adaptive thresholding of an edge map of the image, which resulted in an edge map of locally strong boundaries/edges. Pixels on the bright side of the boundaries were used as seeds for further region growing, with the criteria set to accept a pixel if its intensity was equal to or greater than the seed. The results of these processes are shown in Figure 2.10

Figure has been removed due to copyright reasons.

Figure has been removed due to copyright reasons.

(a)

(b)

Figure 2.10: Images showing the results of region growing (a), and region growing combined with boundary based methods (b), from Qu et al. (2004b).

Refinement of the segmented regions is carried out using morphological processing and small part removal and hole filling. The morphological closing utilised a square 3 by 3 structuring element, and was used to fill gaps in the edges and fuse separated neighbouring regions. Hole filling and small part removal methods rely on the identification of image components, where a component may either be a discrete region or a hole in such a region. Once a component was identified it was either removed or filled if its size fell below a certain threshold. The processed images from this step in the algorithm are shown in Figure 2.11.

With image segmentation complete, the flare ribbons in the initial image were represented by many fragmented components. To track the ribbon separation the algorithm produced one component that was representative of the entire main body of the flare (i.e. all components and so both flare ribbons), this is referred to by the authors as the flare model. Components whose minimum separation distance

Figure has been removed due to copyright reasons.

Figure has been removed due to copyright reasons.

(a)

(b)

Figure 2.11: Images showing the results of morphological closing (a), and small part removing and hole filling (b), from Qu et al. (2004b).

fell below a certain threshold were merged, and from the remaining components all but the largest three were rejected. Morphological closing with a large element was then applied to fill the remaining gaps between the components, resulting in the flare model. The algorithm examined components in the second image in the sequence for any overlap with the model from the first image. Only components that overlapped were used in the creation of the model for the second image. Any holes in the second image model were filled, and the process was repeated iteratively for all images in the sequence. With a flare model for each image the algorithm matched the edge pixels of each model from one image to the next and computed a vector describing these pixels' apparent movement. The model edge pixels were paired if they overlapped, or by finding the closest edge pixel if they did not overlap. For each pixel pair the apparent trajectory and distance from one image to the next was calculated. The mean apparent distance was recorded for each pair of correlated pixels in direction based bins of 10 degrees. By counting the number of pixels recorded in each angular bin the algorithm then made an estimate of the average direction of the ribbon motion, and an average speed was calculated by taking a difference between two averaged expansion distances and dividing this by the time separating the two image exposures. Images showing the result from component labeling and the creation of the model are shown in Figure 2.12.

Figure has been removed due to copyright reasons.

Figure has been removed due to copyright reasons.

(a)

(b)

Figure 2.12: Images showing the results of component labeling (a), and showing the created flare "model" (b), from Qu et al. (2004b).

The time taken to run this algorithm per image, as tested by the authors on a computer with a processing speed of 733 MHz, was under 20 seconds per image, which is fast enough to provide an advantage over manual methods. It should also be noted that this algorithm was developed using the Interactive Data Language (IDL) by Research Systems Inc. a language not noted for its processing speed. The accuracy of this algorithm was tested against results obtained by an observer manually tracing the flare ribbons. The comparison of the separation distances and the

calculated electric field (using the ribbon velocity and the line of sight magnetic field) are represented graphically and are included here in Figure 2.13. The separation distances from the algorithm mostly lie within the given error bars of the manual method, although over two distinct time periods the algorithm's distances drift from the manual distances by more than the given error bars. The graphical comparison of the calculated E-fields also show an approximate match, although the algorithm's results show many more narrow peaks in the E-field over time than the manual method. These narrow peaks are in most cases outside the associated error bars.

The strengths of the algorithm in the view of the authors is; firstly that it is not as dependent on finding the leading edge of the flare ribbons (something which can be considered subjective due to the tenuous nature of this edge), and secondly that a more accurate average is obtained by considering all the pixels in the flaring area of the image. They also point out that noise in the images can adversely affect the result from their algorithm. The data used for the authors' tests was a  $H\alpha$  image, which, judging by the appearance of the image presented in this paper, appears devoid of any post flare loops or network, features which appear in flare images used by our algorithm and complicate the task of automated ribbon tracking. The paper also only tests the algorithm on one flare and one set of images, a more subjective view of its performance could be obtained by testing on different flares and using images from different wavelength bands. The strength of this algorithm may lie in its use and combination of both region and edged based segmentation methods.

**Figure has been removed due to copyright reasons.**

**Figure has been removed due to copyright reasons.**

Figure 2.13: Graphical illustrations of the differences in ribbon separation and the calculate E-field between the automated algorithm developed by the author and a human observer, from Qu et al. (2004b).

## 2.3 Summary

This chapter has provided an introduction and overview of image processing, in particular image segmentation and edge detection, and its application to solar physics.

---

The general overview of image processing use in solar physics, together with the more detailed look at flare ribbon tracking methods, sets the context for the development of our snake algorithm. The background to image processing establishes some important basic concepts the reader will find useful for the following chapter, which discusses the initial development and design of our snake algorithm, and details of the pre-processing applied to our flare data.

# Chapter 3

## The Snake Algorithm

This chapter begins with a section describing the pre-processing that we have applied to our flare data prior to its use with our algorithm. We follow with an overview of the initial development of our algorithm, where we discuss the formulation of the energy function, the method we use for finding a minimum to the energy function, and the method used for edge detection. The final section outlines the various parameters and factors that can affect the performance of the algorithm, and the effects are demonstrated with examples using a simulated test image.

### 3.1 Image Pre-processing

In order to use TRACE images, we must first correct the images for some instrumental effects. Many of these effects are caused by the TRACE CCD, and are common to all CCD imagery. These effects have been studied in great detail since the inception of the CCD, and as such are understood well enough to enable their effective removal. The calculation and removal of these effects is a normal part of dealing with data from instruments such as TRACE, with routines available through the SolarSoft suite of software (SSW) for their application (Freeland & Handy 1998). We also discuss other corrections not caused by the TRACE CCD, and comment on their importance and relevance for our use, namely image registration/alignment and the removal of cosmic ray hits.

#### 3.1.1 Standard Pre-processing

The following section describes a number of standard pre-processing methods applied to our data. As these methods are standardised there are routines in SSW developed for their specific application to TRACE data. Unless otherwise stated we have used these routines for the pre-processing of the TRACE data used in this project.

### Dark Current

A CCD produces an image by detecting an increase in voltage at a pixel location (often called pixel “well”), caused by incident photons moving electrons in the semiconductor of the CCD into the conduction band, due to the photoelectric effect. Due to thermal energy of the sensor, electrons can be freed by thermal agitation rather than by incident photons, causing the CCD to read a certain amount of background noise, even when there are no incident photons. This is intuitively referred to as the “dark current”, and again intuitively the amount of dark current depends on the temperature of the sensor. The TRACE CCD is passively cooled to  $-65\text{ }^{\circ}\text{C}$  to minimise this noise. This noise source is well understood, and it is commonplace to correct raw astronomical images to remove the effects of this dark current.

### ADC Offset

The output signal from a CCD is an analogue voltage, which is then converted to a digital signal by an analogue to digital converter (ADC). The actual signal from the CCD is a minor contribution to the overall output voltage, and as such part of the ADC process is to subtract a reference voltage from the output voltage of the CCD. The remaining voltage can then be converted into a sensible digital number (DN), with any changes in signal showing up as significant changes in the digital number. There is a problem with this however, if for example the overall voltage which the ADC receives from the CCD drops, and we continue to subtract the same baseline voltage from this output. Then the analogue value to be converted may drop below zero, which is a problem for the ADC. To overcome this problem, a small offset voltage is added prior to analogue to digital conversion. This added offset voltage is referred to as the ADC offset. The value is usually known for a CCD, and its equivalent digital value can be subtracted from the resulting digital image to remove its effect from this image.

### Flat Field

Flat fielding actually refers to a correction method rather than an instrumental effect. It is such a commonplace correction it is even used in compact digital cameras. The purpose of a flat field correction is to adjust the CCD output such that a uniform signal across the entire CCD will produce a uniform output. This is not normally the case without a correction applied. Individual pixels in a CCD will normally give a different signal compared to another pixel on the same sensor for the same input signal, the term “gain” is used to describe how much output is generated by the signal input and is usually given as a simple ratio between input and output. The basic idea of flat fielding is to expose the CCD to a uniform signal, and then

using the output 2D image with the knowledge that this image should be uniform, the amount by which each pixel's output differs from the uniform output can be calculated. These values are constructed into a flat field 2D image, and are usually normalised so that a pixel needing no correction has a value of 1 in the flat field image, so that dividing an uncorrected image results in a "gain calibrated" image. TRACE flat fields are calculated using Kuhn-Lin flat-field algorithm (Handy et al. 1999), and are available to the solar community to download. SolarSoft routines are also freely available that apply appropriate flat field corrections to TRACE images.

Note that a pixel's gain can vary with time. The TRACE CCD uses a Lumogen coating applied to the CCD to enable the detection of UV and EUV photons. This coating is expected to degrade with time due to the cumulative effects of EUV exposure (Handy et al. 1999).

### **Normalising for Exposure**

TRACE exposure times are controlled on-board in order to prevent saturation of the CCD during an event, and can be triggered in a number of ways. The implication of this exposure control is that some TRACE images of a flare may have different exposure times to others of the same flare, resulting in the pixel intensities in the images not being representative of the feature brightness when comparing one image to another. As we will be using sequences of images, and using pixel intensity values from these images, it is important that the pixel intensities are corrected for exposure time. We have used the shutter duration information contained in the FITS file header to normalise all images to a 1 second exposure. Note that the shutter duration values are prone to inaccuracies, the inaccuracy is thought to be roughly a constant value independent of exposure time, and is therefore more of an issue for images taken with a small exposure time.

### **3.1.2 Non-Standard Pre-Processing**

The pre-processing techniques discussed here may well be considered standard by many observers, they are marked out as non-standard here as it was not immediately obvious whether the TRACE data used in this project should be processed in these ways. We include discussion and justification for these pre-processing methods and their application to our TRACE data.

#### **Removing Cosmic Ray Hits**

Energetic charged particles (often referred to as cosmic rays) accelerated by explosive events in the solar atmosphere find their way into the TRACE telescope and reach the CCD, causing some CCD pixels to output a large signal. An individual cosmic

ray hit shows up in images as a small bright spot if its trajectory is normal to the CCD, and as a bright streak if its trajectory is off the normal to the CCD. The majority of these energetic particles that enter the TRACE telescope are thought to do so as TRACE passes through the Earth's radiation belts, where they are trapped in higher than normal densities. Cosmic rays hitting the TRACE CCD usually appear in groups, where the number of cosmic ray hits in an image sequence is observed to start low before gradually peaking and then decreasing, possibly due to TRACE passing through regions of lower and higher densities of energetic particles as it passes into, through and then out of a radiation belt. The effect of numbers of cosmic rays impacting on the TRACE CCDs is to add a "salt and pepper" type noise to the image, as shown in Figure 2.7(a) from Section 2.2.2. Our active contour algorithm is highly dependent on pixel intensity and large image gradients, suggesting that the noise characteristic of cosmic ray hits could have a strong impact on our algorithms ability to locate the flare footpoints. Different approaches to removing cosmic rays hits from images have been developed, some of these are included in SSW. The crux of the problem in removing the resulting noise is identifying what is a cosmic ray hit and what is a bright solar feature. Some methods for removal of this noise use a sequence of images, and identify cosmic ray hits as bright pixels that appear in one image but not in other images in the sequence. This is the approach used in the SSW routine applied to our data. Care must be taken when using this algorithm on images of flares, as certain features of solar flares can appear very bright, may be small, and may also be transient in nature, hence they appear similar to a cosmic ray hit and are consequently removed from the image(s). As our algorithm is only designed for detecting the flare footpoints, it is not a concern if for example the bright tops of a loop are removed from the image, but obviously if the footpoints themselves are removed this will cause our algorithm some problems. Also it should be noted that if some part of the flare is removed and replaced by dark pixels, this may create a large image gradient along the edges of the removed feature, and as our algorithm is very sensitive to image gradients this could cause a problem. With these thoughts in mind we have applied a de-spiking routine from SSW to our data, but have been careful to compare the cleaned images against the uncleaned images to check no footpoints have been removed, and no areas of high image gradient are created. If a cleaned image does show these negative impacts from the de-spike routine, then we subsequently make a qualitative judgement on whether the cleaned image or uncleaned image is preferable. This is currently an unavoidable problem with using TRACE data, but with data from future instruments with better spatial and temporal resolution this may not be as much of a problem.

## Image Registration

It is necessary to ensure that the images used are co-aligned to the best of our ability. Our algorithm uses the final tracked ribbon position from one image in the detection of the ribbon in the next image, and so any mis-alignment of images in the sequence could result in errors. Mis-alignment may arise due to drift in the TRACE telescope pointing, as discussed in Fletcher et al. (2004), and also due to solar rotation. By applying a cross correlation algorithm to two images it is possible to estimate a vector that describes the offset of image (b), compared to image (a). By shifting image (b) by this offset vector the images are co-aligned.

When discussing the application of the results from our algorithm, it became clear that a lot of its benefit will come by observing the evolution of the ribbons and by comparing the tracked ribbon positions with other data, such as line of sight magnetograms from MDI or white light images. Clearly when observing the evolution of one ribbon position with another in a previous image the observer should be certain that any perceived movement of the ribbon is due to actual ribbon movement and not due to mis-alignment of the images. When comparing features on other images (for example sunspots) with flare ribbon position and morphology it is clear that the positions of the images must be accurately co-aligned to be of use, and again it is important that any perceived patterns or behaviour are due to the actual evolution of the ribbons and not errors in the image alignment.

## 3.2 Formulation of our Algorithm

### 3.2.1 Basic Design

The basic design of our algorithm is shown in Figure 3.1 in flow chart format, and is similar to that of the Williams & Shah (1990) greedy algorithm. Its aim is to find a minimum in the energy function of the snake. This energy function is designed such that it returns a low value when the snake is in a desirable position on the image and the nodes of the snake are in a desirable configuration with respect to each other. A high value is returned when the snake is in an undesirable configuration. The energy function is comprised of a model energy function and a data energy function.

The model energy function calculates the energy of the snake based on the position of the nodes relative to each other, and has no input from the image. The role of this model energy function is to impart some rigidity, smoothness and elasticity to the structure of the snake.

The data energy function is based on the image data and a preferred direction of movement for the snake (as referred to in Section 2.1.3 as “pressure forces”). It consists of three separate sub-functions; the image intensity sub-function, the

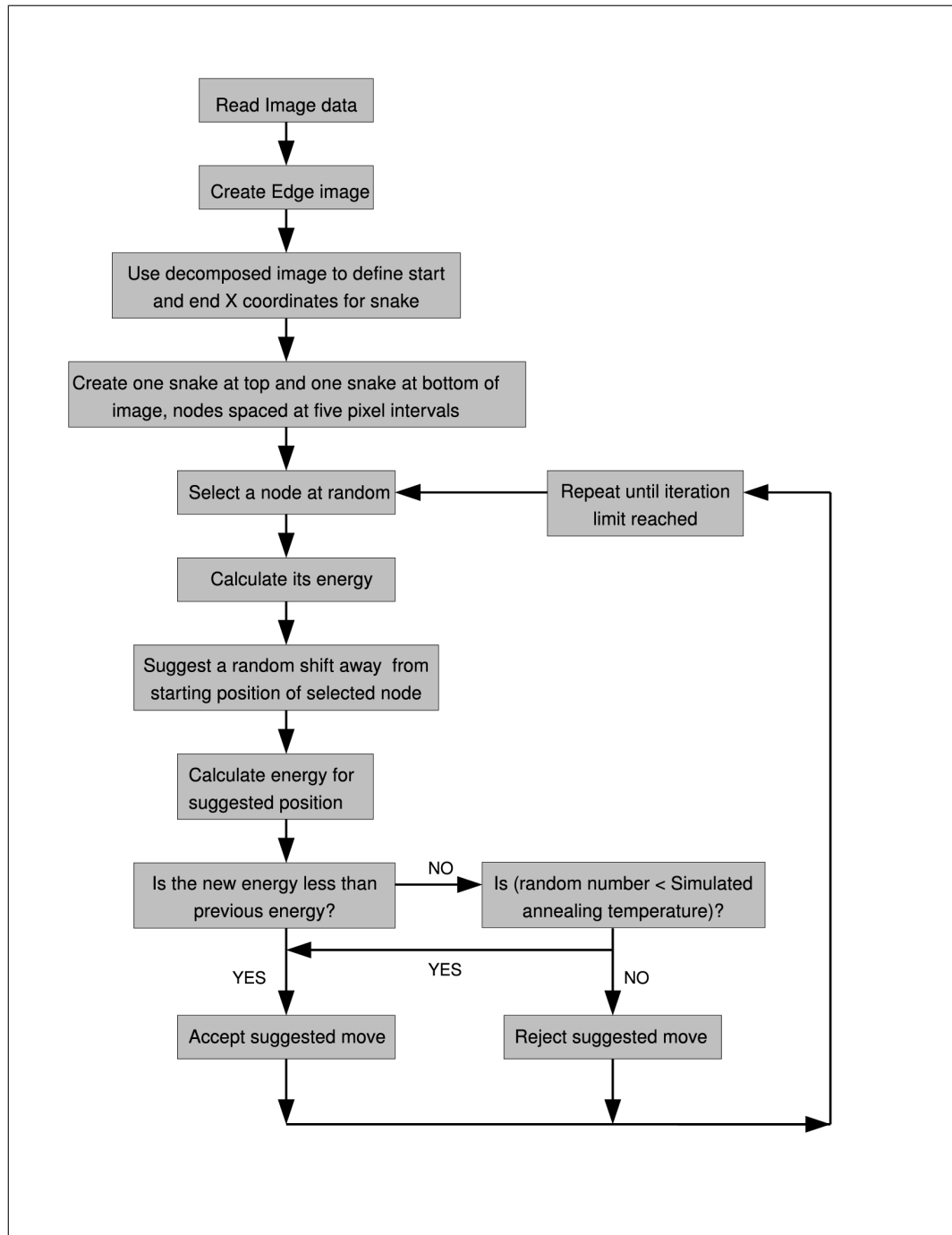


Figure 3.1: Flow chart showing the basic design of our snake algorithm.

image gradient sub-function, and the pressure sub-function. The image intensity sub-function aims to draw the snake to bright pixels in the image, and the image gradient sub-function aims to draw the snake to locations where the image gradient is large. The pressure sub-function aims to propel the snake away from its initial position in a certain direction. Where the snake's initial position is at the top of the image the pressure force, referred to from now simply as "pressure", acts to push the snake downwards, and where the initial position is at the bottom of the image

the pressure acts to push the snake up the image.

Consider a snake initialised at the top of an image, this snake consists of a number of linked nodes spanning the width of the image. For this simple case consider a linear horizontal bright feature spanning the entire width of the image, representing the flare ribbon which we aim to locate with our snake. One node from the snake is selected at random and its energy is calculated based on its current position by the energy function. A new position further down the image is then suggested for the node. The distance between the node's suggested position and the node's current position is random, but is limited by a maximum possible value of the order of a few tens of pixels. The energy is calculated for the suggested position of the node. If this energy is less than the energy associated with the node's current position the node moves to the suggested position. This process is repeated iteratively so that all the nodes are selected many times and until no nodes can move any further. Where the node lies on the bright linear feature its energy will be low, and any suggested new positions for the node will result in an increase in energy and so the node remains on the linear feature. The process is repeated with a snake starting at the bottom of the image and moving upwards.

A more detailed description of the formulation of our snake algorithm is discussed in the following sections. For the initial stages of development for our algorithm we used a simulated image rather than actual flare data. The simulated test image was created using the GNU Image Manipulation Program, and aims to replicate a flare ribbon. To replicate a flare ribbon a random jitter is imposed on the structure of the simulated ribbon, and its edges are blurred to simulate the affect of the point spread function of the TRACE telescope. The whole image is then speckled with a random 'noise'. The evolution of the snake on this simulated test image can be seen in Figure 3.2.

### 3.2.2 Formulation of Model Energy Function

The model energy function of the snake has two purposes. It must impart a rigidity and smoothness to the snake and it must prevent the snake from exhibiting excessive shrinking or growing of the distance separating the nodes. The function for the model energy of the snake must return a low value when the nodes of the snake are in a desirable configuration, and must return a high value when they are in an undesirable configuration. This behaviour of the model energy function will enable the selection of desirable configurations through energy minimisation. The model energy function is split into two sub-functions; one seeks to impart rigidity and smoothness to the snake and is referred to as the curvature sub-function, the other seeks to impart elasticity to the snake (i.e. prevent excessive shrinking or growing

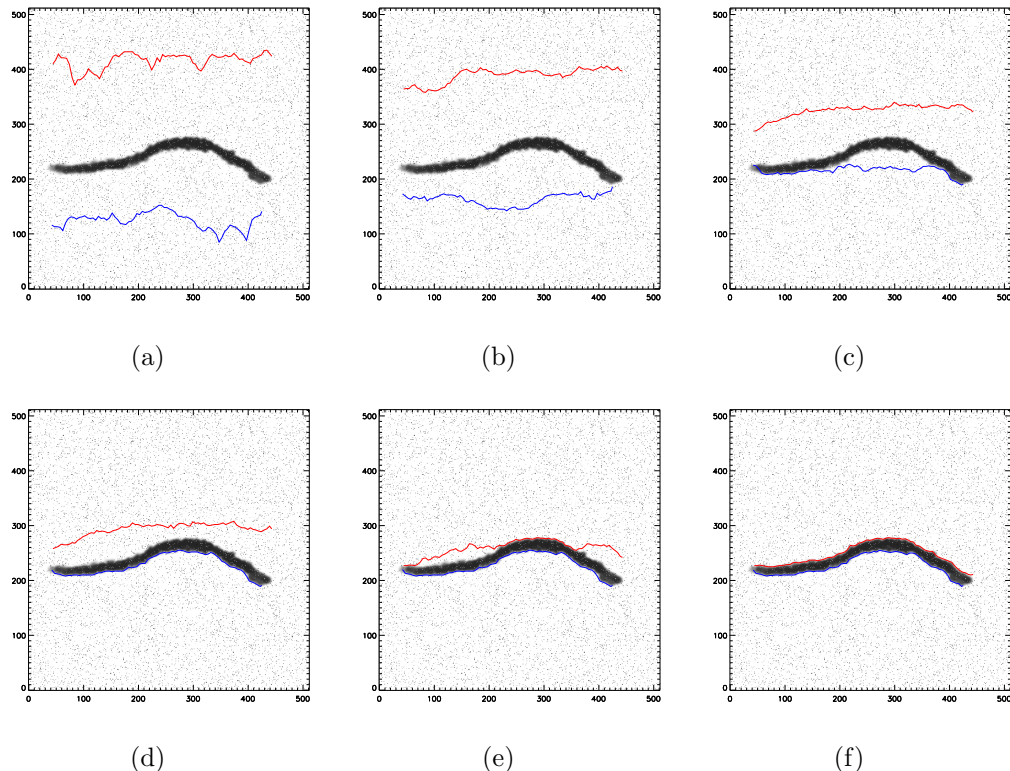


Figure 3.2: Figure showing snakes as they move over the simulated test image onto the simulated test ribbon. Note the snake shown in red starts at the top of the image, and the snake shown in blue starts at the bottom of the image. Image (a) show the snakes shortly after their initialisation, the following images show the snakes at increasing time intervals after (a), with (f) showing the snakes once they have come to rest.

in the distance between nodes) and is referred to as the continuity sub-function. The continuity and curvature sub-functions have received some attention in early implementations of snake algorithms, most notably by Williams & Shah (1990) who examine a number of different methods, including those used by (Kass et al. 1988). The functions we have used are the same as those chosen by Williams & Shah (1990). Where the snake is represented by a vector written as  $v(s) = (x(s), y(s))$ , the continuity part of the model energy function is written as:

$$cont = \hat{d} - |v_i - v_{i-1}|, \quad (3.1)$$

where  $\hat{d}$  is the average distance between nodes of the snake. This continuity term returns zero if the distance between the current node and the next node in the snake is the same as the average node separation, and increases with the difference between this distance and the average node separation. The curvature part of the model energy function is written as:

$$curv = |v_{i-1} - 2v_i + v_{i+1}|^2. \quad (3.2)$$

When one node lies on a straight line between its two neighbours the curvature value is zero, and as the node deviates from this position its curvature value increases. For a node at the end of the snake it is not possible to calculate the continuity in this way, as there is no  $v_{i+1}$  node: for this node the distance between it and the  $v_{i-1}$  node is used instead. For the curvature function both end nodes are unable to use Equation 3.2, in this case the curvature is simply taken to be the difference in the  $y$  values of the node and its neighbour.

### 3.2.3 Formulation of Data Energy Function

The data energy function consists of three separate functions whose results are summed to give the external energy for the node at any position. The image intensity sub-function returns a low value when a node lies over a bright pixel in the original image and returns a high value when the node lies over dark pixel. This has the effect of drawing the snake to brighter parts of the image, a desirable property for our snake when it is observed that flare ribbons appear as the brightest parts of the TRACE images used. The sub-function takes the difference between the pixel value of the node's current position and the maximum pixel value in the image.

The image gradient sub-function aims to draw the snake towards areas of high image gradient. This is achieved by using a separate 'edge image', where pixel values in the edge image are at their greatest where the image gradient is at its maximum, and are zero where the image gradient is zero. The sub-function finds the difference between the current edge pixel and the maximum edge pixel.

The pressure sub-function propels the snake away from its initial position towards the ribbon. Where the snake starts at the top of the image the pressure acts to push the snake down the image, and where the snake starts at the bottom of the image the pressure acts to push the snake up the image. If the snake starts at the top of the image, the pressure function is simply calculated by finding the difference between the  $y$  coordinate of the node's position and the bottom edge of the image. Where the snake is started at the bottom of the edge the difference is between the node's  $y$  coordinate and the top edge of the image.

### 3.2.4 Edge Detection

To create an edge image useful for the image gradient sub-function we must employ an edge detector, the choice of which will impact on the performance of our snake. The first implementation of our algorithm used a Sobel edge detector (Gonzalez &

Woods 2007), applied directly to the pre-processed data. Our first test runs used a test image with no simulated noise, and so the Sobel edge detector worked well. The only edges found in the image lay along the outside of the test ribbon, and the resulting edge image showed these edges clearly with no other edges to distract the snake. The Sobel operator, being a 3 by 3 square filter, has the advantage of being computationally efficient to apply. With the introduction of a test image containing noise it was immediately obvious that the strategy for edge detection required modification, as the snake was easily trapped by noise pixels with large image gradients. The first approach to this problem was to apply a Gaussian blur filter to the image before applying the Sobel filter, which worked well for our initial testing. By substituting this two stage process with a Laplacian of Gaussian (LoG) filter the same result could be achieved with a single pass. The LoG, from Gonzalez & Woods (2007), is defined as:

$$\Delta G(x, y) = \frac{x^2 + y^2 - 2\sigma^2}{\sigma^4} e^{-\frac{x^2 + y^2}{2\sigma^2}}. \quad (3.3)$$

The values of  $x$  and  $y$  are pixel positions relative to the centre pixel of the filter. As the value of  $\sigma$  is increased the LoG response increases in width. For correct implementation of the discrete filter this must be taken into account and the filter size adjusted accordingly. The LoG filter is a second order derivative edge detector that applies Gaussian blur with edge detection, in one filter. As it is a second order derivative edge detector, edges appear in the output images as “zero-crossings”, as described in Section 2.1.2. Finding these zero-crossings is not reliant on thresholding, giving second order edge detection approaches an advantage over first order edge detection approaches.

### 3.2.5 Optimisation: Simulated Annealing

Simulated annealing (SA) is an optimisation technique capable of producing a good approximation to the global optimum of a function given a large search space (Kirkpatrick et al. 1983). It aims to simulate the annealing process in metallurgy, where the heating of a material dislodges its atoms from their bound states (i.e. local minima in the their energy function), and allows them to move about randomly through states of higher energy. Slow cooling then enables the atoms to move into configurations with energies lower than their initial states. Simulated annealing aims to find the minimum energy of a given function from an arbitrary initial configuration. The function can take a large number of different configurations, and the total of all these different configurations is described as the search space. Any one point in the search space is considered as a state of the function, analogous to the physical state of the material used in the metallurgy example. With each

iteration a new configuration of the function representing a neighbouring state is suggested, the decision to move to the suggested state or remain in its current state is decided probabilistically. At each iteration the temperature decreases, replicating the physical process of cooling. The temperature controls the likelihood of suggested higher energy states being accepted, lower temperatures make such changes in state decreasingly likely and vice versa. The function gradually moves into lower energy states, and the process is stopped when the minimisation process achieves a certain target or some computational constraint is reached.

Applied to the energy function of the snake algorithm, SA is used to accept or reject changes in the configuration of the snake, and aims to find a good approximation to the minimum of the snake's energy function. The temperature is initially set high, meaning that the snake is free to move about through the higher energy configurations. As the temperature cools the snake is increasingly confined to lower energy configurations. The temperature is highest close to the initial position of the snake, and there is a defined direction of movement for the snake, therefore SA has the effect of letting the snake pass over local minima in its energy function close to its initial position, and makes the snake increasingly likely to settle on such a minimum as it gets further from its initial position. Local minima in the snake's energy function near its initial position arise due to noise and bright features other than flare ribbons on the solar surface. For example in the 1600 Å TRACE images there is usually a large amount of brightened network, a feature of the solar chromosphere that appears as areas of enhanced emission over the normal background. The network is usually of similar scale and structure to the flare ribbons, and so is not easily removed from the images.

The value chosen for the initial temperature can be set higher or lower such that the cooling occurs closer or further from the snake initial position. Care must be taken when setting this initial temperature, as if set too low it will have little effect, since only configurations that decrease the energy of the snake will be accepted. Thus the snake is likely to come to rest at a local minimum in its energy function far from the flare ribbons. If set too high the snake will be able to move past the flare ribbons, as shown in Figure 3.3, as with a high temperature when a node is on the flare ribbon the node will be permitted to move off the ribbon to a higher energy position. The initial temperature will need to be set according to the size of the snake and the size of the image. This is because the temperature cools at every iteration of the snake, so when the snake is longer and has more nodes, more iterations will be needed for the snake to travel the same distance within the image compared to a snake with fewer nodes. A snake being used on a larger image will need more iterations to move over the same proportion of the image compared to a smaller image.

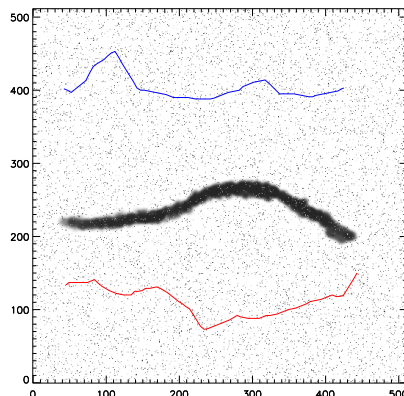


Figure 3.3: Diagram showing snake with the simulated annealing temperature set too high, thus the snake moves past the feature. The snake in blue started at the bottom of the image, and the snake in red started at the top of the image. The image shown is a simulated test image.

### 3.2.6 Correct Truncation of the Snake

As the flare ribbons present in the TRACE images used for this project vary in length and rarely extend along the entire width of the images, it is necessary to determine different starting  $x$  coordinates for each snake in different images. Two different approaches were tested to find a suitable method for determining the starting  $x$  coordinates for the snakes. The first method uses the original image and finds the brightest pixel in the image. This method relies on the brightest pixel belonging to one of the ribbons. From this start pixel we first move across the image to the left in a way similar to region growing. Adjacent pixels are considered as new start pixels if their intensity is above a certain percentage of the initial start pixel's intensity. If there are multiple pixels that fit this condition and lie in the considered direction the pixel with the highest intensity is chosen as the new start pixel. This is repeated until the start pixel reaches the edge of the image or no pixels adjacent to the current start pixel meet the intensity criteria. The  $x$  coordinate of the last start pixel is then used as the left-most position for the snake initialisation. The process is repeated in the opposite direction to determine the right-most position for the snake initialisation. This process, which we refer to as the width determination method, works reasonably well with our simple test case image, but fails where the flare ribbon is discontinuous. An attempt to resolve this issue considered pixels from a wider neighbourhood for selection as a new start pixel. Such approaches were abandoned due to their reliance on the predicted properties of the flare ribbon pixels. The second method used an output from the  $\hat{a}$  trous algorithm. This algorithm uses wavelet transforms to decompose an image, from which it can reconstruct images that represent a certain scale of the original image, (Stenborg & Cobelli 2003).

The wavelet transform is analogous to the Fourier transform, but instead of using sinusoidal base functions the wavelet transforms are based on wavelets (small waves) of varying frequency and limited duration. Using this algorithm produces a specified number of images at different scales, and the sum of all of these images results in the original image. For this task the *à trous* algorithm was used to produce 8 output images, three of which can be seen in Figure 3.4. The output image with the largest scale was used for truncating the snake and is referred to in the rest of this thesis as the “reconstructed scale image”. By choosing the image with the largest scale the enhanced emission of the flare ribbons, and any other bright image feature in the image, are reduced to a vague blob, Figure 3.4 (d). Using this image, the width determination method was employed to find the  $x$  coordinates for the initialisation position of the snake. The use of the reconstructed scale image meant that there was no need to code into the method the ability to consider pixels within an extended neighbourhood of the start pixel. This is because the reconstructed scale image represents the ribbons on a much larger scale, ignoring the finer scale details such as discontinuities in the ribbon structure. This method showed promise for use with TRACE images, and is referred to later in this thesis as the “reconstructed scale image method”.

### 3.3 Factors Affecting Snake Performance

This section looks at the parameters of the snake that can be changed to affect its behaviour. For the successful implementation of the snake these parameters must be fine tuned to suit the images being used. The affect of these parameters on the behaviour of the snake is illustrated with examples.

#### 3.3.1 Changing the Weighting of Energy Sub-Functions

By changing the relative weighting of the data and model energy functions, it is possible to make a significant change to the overall energy function. As a result the properties of the snake and the position where the snake comes to rest will also be changed. Where the weighting of the data energy function is such that it dominates over the model energy function, the associated snake will show little or no rigidity, with its nodes free to move independently of each other. The result will be disordered with many sharp spikes, as demonstrated in Figure 3.5, which shows a snake in the early stages of its progress. Where the weighting of the model energy function is set so that it dominates over the data energy function, the snake remains very rigid and ordered in structure and is unlikely to converge onto any particular feature in the image. In this case SA will allow a certain amount of movement

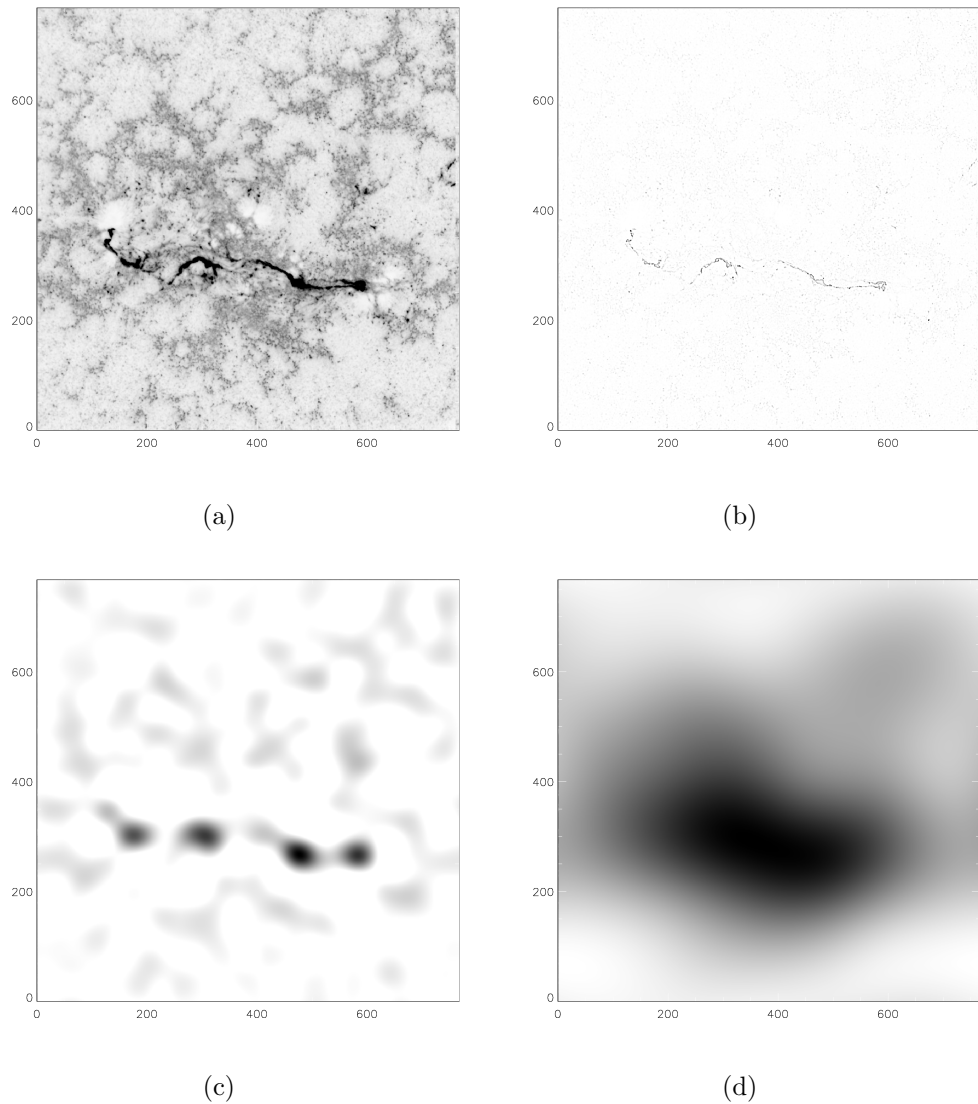


Figure 3.4: Images showing an original image (a), together with reconstructed scale images output from the *à trous* algorithm from the smallest scale (b) through to the largest scale (d).

over the image, but once the SA temperature has sufficiently cooled the snake will quickly settle in an ordered configuration regardless of the underlying image. This behaviour is shown in Figure 3.6

Neither of these scenarios are likely to produce a desirable result, but the advantage of using snakes is that they can find a compromise between prior knowledge about a feature and the image data. To achieve this best compromise the weighting of the two parts of the snake energy function should be roughly equal, so that they both exert some influence over the snake. The exact relative weighting of these two parts of the snake's energy function will need fine tuning to achieve the best result. An example where this weighting is roughly equal is shown with our test image in Figure 3.7, where again the snake is shown before it has settled into its

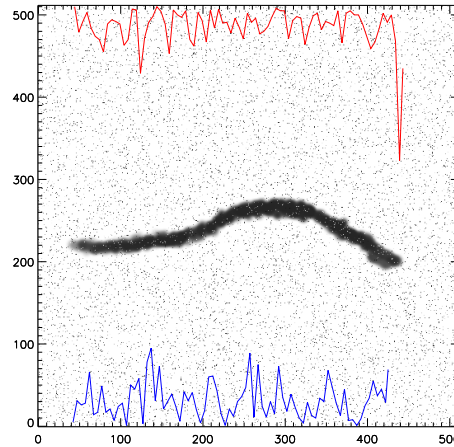


Figure 3.5: Diagram showing snake early in its progress, where the data energy function dominates over the model energy function.

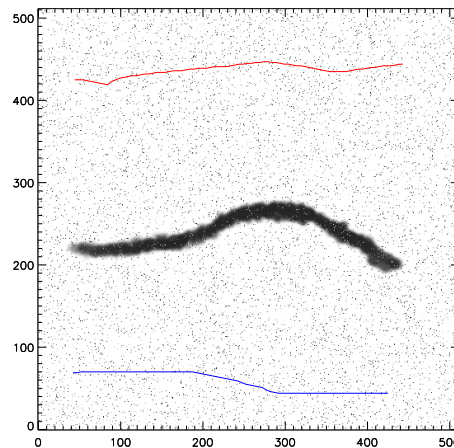


Figure 3.6: Diagram showing snake early in its progress, where the model energy function dominates over the data energy function.

final configuration for the purpose of demonstrating its shape as it moves over the image.

Where the snake is allowed to settle into its final configuration it locates the test ribbon reasonably well. It is possible to see in Figure 3.8 (a) that the rigidity of the snake prevents it from fitting the ribbon edge exactly in the more convoluted parts of the ribbon edge, but in general the snake forms a close fit to ribbon along its length. By fine tuning the weighting of the energy functions it is possible to achieve a better fit to the test ribbon. By slightly decreasing the weighting of the model energy function we can see that it forms a closer fit to the ribbon as in Figure 3.8 (a), however when applying the snake to real flare ribbons the rigidity may be important for keeping the snake in the correct place where the ribbon edge becomes

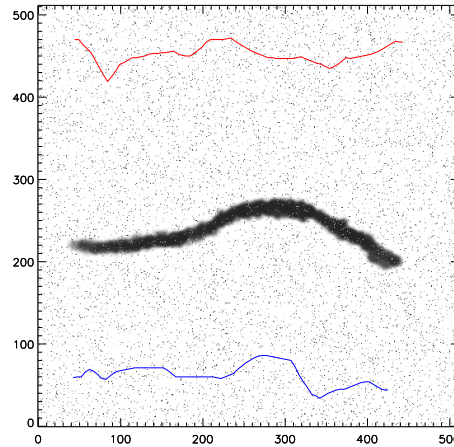


Figure 3.7: Diagram showing snake early in its progress, with the data and model energy functions weighted equally, the result is a snake which is attracted to the strong edges in the image but maintains a certain amount of rigidity.

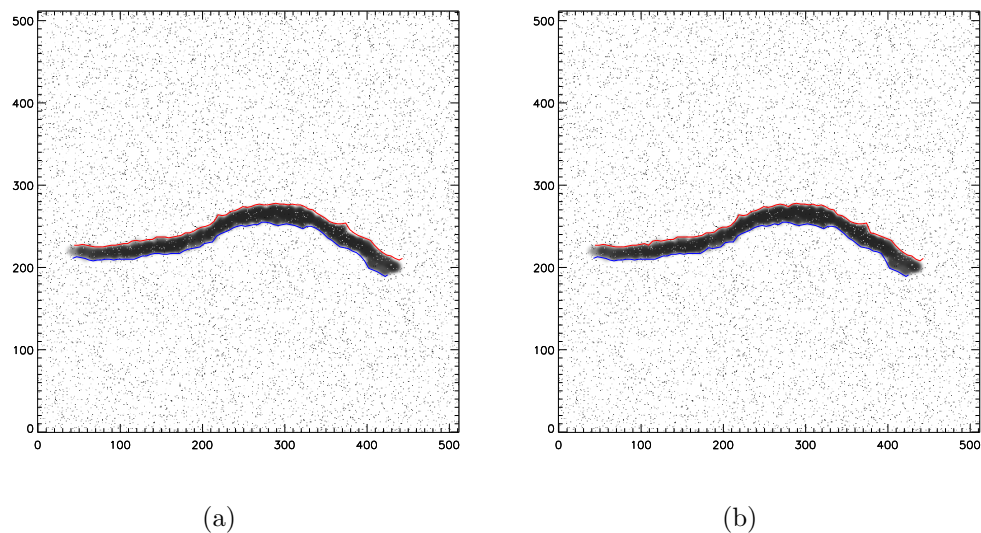


Figure 3.8: Diagram showing snake in its final configuration, where it fits the test ribbon well. Image (a) shows a snake which is slightly more rigid than the snake in image (b), this rigidity prevents the snake from obtaining as close a fit as the snake in image (b).

faint and tenuous. It is also possible to reduce the rigidity too much.

### 3.3.2 Effect of Noise

By adding noise to the test image we attempt to replicate real flare data more accurately. After adding noise to the test images it was immediately apparent that the snake was highly sensitive to noise. The snake was liable to become stranded on points of stronger noise and was so prevented from reaching the ribbon if such pixels

lay between its initial position and the ribbon. This was to be expected, as it is noted that edge detectors are sensitive to noise, and the snake relied principally on the edge image. To reduce the snake's sensitivity to noise we aimed to remove noise by blurring the images. In the initial stages of development we employed a separate Gaussian blur filter applied to the image before applying Sobel operator for edge detection. This approach worked reasonably well, although there is an upper limit on the amount of noise this can deal with. The edge detection changed to using a Laplacian of Gaussian filter, which added edge detection benefits over the Sobel operator and removed the need for a separate Gaussian filter. In cases where noise levels are sufficiently high it becomes impossible to remove the noise by blurring the image without removing important levels of detail from the flare ribbons. In these cases the optimisation technique, SA, provides a means of enabling the snake to move over smaller minima in its energy function represented by noise or other image features.

### 3.3.3 Laplacian of Gaussian

The  $\sigma$  parameter used by the LoG edge filter is used to determine the amount of Gaussian blur applied to the image. Increasing the value of  $\sigma$  increases the amount of blur, and vice versa. Higher values of  $\sigma$  will result in smoother edges in the edge image, and in turn this usually results in a smoother snake. If too high a value is used for  $\sigma$ , the edges become so blurred that they lose important detail and eventually no detail remains. Lower values for  $\sigma$  will result in rougher edges in the edge image, but retain more of the finer detail lost with the use of higher  $\sigma$  values. If  $\sigma$  is set too low it is also more likely that edges due to noise or the brightened network will contribute to the edge image. This effect is illustrated in Figure 3.9, where Figure 3.9(a) shows the result where the value of  $\sigma$  is set too low to suppress the noise in the image, and hence the snake gets snagged on the noise. Figure 3.9(b) and Figure 3.9(c) show the result where the value of  $\sigma$  is sufficient to suppress the noise, and the snake locates the ribbon. In Figure 3.9(c) the value for  $\sigma$  is set higher and so the snake result is slightly smoother. Figure 3.9(d) shows where the values of  $\sigma$  is set too high, and as result edge pixels are only present in small clusters along the ribbon edges, so that the snake falls through the gaps between these clusters.

As our zero crossing detection uses the magnitudes of the pixels to either side of the zero crossings, stronger edges are represented in the edge image as pixels with a greater value. This aids the snake's ability to move over the weaker edges (e.g. as presented by chromospheric network in real flare images) and come to rest of the stronger edges (ribbons). This does mean that when higher values of  $\sigma$  are used the edges are generally weaker, and as such it may be necessary to decrease the

directional pressure on the snake to prevent it from being pushed past the edges of the flare ribbons.

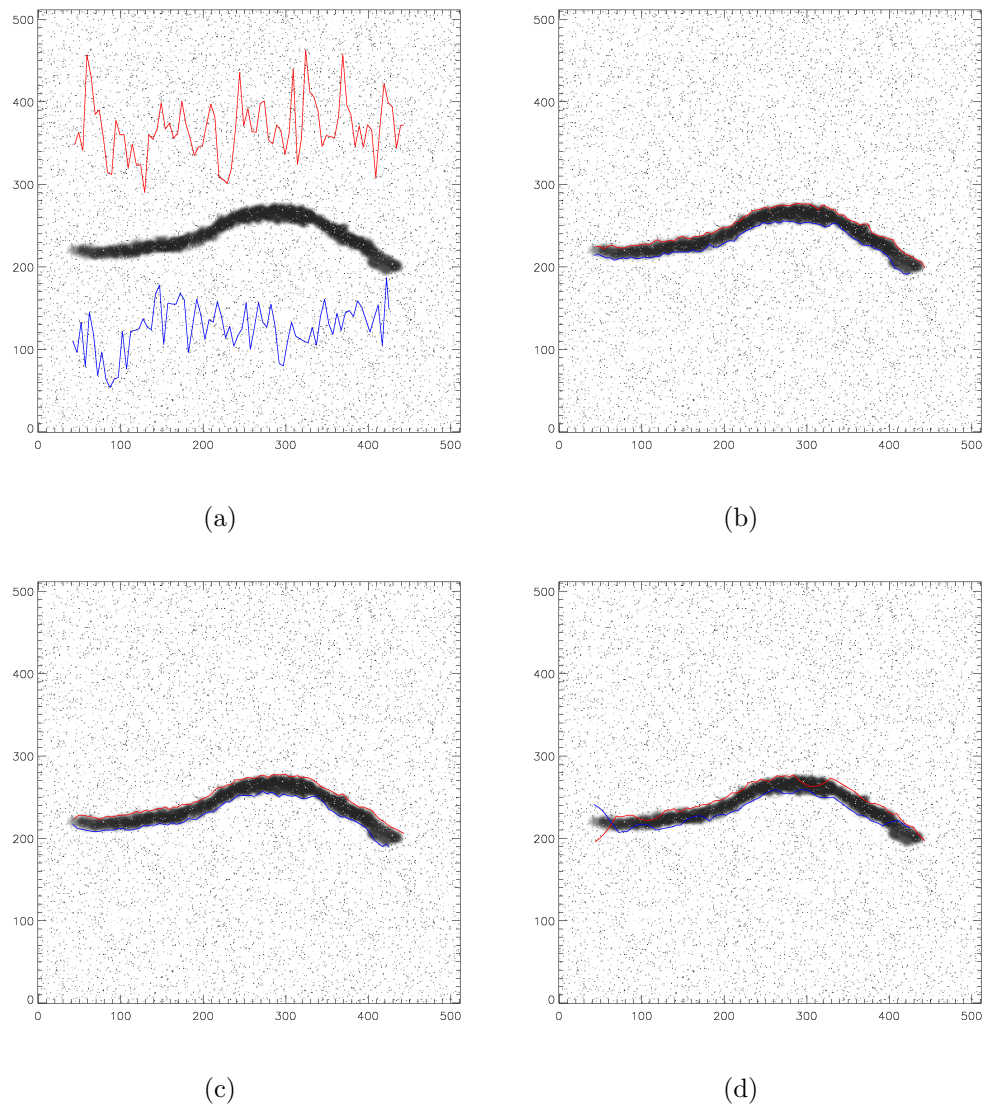


Figure 3.9: Images showing snake results using different values for  $\sigma$  in the LoG, and how this parameter can influence the end result of our algorithm. Images, shown using  $\sigma = 1.0, 2.5, 5,$  and  $6.5$ .

### 3.3.4 Pressure

In order to combat the initialisation problem common to snakes (as discussed in section 2.1.3), we introduce a directional pressure to our snake, described as “pressure forces” in section 3.2.3. Built into our algorithm is the ability to apply separate weighting to the individual functions that combine to give the data function. This enables us to increase or decrease the “pressure” on the snake. If this pressure is too weak the snake will never reach the ribbon, instead the snake will find a position

in which any change has a sufficiently large increase to the model energy function that the reduction in the data energy can not overcome it. If the pressure is too strong, it will dominate over the other terms in the data energy function when the snake is over the ribbon, thus the snake moves over the ribbon without stopping and comes to rest at the bottom of the image. It is therefore necessary to balance the weighting of the pressure with the other parts of the data energy function, and with the model energy function.

## 3.4 Summary

This chapter has documented the initial stages of development for the snake algorithm, and illustrated the influence of specific parameters of the algorithm and its end result. We have detailed the overall design of the algorithm, and the formulation of its associated energy function. The reader should now have an idea of how the algorithm works, and how we are able to adapt the snake to detect ribbons in different images. This understanding is essential for reading of the next chapter where we detail the application of the snake algorithm to real flare data and present a qualitative and quantitative evaluation of its performance. We also discuss the fine tuning of the algorithm to the images used, and the characteristics of certain flare ribbons that influence the ease with which we can locate them accurately with the algorithm.

# Chapter 4

## The Snake Algorithm with Real Flare data

Having tested the snake algorithm using a simulated flare image, we next tested the algorithm using real flare data from the TRACE satellite. A number of flares were chosen for their strong and well-defined ribbons to be used in this process. TRACE images in the 1600Å and 195Å passbands were chosen, although more 1600 Å images were used, simply because there were more images showing flare ribbons in this waveband. Many of 195 Å flare images inspected for possible use did not show flare ribbons, or the ribbons were obscured by flare loops. Each flare examined was present in a sequence of images, enabling the ribbon positions to be followed over time.

### 4.1 Modifications

After applying our algorithm to a small number of flares it became apparent that we could improve it with a few modifications. We describe the reasoning behind these changes, and how they were made.

#### 4.1.1 Splitting into a Two-stage Process

One of the modifications to our algorithm was to split the ribbon tracking process into two parts. The first part attempts to locate the flare ribbons in the last image of the sequence. For this the snakes are started at the top and bottom of the image, and the output ribbon positions are recorded in a text file and made available for the next part of the algorithm. The second part of the algorithm aims to track the flare ribbons as they evolve in the remaining images in the sequence. The flare ribbon positions identified in the first part of the algorithm are used as the starting positions for the snakes in the penultimate image. The snake algorithm is run on

each image in turn, with the images processed in reverse order, starting with the penultimate image and ending with the first image. The tracked ribbon positions from each image are used as the starting positions of the snakes for the next image to be processed (i.e. the image captured before the one just processed). The generally observed behaviour is that flare ribbons move apart over time, hence it is reasonable to assume that the ribbons from an image captured earlier in time will lie inside the ribbons from an image captured later in time. Using the tracked ribbon positions as a predictor for the ribbon positions in the next image utilises the prior knowledge available to improve the tracking ability of the algorithm. Using this prior knowledge also has the advantage of saving processing time as the snakes have less distance to travel before finding the ribbons. It also significantly improves the chance of the snake finding the ribbon position, as the search space for the energy minimisation is significantly reduced, and the snakes start close to the desired minimum energy configuration. Provided the ribbons have not moved very far between images, it also side-steps the initialisation problem associated with snakes as discussed in Chapter 2. If the ribbon positions between two images are significantly different some of this benefit is lost, but provided the pressure sub-function is appropriately weighted the snake retains the ability to move across the image to locate the ribbons.

### 4.1.2 Truncating the Snake

After use on only a couple of flares it became obvious that the “reconstructed scale image method” for truncating the snake to the appropriate length and determining the  $x$  coordinates for the ends of the snakes was flawed. In many flares the two flare ribbons are not of equal length (see Figure 4.1). Our approach to snake truncation made no allowance for this. Also, as the reconstructed scale image is a representation of the whole image, i.e. the flare ribbons and the network, an area of brightened network can have more influence on the reconstructed scale image than flare ribbons that appear faint or cover only a small area. This can lead to a reconstructed scale image that does not represent the horizontal extent of the flare, and the incorrect truncation of the snake. This is demonstrated in Figure 4.2, where the reconstructed scale image (a), shows the bright area of the image slightly left of centre, and the flare ribbons are shown slightly right of centre in green. Control for snake length is therefore given to the user, who is now prompted to specify the  $x$  coordinates for the start and end of both the flare ribbons independently of each other. This information is then used by the snake algorithm to define outer limits for the starting  $x$  coordinates for both snakes in all images. The LoG edge image is then compared against these outer limits for both the top and bottom ribbon. The final starting  $x$  coordinates for the snakes are defined by the outermost columns in the edge

image with a pixel value greater than 0 that are inside the limits set by the user. This process allows for two snakes of different length, and also allows for snakes to grow with the flare ribbons as they evolve. Using this method prevents the algorithm from being fully autonomous, but presents an acceptable balance between user intervention and the time and computational demands of implementing a fully autonomous alternative.

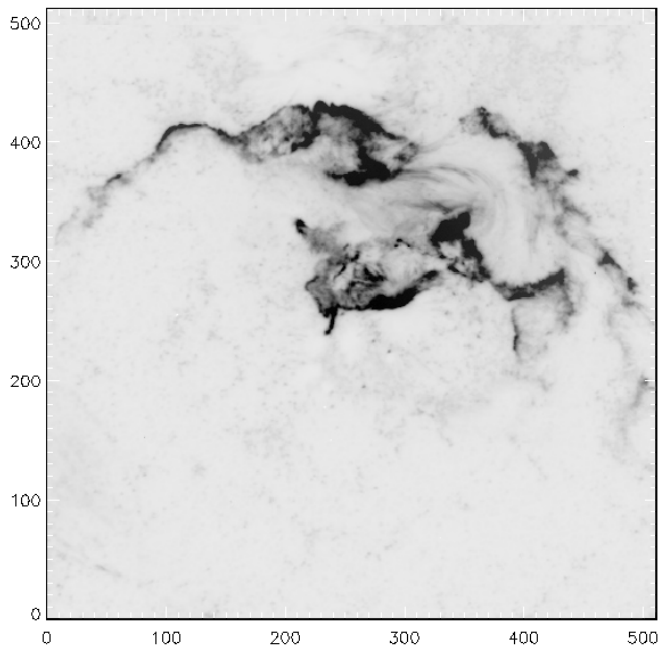
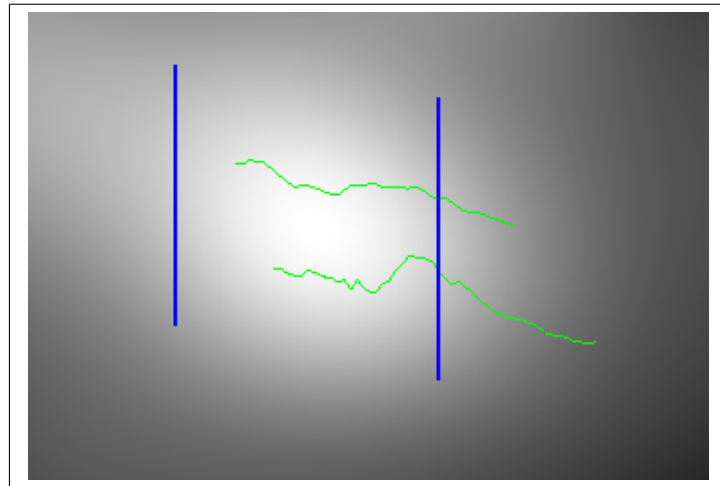


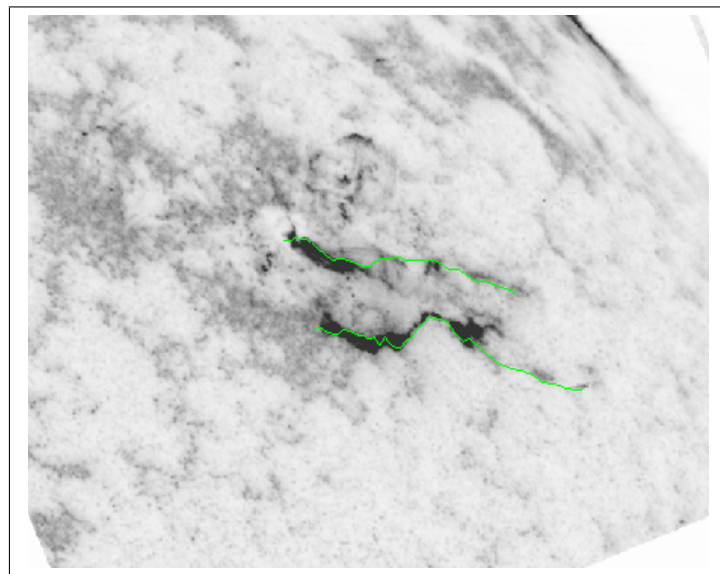
Figure 4.1: An image from a flare on 12 November 2000 in the TRACE 1600 Å band. The ribbon morphology of this flare is interesting and complex, but regardless of the interpretation of the ribbons, the difference in length between the upper and lower ribbons is apparent.

## 4.2 Finding the Error in the Snake Tracking Result

To gauge the success of the snake algorithm in tracking the flare ribbons over different images and different flares, we compare its results with the only ground truth available; the result of manually tracked flare ribbons. The measure of “tracking error” for the snake results is the area enclosed between the snake result and the manual result divided by the length of the flare ribbon (both quantities are in pixel units). This chosen measure of the tracking error is therefore the mean offset in pixels between the snake position and the “ground truth” position. The ribbon’s length is defined as the length along the path of the manually traced ribbon, as this prevents a bias towards ribbons that may be straighter or orientated differently. In order to give some sense of scale to this “tracking error” measure, it is compared



(a)



(b)

Figure 4.2: Images showing the reconstructed scale image (a), from a flare on 25 June 2000, and the original image (b). In both images the tracked ribbons (whose horizontal range has been determined by hand), are shown in green. Image (a) shows blue lines representing the horizontal limits of the flare ribbons as defined by the “reconstructed scale image method” for snake truncation, which clearly do not agree with manually obtained horizontal limits. Note that although the far right extent of the ribbons are very faint and difficult to see, they do extend along the length of the green lines.

against an error obtained using the same measure between a number of manually obtained ribbon positions (referred to from now on as the “ground truth” positions). These ground truth positions were taken from two ribbons, each from two different flares. The two ribbons were chosen to represent the two extremes of a simple smooth flare ribbon and a complex ribbon with a large amount of smaller structure and were the upper ribbon of the 20th January 2001 flare, in image number 51 from the image sequence, and from the upper ribbon of the 10th April 2001 flare, in image

number 2 from the image sequence. Ten different “ground truth” positions obtained for each of the two ribbons were compared to each other to give an average error of 0.7 pixels (px). This is used as a guide to the accuracy obtainable by manual tracking of the flare ribbons and is used as the benchmark for the results from the snake algorithm.

### 4.3 Finding Ribbons in the Last Image of the Sequence

We begin by showing the snake performance on the last image in the sequence of our chosen flares. The snakes that start at the top of the image and move downward are shown in the images in green and the snakes that start at the bottom of the image and move upward are shown in the images in pink. We start with the flare showing the simplest ribbons and use this as an example to demonstrate the application of the snake algorithm and the fine tuning of the algorithm’s parameters. The various parameters are described in Section 3.2; the main points are repeated. The  $\sigma$  parameter is used for the LoG edge filter to determine the amount of blur applied to the image when producing the edge image, a higher value  $\sigma$  will produce a smoother edge image less sensitive to fine structure in the original image. The “cont” and “curv” parameters set the weighting of the continuity and curvature sub-functions that make the model energy function, (see Section 3.2.2). The “pressure”, “grad” and “int” parameters set the weighting of the pressure, image gradient and image intensity sub-functions of the data energy function (see Section 3.2.3). These parameters that set the weights of the energy sub-functions are listed as weights relative to each other. To aid comparisons the continuity weight is shown as 1 for each flare, the other weights are shown relative to this. The final parameters used for each flare are summarised in Section 4.3.7.

#### 4.3.1 Flare 20th January 2001, 20:46 - 21:16, M7.7, 1600 Å

The last image in the time sequence for the flare on 20th January 2000 is shown in Figure 4.3. From a quick observation of the flare it is possible to note some of its properties, which can provide some simple information useful for the application of the snake algorithm. For the fine tuning of the snake algorithm to a particular image or set of images we make small adjustments to a default set of parameters. The default parameters have been obtained empirically. The ribbons of this flare are significantly closer to the top of the image than the bottom, meaning that the lower snake will have to travel over more of the image than the upper snake, to find the ribbon. This suggests that the SA initial temperature should be increased

from the default for the lower snake, and decreased for the upper snake. The lower ribbon and some parts of the upper ribbon appear quite thin and faint. A careful balance must be struck when choosing the  $\sigma$  value for the LoG filter, as if this value is too high the thin faint parts of the ribbon will be blurred into the background, while if set too low the smaller bright noise features and the underlying network are more likely to trap the snake as it moves over the image. Parts of the ribbons also appear in low contrast to their surroundings, especially when the surrounding area is enhanced network. This again has implications for the edge detection, as in certain areas the image gradient between the network and the background appears at least equal to the image gradient between the flare ribbons and the network. This can result in the snake becoming caught on the network and not the flare ribbon. In Figure 4.3, it is possible to see that the lower ribbon has split into two parallel ribbons, this becomes more obvious in earlier images, and has been observed in other flares and reported as ribbon bifurcation (Fletcher & Hudson 2001). This presents a complication for ribbon tracking in general, as it is not clear which part of the ribbon to track. This feature will be discussed in more detail when we review the performance of our algorithm on the remaining images in the sequence for this flare in Section 4.4.1. Both the upper and lower ribbons appear reasonably straight and smooth.

For the first run with this image we increased the default SA initial temperature for the lower ribbon, and decreased this value for the upper ribbon. We left the LoG  $\sigma$  at its default value of 3.5, but after examining the edge image output from this first run we were in a better position to make changes to this parameter. The remaining parameters were also left unaltered from their defaults. The result from this first attempt can be seen in Figure 4.3.1, where the final snake positions are shown overlaid on the original image (a), and on the edge image (b).

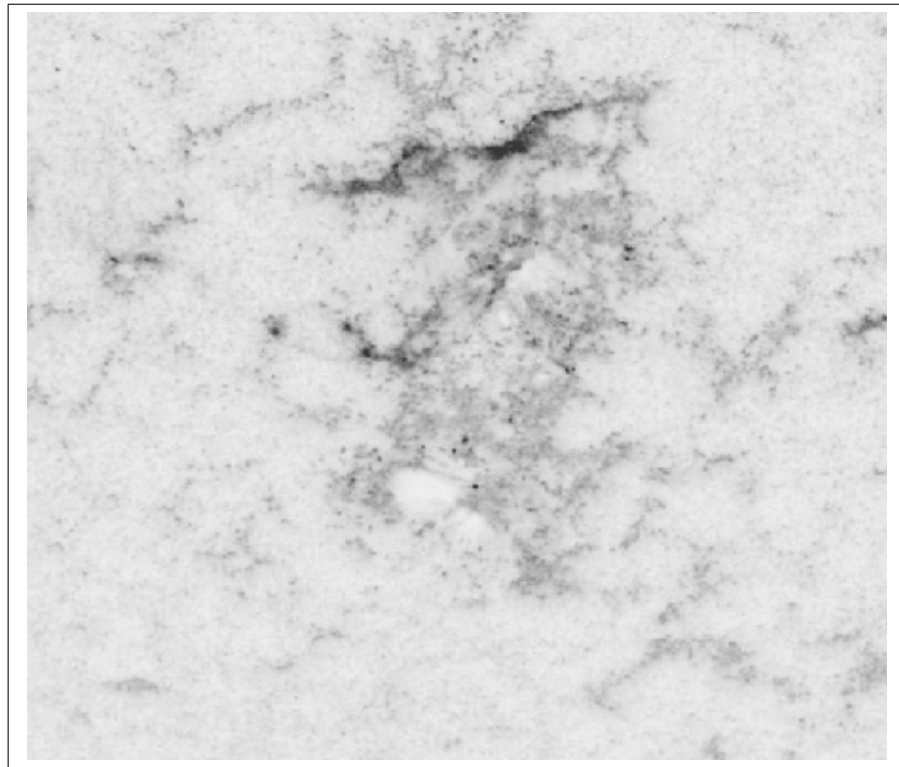
From the results of this first run it is clear that some modifications to the parameters need to be made. After each run of the snake algorithm, it is advisable to view the edge image, as this has the greatest effect on the performance of the snakes. By observing the edge image produced by this first run, see Figure 4.3.1, it is clear that the upper ribbon appears well-defined, but that there are a few edges that appear as a result of the network, and not the flare ribbon, that have trapped the snake before it has reached the upper ribbon. It is also clear that the lower ribbon is represented in the edge image, although it does not appear so well defined as the upper ribbon. There are also many edges that appear between the lower ribbon and the bottom of the image. These edges will present local minima in the lower snake's energy function, and have the potential to trap the lower snake before it reaches the lower ribbon. To remove some of these edges we increased the value of  $\sigma$  for the LoG filter from 3.0 to 4.0. We could also have increased the SA initial temperature

for the lower snake, but as the other edges appear close to the lower ribbon, it may not have been possible to make the snake pass over all the other edges without also passing over the lower ribbon. With the parameters changed the snake algorithm was reapplied, and the results are shown in Figure 4.5.

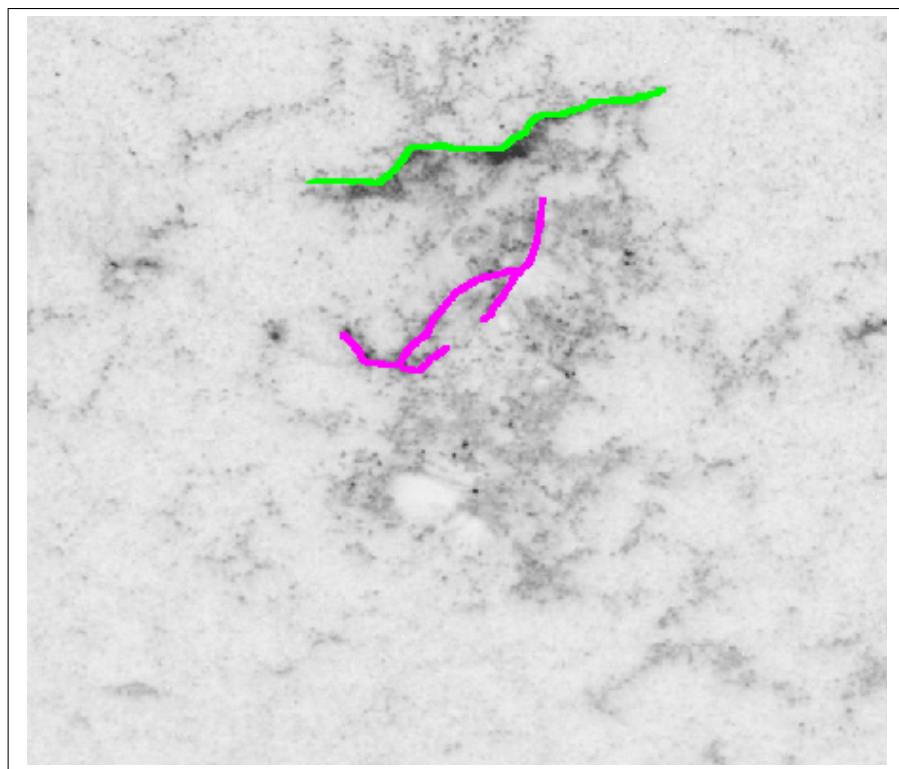
By examining the edge image from this second run (see Figure 4.5) it is possible to observe a decrease in the edges present as a result of the network, although there remains a large number of edges not from the flare ribbons. As the ribbon detail itself appears vague in places, increasing the LoG  $\sigma$  value again would likely result in some of the ribbon detail being lost. The new final position of the upper snake is much improved, it matches the ribbon over a small region, and in general it is close to the ribbon and resembles its general shape. It has however moved slightly past the ribbon in one place to the far right of the ribbon. As this part of the ribbon shows up in the edge image, this is probably due to the affect of SA. Hence the SA initial temperature for the upper snake was reduced. The upper snake is also held off the upper ribbon for the majority of its length. By examining the original image and the edge image it appears as though there are a few small bright points that are holding the snake away from the ribbon. The snake appears very smooth in these regions, suggesting that the small bright features are holding a few nodes of the snake, and the rest of the snake is being held up between these nodes by the model energy function. If the weighting of the model energy function were decreased such that some nodes of the snake could reach the ribbon, the nodes that reach the ribbon would then have the effect of pulling the rest of the snake down so they too would come to rest on the ribbon. The lower snake appears slightly different in shape, but has not travelled significantly closer to the lower ribbon. By examining the edge image, see Figure 4.5, it is clear that the lower snake is being trapped by a number of weaker edges. By increasing the pressure sub-function weighting it may be possible to push the snake over these weaker edges and onto the stronger edges of the lower ribbon. Of course if this is set too high it would simply push the snake over the lower ribbon. The parameters were adjusted as discussed, and the algorithm was run again on the last image: the result from this run is shown in Figure 4.6.

From Figure 4.6, the snakes can be seen to fit the ribbons well, with the upper snake showing the better fit, and the lower snake coming to rest on the upper edge of the lower ribbon rather than the lower leading edge. By looking at the edge image it is clear to see why the lower snake has produced this result, as the lower edge of the lower ribbon appears very faint and discontinuous, whereas the upper edge appears much stronger and more solid, so that this would represent a node position of lower energy than the fainter edge. This underlines an important point, that the edge image is vital to the performance of the snake. Where a ribbon appears strong in

the edge image and other sources of edges appear weak, a large number of different parameters for the snake are likely to produce a good result. Where the ribbon appears faint and indistinct in the edge image and edges from other sources appear at a similar strength the task of finding suitable parameters becomes increasingly difficult with many fewer combinations likely to give a satisfactory result. The bifurcation observed in the lower ribbon has not had an effect on the results for this image. The final snake results give errors of 0.7 px for the upper snake, and 3 px for the lower snake. The error for the upper snake shows an equivalent fit to the benchmark manual error of 0.7 px. The error for the lower snake is significantly worse, mainly due to the large section of the snake that has come to rest on the upper edge of the ribbon rather than the leading lower edge. That the error for the upper snake is significantly lower than for the lower snake is to be expected given the relative strengths of the ribbons in the edge image.

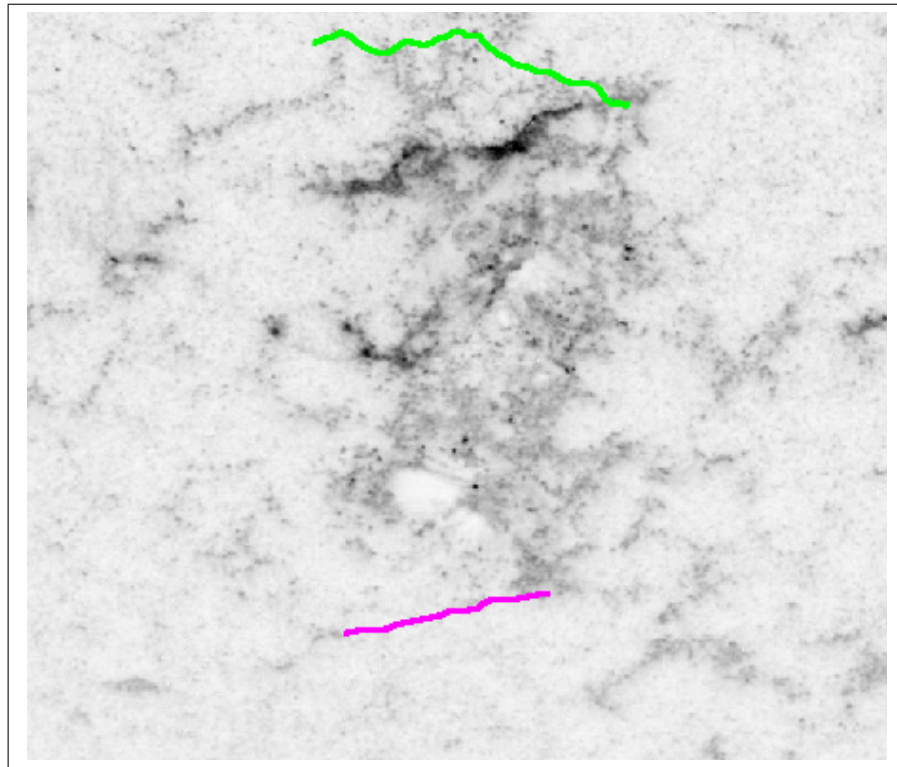


(a)

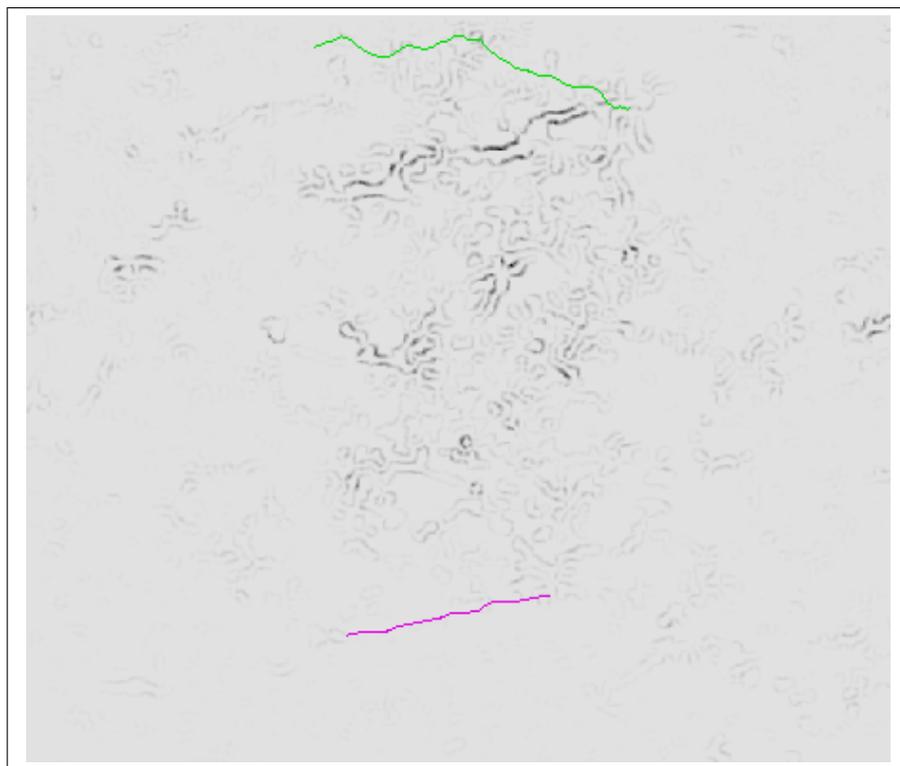


(b)

Figure 4.3: Image (a) is from a flare on 20 January 2001 in the TRACE 1600 Å band. This is the last image in the sequence for this flare, there are two ribbons present, a brighter upper ribbon, and a lower fainter discontinuous ribbon. The same image is shown in (b), but with the ribbon positions manually traced in green and pink, for the upper and lower ribbons respectively. The lower ribbon is split into two parallel ribbons in its centre.

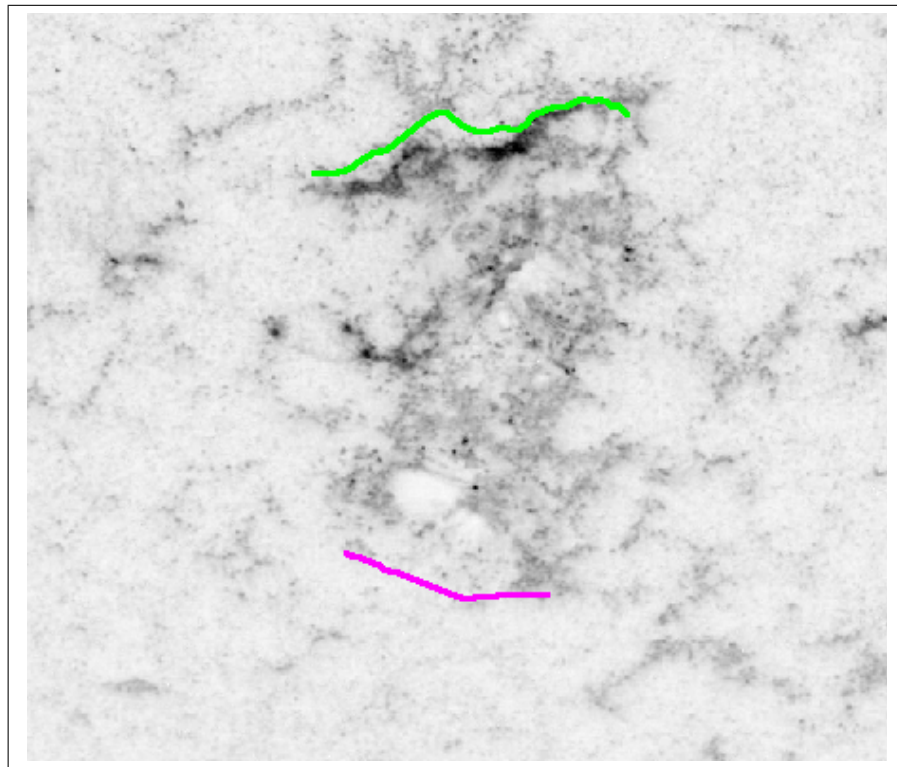


(a)

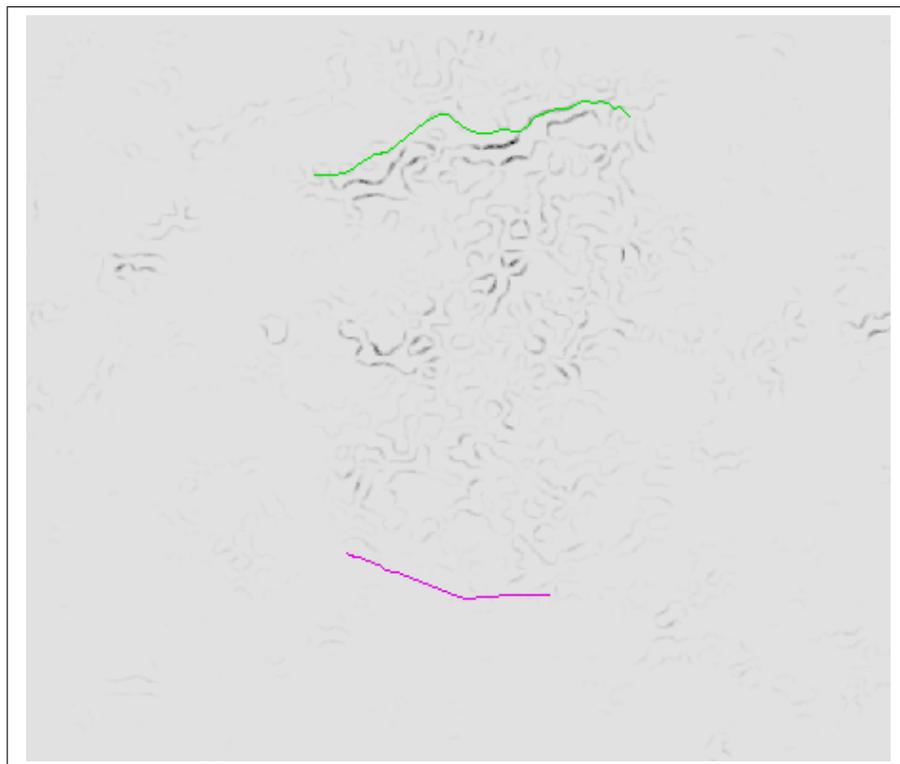


(b)

Figure 4.4: First run of the snake algorithm on the last image in the time sequence from the 20th January 2000 flare. This shows the snake results in green for the upper snake, and in pink for the lower snake. The parameters used for these results are: upper snake - cont = 1.0, curv = 1.0, pressure = 4.15, grad = 0.625, ints = 0.0, te = 0.6500; lower snake - cont = 1.0, curv = 1.0, pressure = 3.75, grad = 0.625, ints = 0.0, te = 0.9980. For both snakes  $\sigma = 3.0$ .

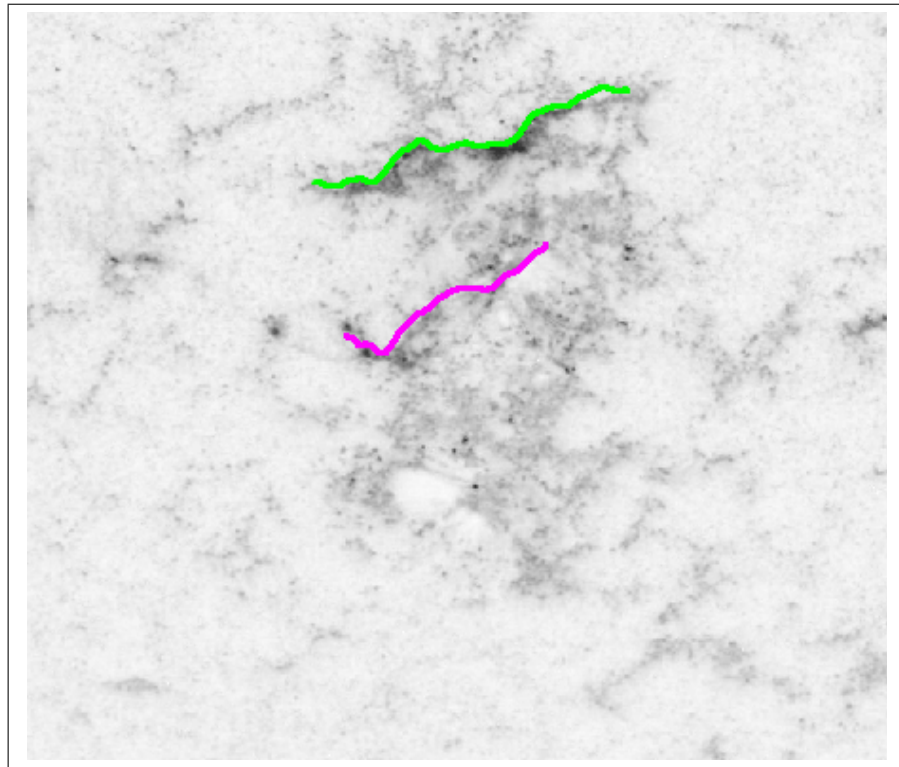


(a)

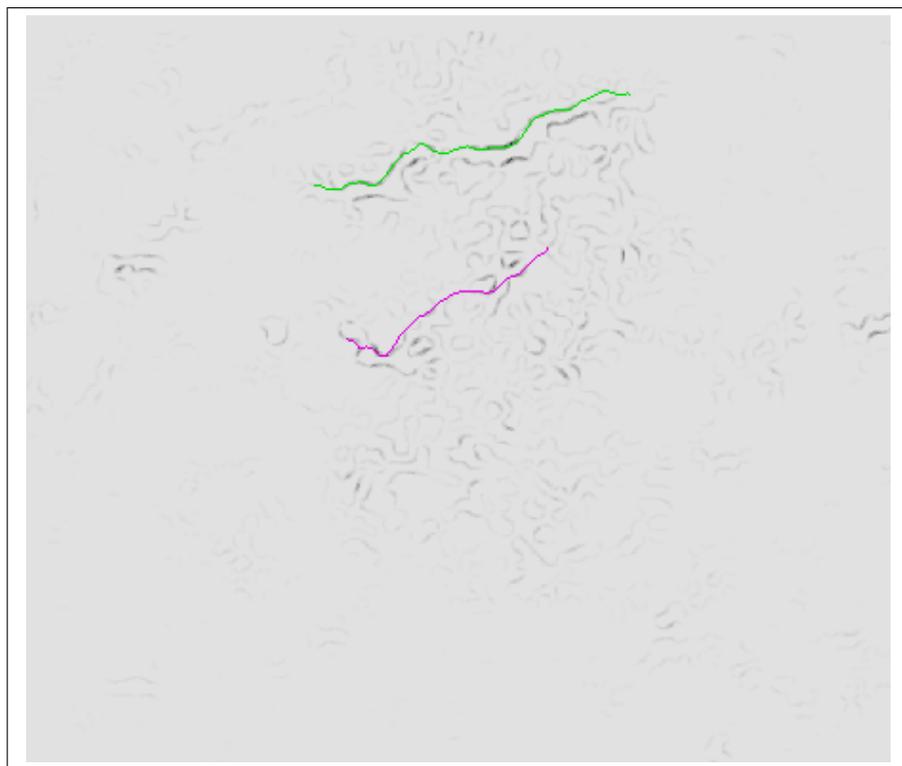


(b)

Figure 4.5: Second run with last image from the flare on 20th January 2001. Both snakes still do not fit the ribbons well. The parameters used for these results are: upper snake - cont = 1.0, curv = 1.0, pressure = 4.15, grad = 0.625, ints = 0.0, te = 0.6500; lower snake - cont = 1.0, curv = 1.0, pressure = 3.75, grad = 0.625, ints = 0.0, te = 0.9980. For both snakes  $\sigma = 4.0$ .



(a)



(b)

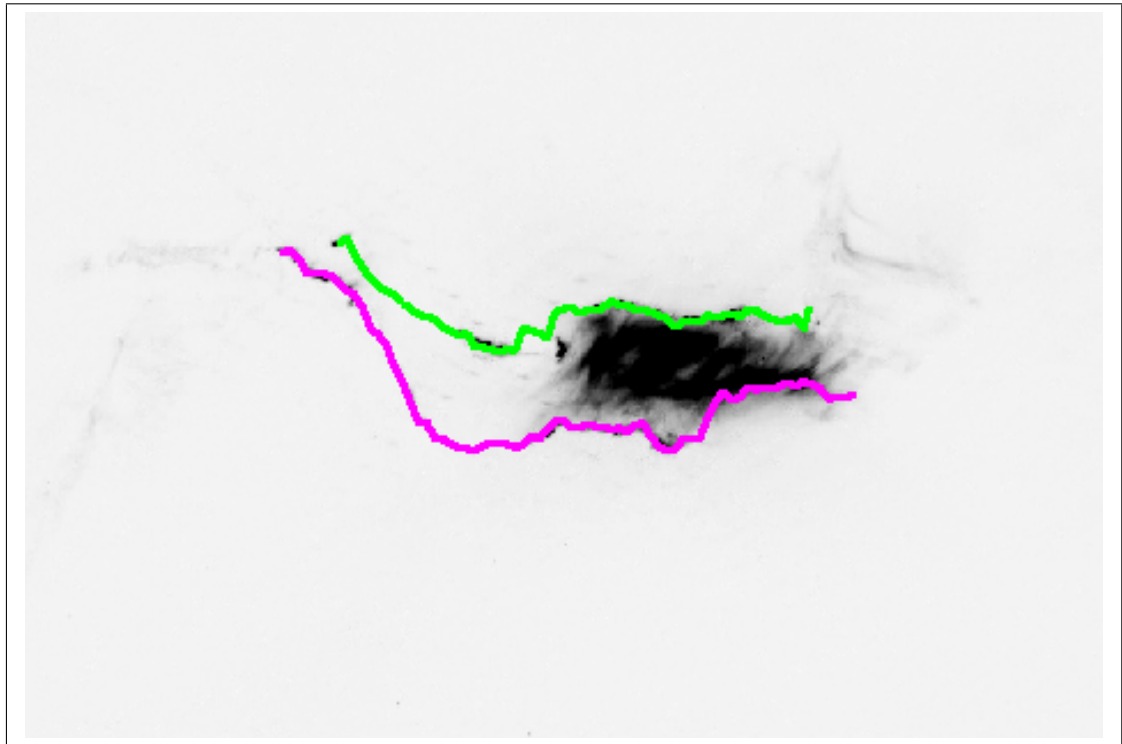
Figure 4.6: Third run with last image from 20 Jan 2001. Both snakes now fit their respective ribbons reasonably well. The lower ribbon has come to rest on the upper edge of the lower ribbon rather than the lower edge. The parameters used for these results are: upper snake - cont = 1.0, curv = 1.0, pressure = 5.54, grad = 0.834, ints = 0.0, te = 0.5600; lower snake - cont = 1.0, curv = 1.0, pressure = 5.31, grad = 0.625, ints = 0.0, te = 0.9980. For both snakes  $\sigma = 4.0$ .

### 4.3.2 Flare 14 July 2000, 09:43 - 11:02, X5.7, 195 Å

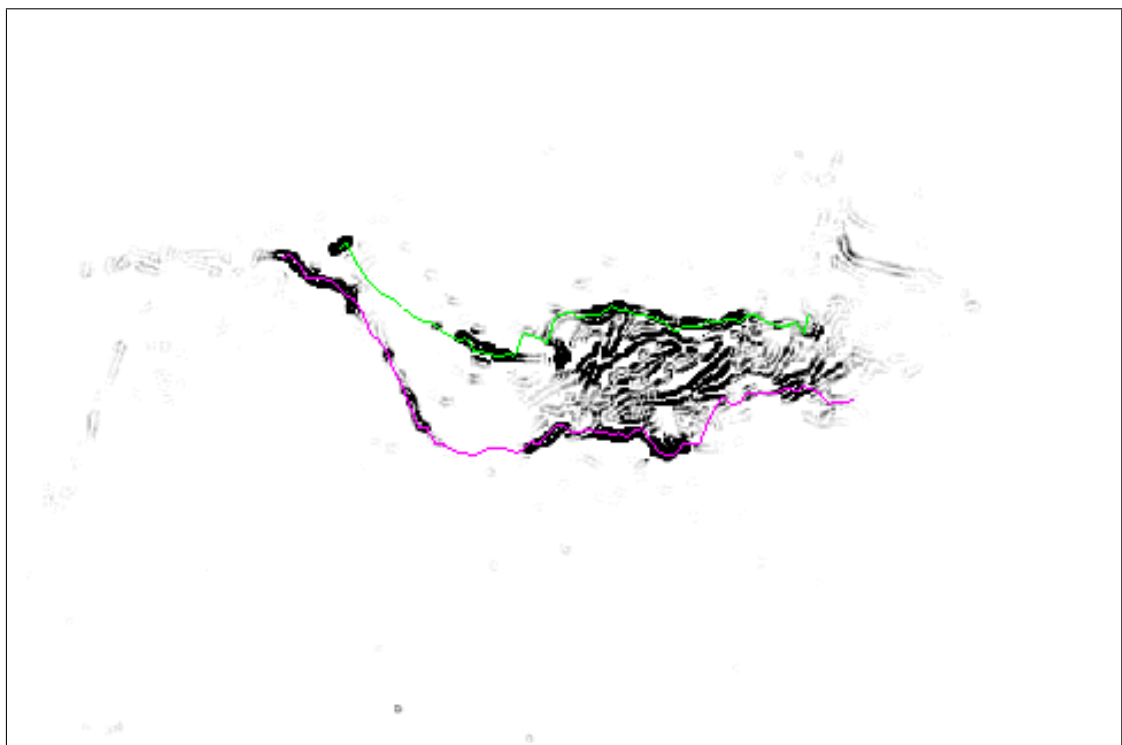
The images used for this flare were captured in the TRACE 195 Å band, and therefore present significant differences with images from the 1600 Å passband used for other flares. The most notable of these differences are emission from the flare loops, and the lack of emission from the network. The presence of bright loops presents a feature that can interfere with the snakes, whilst the absence of emission from the network eliminates another. Unlike the network, the loops do not lie between the snake's initialisation position and the flare ribbons, suggesting the snakes will have an easier task of reaching the ribbons. In places along the flare there are regions where there are no ribbons visible, where it is questionable whether there is a meaningful result to be obtained. There are also regions where the ribbon emission is weak with neighbouring stronger loop emission which may present a problem for the algorithm. Figure 4.7 shows the last image in the sequence for the 14th July 2000 flare, with the snake results overlaid. In these images the length of the snakes was set to include the left-most section of the flare ribbons, which whilst from the same event, represents earlier flare activity. This section of the flare ribbons is not of primary interest in this image, but has been included to provide an additional test for the snake algorithm.

The result shows a good fit to the flare ribbons (see Figure 4.7) with the exception of the regions to the right of the flare where there is no visible lower ribbon emission. In these regions the best result the snake could return would be the boundary of the loop emission, but this boundary is particularly weak and blends into the background very smoothly and therefore does not produce an edge in the edge image. As a result the snakes are drawn to the edge of the brighter loop emission instead of the boundary, and this error with respect to the manually traced ribbon positions (that do locate the vague smooth boundary of the loop emission), produces a significant contribution to the overall snake tracking error. It is interesting that despite the faint appearance of the ribbons to the left, the snakes still fit this section of the ribbons well. Other than the lower right section where there is an absence of ribbon emission the snakes show a good fit to the ribbons. The errors for the snake tracking for this flare image are 0.6 px for the upper ribbon and 3.9 px for the lower ribbon. This reflects the qualitative observations of the snake performance.

Figure 4.8 shows the snake result where the length of the snakes have been restricted so that the left most section of ribbon emission is ignored. Although this left most section of ribbon emission appears reasonably strong here, it is from earlier activity in this flare, and does not appear as strong in the other images of the sequence.

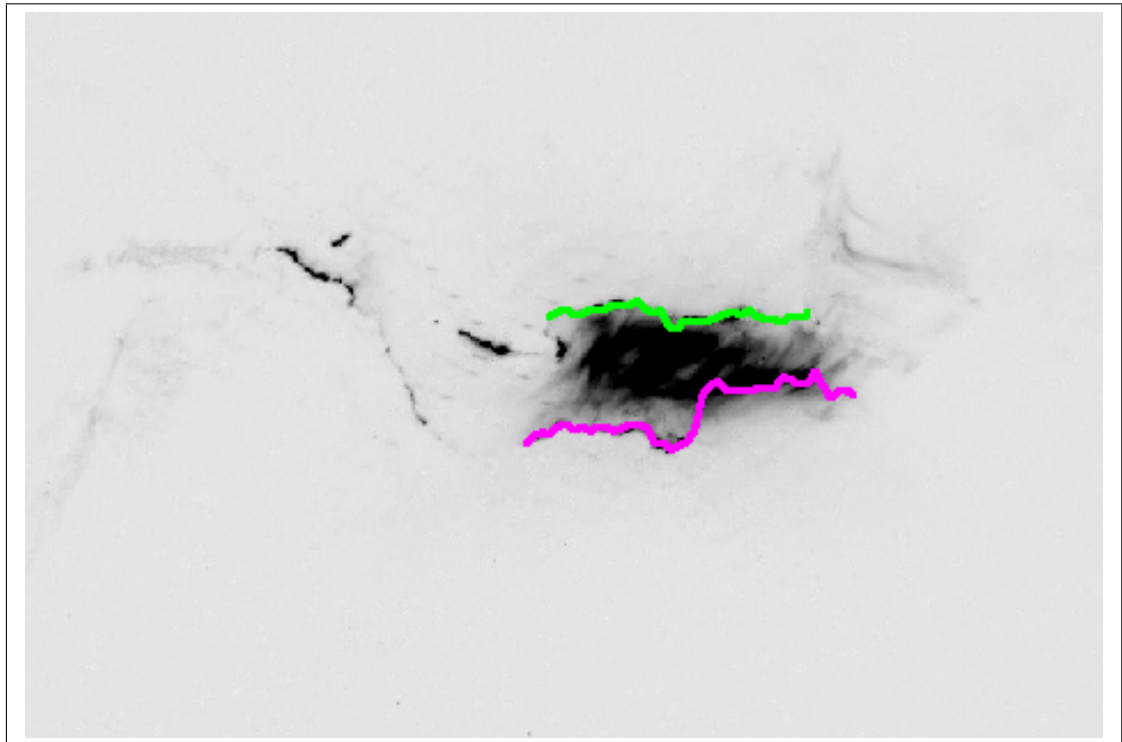


(a)

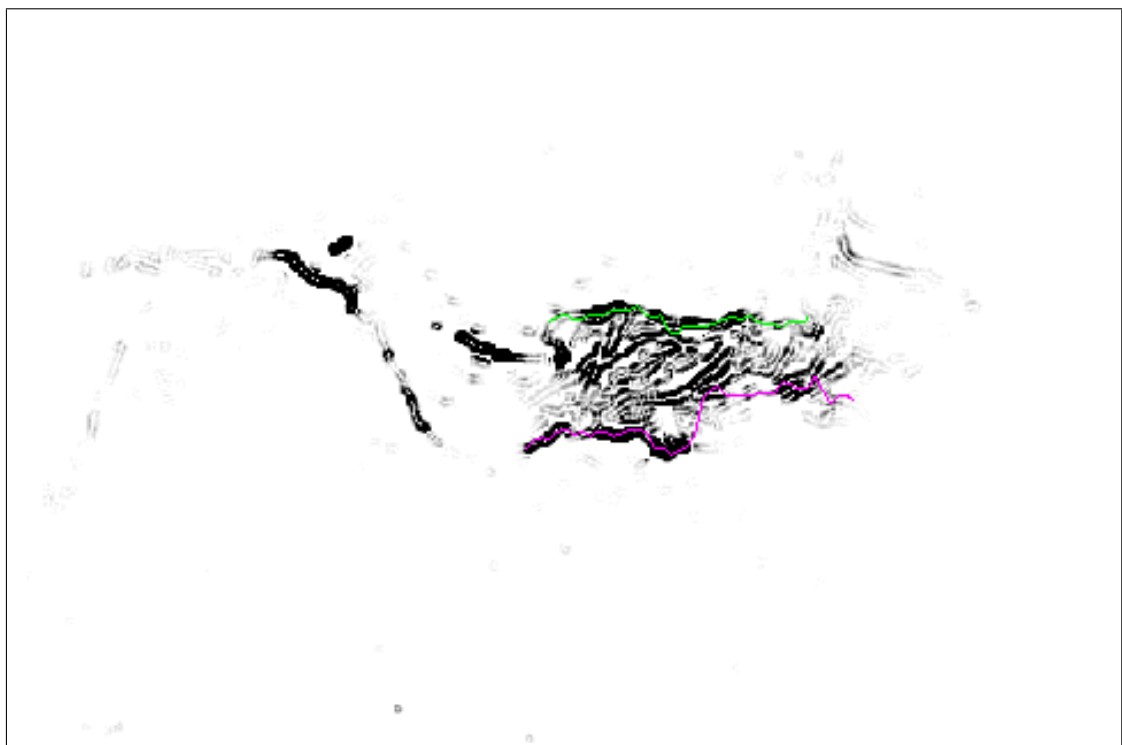


(b)

Figure 4.7: Images showing snakes on last image from 14th July 2000, (a) overlaid on original image, and (b) overlaid on edge image. In these images the snakes span the left most ribbon emission from this flare. The parameters used for these results are: upper snake - cont = 1.0, curv = 1.2, pressure = 5.0, grad = 0.40, ints = 0.0, te = 0.9986; lower snake - cont = 1.0, curv = 1.0, pressure = 4.5, grad = 0.40, ints = 0.0, te = 0.9980. For both snakes  $\sigma = 1.5$ .



(a)

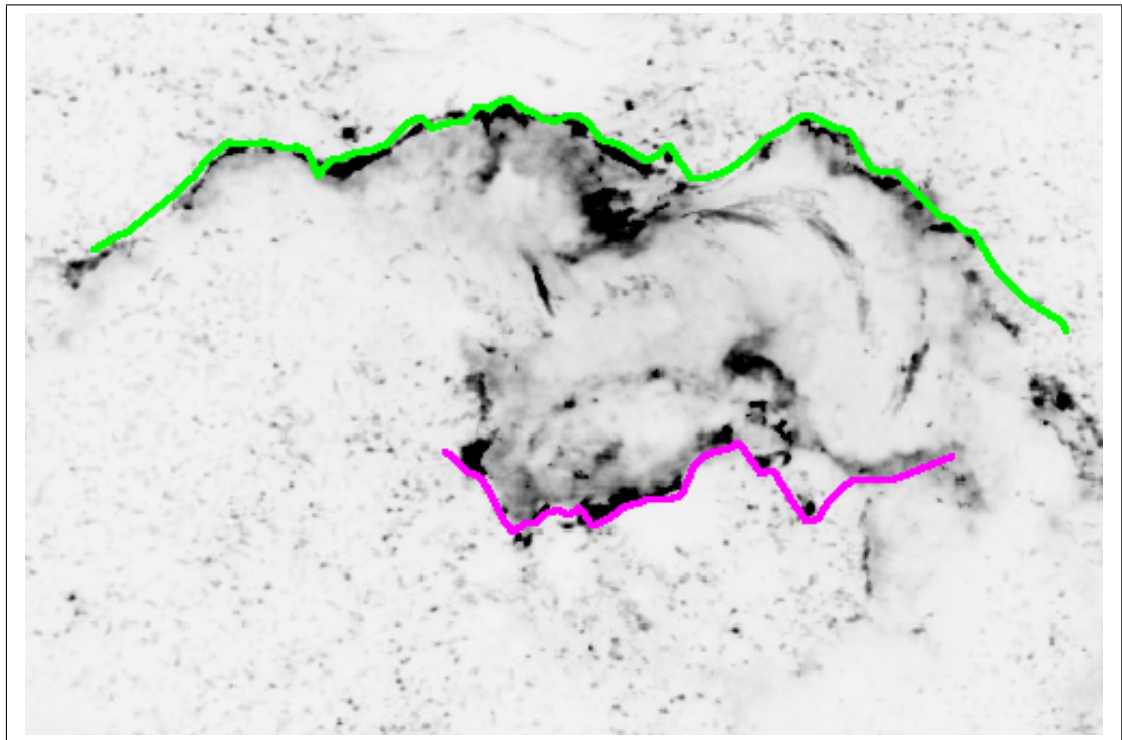


(b)

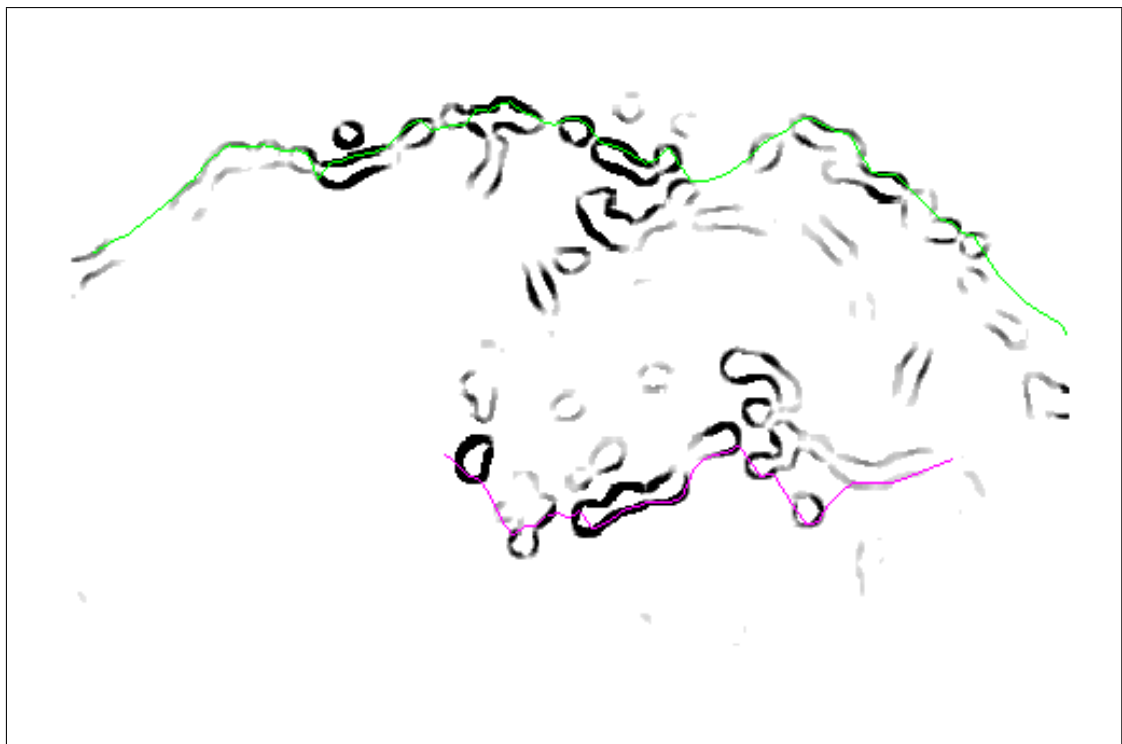
Figure 4.8: Images showing snakes on last image from 14th July 2000, (a) overlaid on original image, and (b) overlaid on edge image. In these images the snakes do not cover the left most section of ribbon emission. The parameters used for these results are: upper snake - cont = 1.0, curv = 1.2, pressure = 5.0, grad = 0.40, ints = 0.0, te = 0.9986; lower snake - cont = 1.0, curv = 1.0, pressure = 4.5, grad = 0.40, ints = 0.0, te = 0.9980. For both snakes  $\sigma = 1.5$ .

### 4.3.3 Flare 10th April 2001, 04:46 - 06:01, X2.3, 1600 Å

The ribbons of this flare span a large portion of the image width, and show a high degree of complexity and irregularity. As there are many bright point-like sources of emission close to the flare ribbons, and the ribbons appear bright and well defined, a high value was used for the LoG  $\sigma$  (4.2). This high value for  $\sigma$  removed some of the smaller point-like sources of emission, and as the ribbons were particularly strong, it was possible to apply such a high value of  $\sigma$  without blurring out parts of the ribbons. The ribbons from this flare were also close to the top of the image, so the SA initial temperatures were adjusted accordingly, as discussed in Section 4.3.1. The application of the snake algorithm to the last image in the sequence for this flare produces a good fit, see Figure 4.9. There are places on both ribbons where point-like sources of emission close to the ribbon edge have prevented both snakes from moving onto the ribbons, and the far right end of the upper snake is floating above the section of upper ribbon below it. The point-like sources are sufficiently large to appear in the edge image, despite the high LoG  $\sigma$  value. One such point near the centre of the upper ribbon appears as part of the ribbon in the edge image owing to the large LoG  $\sigma$  value. The strength and size of these point-like sources of emission make their removal difficult. The part of the upper snake to the far right of the upper ribbon, appears to be suspended above the ribbon. This is due to the model energy function preventing the snake from bending sufficiently for one of its nodes to reach the section of ribbon underneath. By decreasing the weight of the model energy function, the snake would be able to move onto this section of ribbon. However, this decrease in the model energy function would adversely affect the snake result in other places, where the snake is suspended over gaps in the ribbons in the edge image by the model energy function. Parameters for the algorithm may suit one part of a flare ribbon but do not necessarily suit the whole of that flare ribbon. The errors in the snakes for the last image of this flare are 3.8 px and 2.6 px for the upper and lower snake respectively. Both of these errors are significantly worse than the manual tracking error, despite the snake results qualitatively appearing very good. This can be explained by the large  $\sigma$  value used for the LoG filter for this image, as this results in both ribbons appearing smooth in the edge image and subsequently the snakes find the smooth edges of the ribbons in the edge image. The hand tracked result relies on the original image with no smoothing applied and as a result it follows the rough spiky edge of the ribbons. When the two results are compared, there is a difference along the entire length of the ribbon. This error, when combined with the error from a few places where the snakes do not match the ribbon well (e.g. the far right part of the upper ribbon) producing the seemingly large snake tracking errors.



(a)



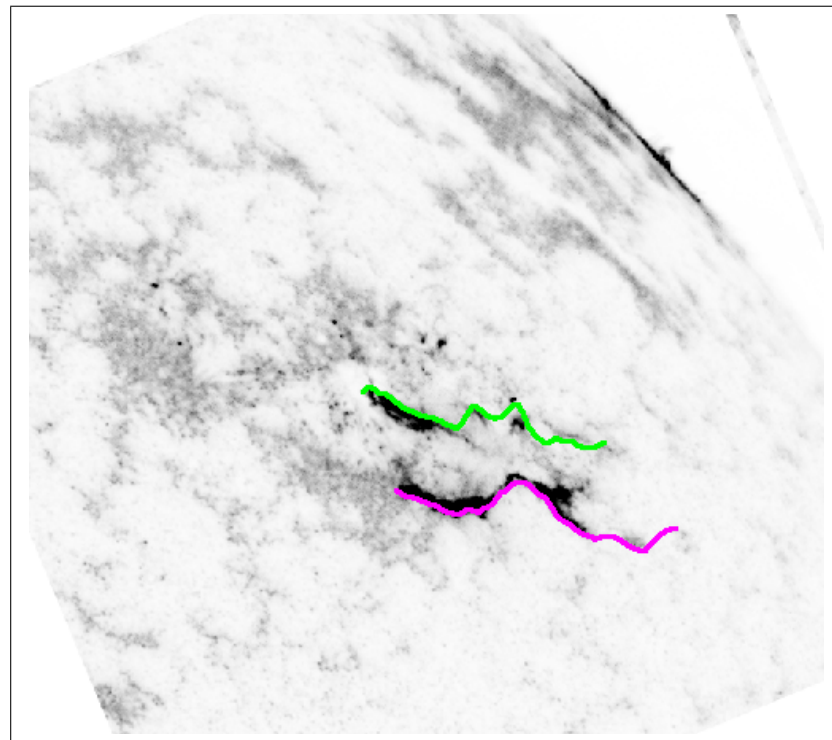
(b)

Figure 4.9: Images showing snake result on last image from 10th April 2001, (a) overlaid on original image, and (b) overlaid on edge image. The parameters used for these results are: upper snake - cont = 1.0, curv = 1.14, pressure = 5.0, grad = 1.6, ints = 0.0, te = 0.250; lower snake - cont = 1.0, curv = 3.71, pressure = 15.0, grad = 5.71, ints = 0.0, te = 0.9980. For both snakes  $\sigma = 4.2$ .

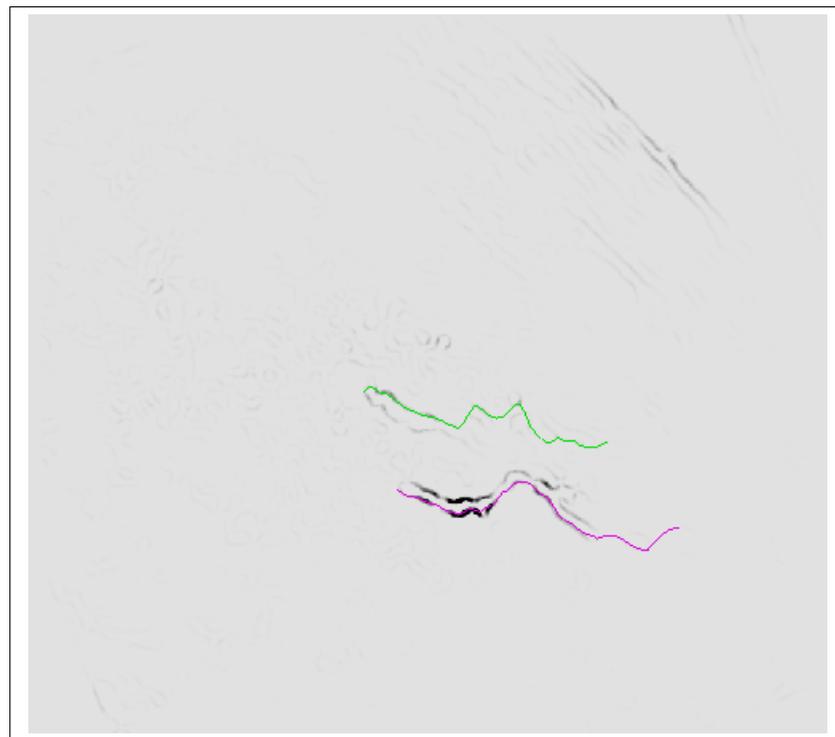
#### 4.3.4 Flare 25 June 2000, 07:36 - 08:40, M 1.9, 1600 Å

The result from the snake algorithm for this image is shown in Figure 4.10. The orientation of the ribbons in this flare were such that the images required rotating prior to use in our algorithm, as seen in the images of Figure 4.10. The rotation was carried out with a bi-linear interpolation code written for this purpose.

This flare appears close to the solar limb, with the image showing what appears to be another site of solar activity on the limb. This second area of bright emission presents a considerable obstacle for the upper snake as it moves downwards from the top of the image, as it appears much as a flare ribbon, i.e. a long thin area of bright emission. For this reason the role of SA was particularly important for the application of the snake algorithm to this image, and several adjustments to the SA initial temperature were needed to enable the snake to move past this feature. The lower ribbon of this flare appears strong and well defined, with the exception of the right-most section of ribbon. For part of this section of the ribbon it is hard to tell there is a ribbon present, but images earlier in the sequence indicate that the faint emission seen in this image is at the location of previously bright ribbon emission. The upper ribbon of this flare appears less well defined, particularly in its centre, where there are multiple areas of emission. What part of this emission should be defined as the leading edge is debatable, and where the manual result disagrees with the snake algorithm result, the error in the snake result shows a significant increase. The strong edge of a point-like source of emission close to the upper ribbon is seen to trap part of the upper snake, increasing the the LoG  $\sigma$  value to attempt to remove this feature from the edge image also removes the faint right section of the upper ribbon. The lower snake fits the lower ribbon particularly well, and with the exception of the ambiguous centre section and area close to the point feature, and the upper snake fits the upper ribbon well also. The tracking errors for the upper and lower snake are 3.8 px and 0.8 px respectively. The small error for the lower snake reflects the well defined appearance of the lower ribbon, and the larger error for the upper snake reflects the less well defined and complex nature of the upper ribbon.



(a)

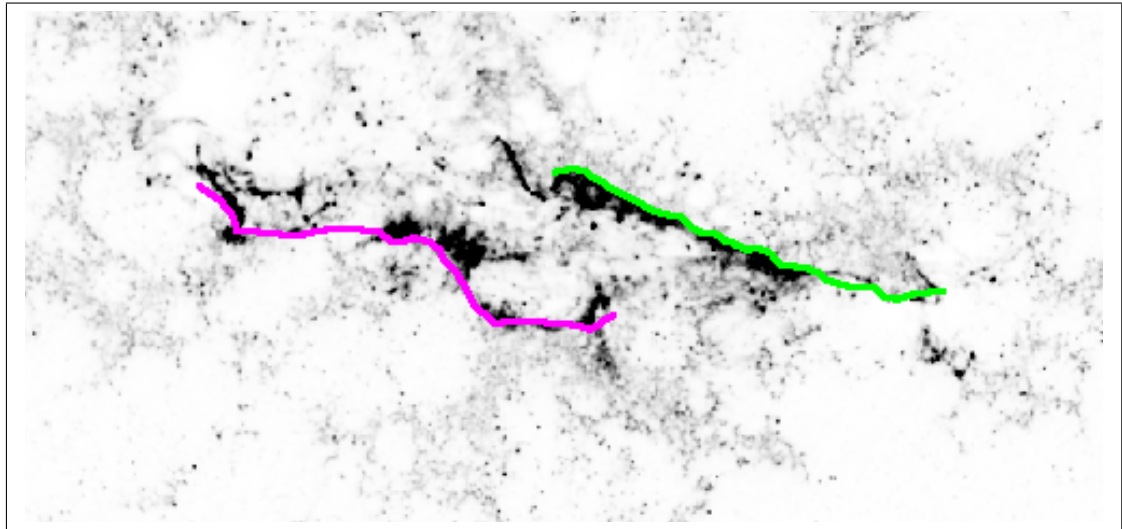


(b)

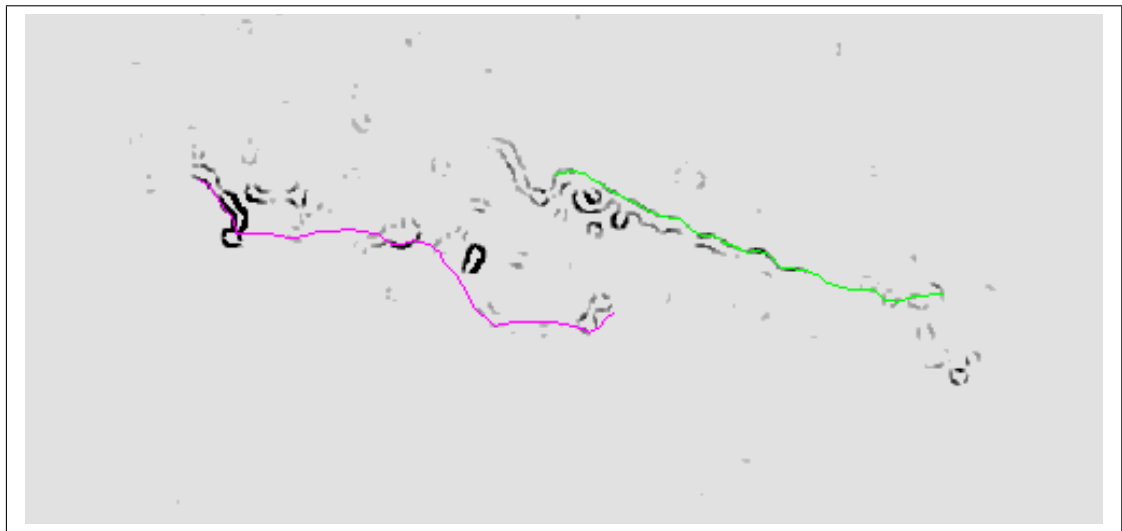
Figure 4.10: Images showing snakes on last image from 25th June 2000, (a) overlaid on original image, and (b) overlaid on edge image. The parameters used for these results are: upper snake - cont = 1.0, curv = 1.02, pressure = 9.6, grad = 1.6, ints = 1.0, te = 0.99835; lower snake - cont = 1.0, curv = 3.71, pressure = 17.86, grad = 5.71, ints = 0.0, te = 0.9980. For both snakes  $\sigma = 4.0$ .

### 4.3.5 Flare 12 November 1999, 08:39 - 09:49, 1600 Å

The last image in the time sequence for this flare shows a strong upper ribbon regular in shape, and three separate sections of bright emission that could be interpreted as belonging to one lower ribbon, but could equally be interpreted as three separate lower ribbons. The disjointed nature of the lower ribbon presents an interesting point for the design of automated flare ribbon tracking software. The snake algorithm assumes that there are only two ribbons in the image, and aims to locate one ribbon over the range of  $x$  coordinates specified by the user. The structure of the lower ribbon(s) of this flare calls into question whether this assumption should be made prior to running the algorithm and imposing the assumption on the data. For the benefit of examining the snake algorithm's performance we assumed that the emission was from one single lower ribbon. The result from the snake algorithm for this flare can be seen in Figure 4.3.5. The upper snake locates the upper ribbon accurately for most of its length, although the right-most section of the snake has moved past the ribbon in one small area, this part of the ribbon appears particularly faint in the edge image, owing to the fact it appears thin in the original image. The lower snake appears to fit the main areas of bright emission in the lower ribbon, although it does not fit a lot of the finer structure present. Again the tracking errors bear out the qualitative analysis, with the upper snake error of 1.0 px and the lower snake error of 3.0 px.



(a)



(b)

Figure 4.11: Images showing snakes on last image from 12th November 1999, (a) overlaid on original image, and (b) overlaid on edge image. The parameters used for these results are: upper snake - cont = 1.0, curv = 1.0, pressure = 11.4, grad = 2.85, ints = 0.0, te = 0.9993; lower snake - cont = 1.0, curv = 1.0, pressure = 8.89, grad = 2.23, ints = 0.0, te = 0.992. For both snakes  $\sigma = 5.0$ .

### 4.3.6 Flare 8th February 2000, 08:33 - 09:37, M1.3, 1600 Å

The morphology of this flare is interesting (see Figure 4.12) with the upper ribbon in particular having a complex and convoluted shape. The lower ribbon again appears to consist of three separate areas of bright emission, and again it is not clear whether the assumption that these regions should be interpreted as a single flare ribbon should be made. Our algorithm does not expressly prevent the snake from looping back under itself, but it is practically impossible for the snake to do so. The accurate location of the upper ribbon in this image would require a snake that was designed to loop back under itself, so instead we set a more realistic goal of only tracking the main part of the upper ribbon, shown highlighted in green in Figure 4.12. The result from the application of our algorithm on this flare is shown in Figure 4.13, where the upper snake shows a poor fit to the upper ribbon, but the lower snake shows a good fit for the lower ribbon. The upper snake is prevented from reaching the main section of the upper ribbon by a secondary part of the ribbon that has looped back from the far right of the ribbon, this secondary part of the ribbon is highlighted in pink Figure 4.12. As this secondary part of the ribbon is as bright and as thick as the main sections of ribbon, there is little that can be done to remove it other than manually deleting it from the image. By raising the SA temperature it is possible to let the snake move over this secondary section of ribbon, however this would result in the snake moving over the main sections of ribbon as well. In this case our algorithm needs additional manual intervention. In order to retain the utility of this flare as a means of testing the snake algorithm, we will use a manually traced ribbon position for the upper ribbon as a start position when applying the snake algorithm to the rest of the images in the sequence instead of this result. Whilst relying on substantial manual intervention this still enables the algorithm to semi-autonomously track the ribbons over the remaining images in the sequence.

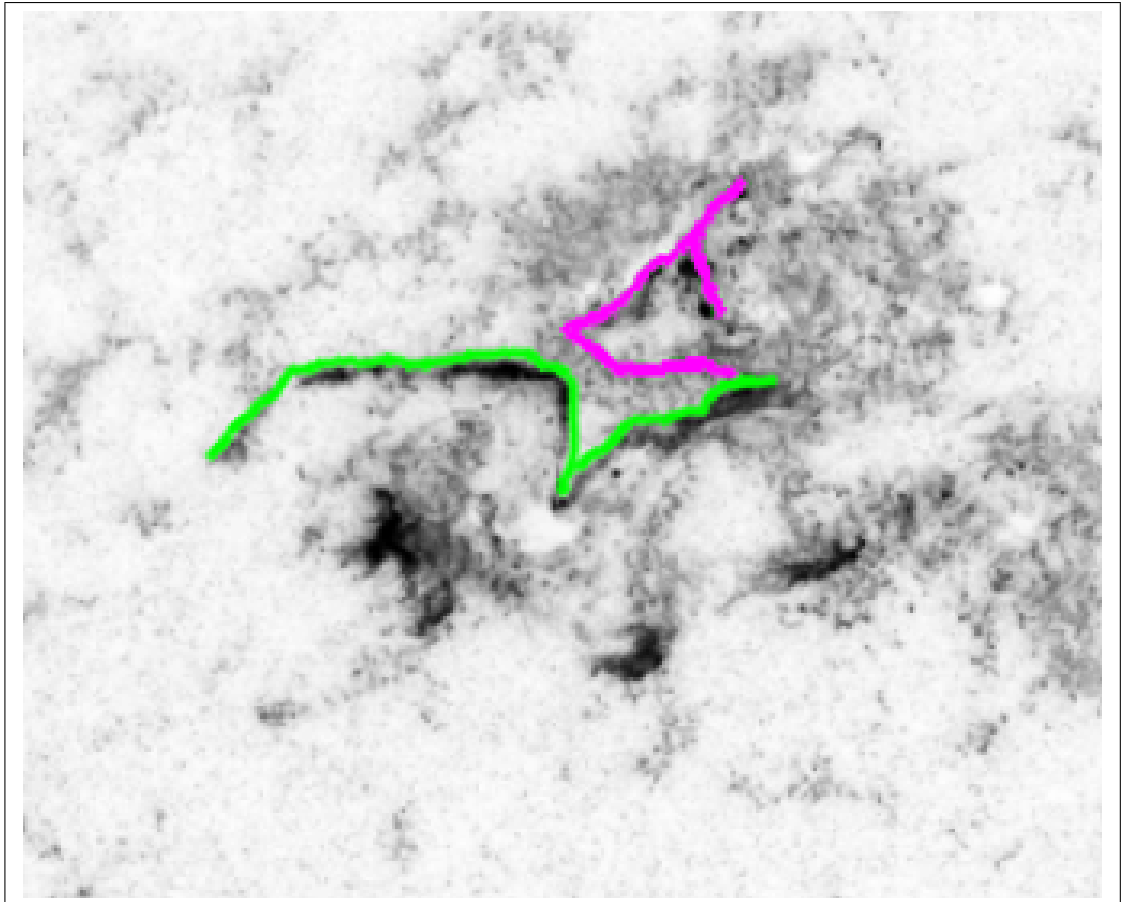
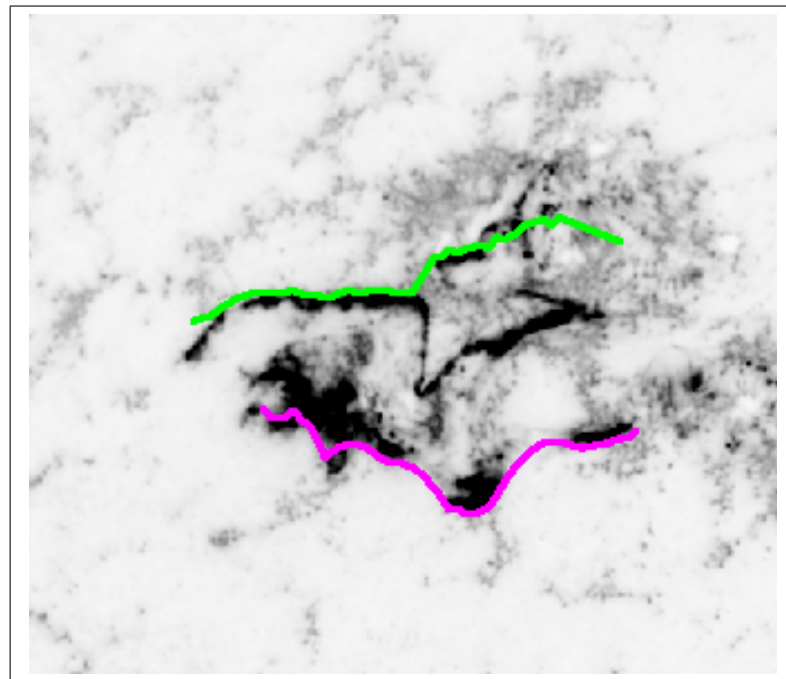
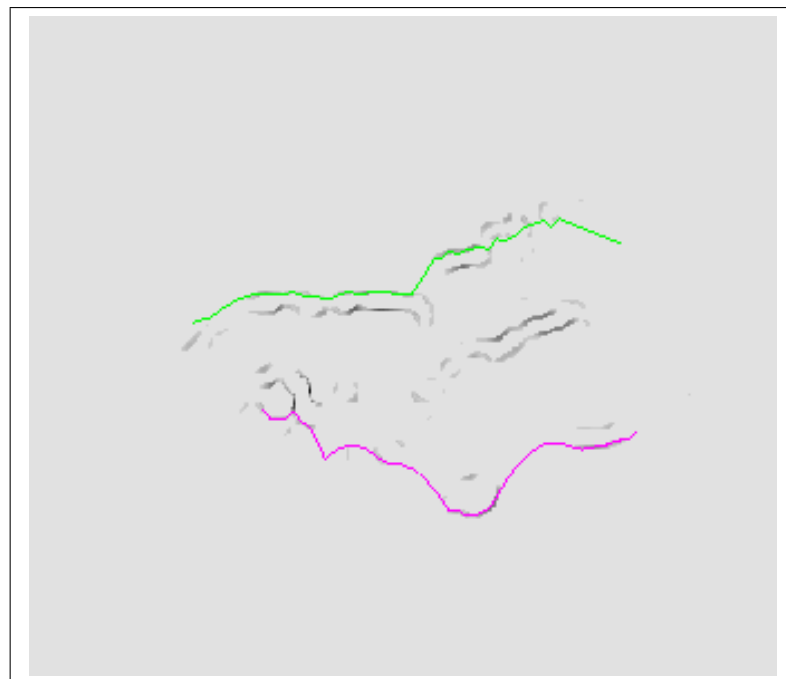


Figure 4.12: The last image in the 8th of February 2000 flare. The outline of the upper ribbon has been manually traced. The main part of the ribbon we try to locate is shown in green, and the other part of the ribbon that interferes with tracking the main part of the ribbon is shown in pink.



(a)



(b)

Figure 4.13: Images showing snakes on last image from 8th February 2000, (a) overlaid on original image, and (b) overlaid on edge image produced with a value of  $\sigma = 5.0$ . The parameters used for these results are: upper snake - cont = 1.0, curv = 2.33, pressure = 8.33, grad = 3.33, ints = 1.0, te = 0.9993; lower snake - cont = 1.0, curv = 10.0, pressure = 50.0, grad = 20.0, ints = 4.0, te = 0.9986. For both snakes  $\sigma = 5.0$ .

### 4.3.7 Summary of parameters used

The parameters of the algorithm used for the last image in each flare are summarised in Table 4.1. The parameters “cont”, “curv”, “pressure”, “grad” and “ints” are all relative weights. For easy comparison these weights are shown relative to the weighting of the “cont” parameter. The different values of  $\sigma$  used for the different flares show a wide range, indicative of the difference in the ribbons from different flares. The SA initial temperature parameter “te” mostly varies according to the distance of the ribbon from either the top or bottom of the images. The high degree of precision that the “te” values are quoted to show just how sensitive the snakes are to this parameter. Where flare ribbons appear strong and continuous in their edge images, the associated model energy parameters “cont” and “curv” are smaller than the data energy parameters “grad” and “ints”. Where the network emission is strong compared to the flare ribbons, and has not been blurred out by the LoG filter, the pressure parameter needs to be non-zero, with larger values needed where the edges of the network appear brighter in the edge image. The low weighting of the cont sub-function relative to the other sub-functions for the lower snake for the 8th February is because the lower ribbon takes the form of three separate sections with a considerable distance in the image  $y$  coordinate between the start of one section and the end of another. The parameters listed here for each flare were used as the defaults for the algorithm when processing the remaining images in the sequence.

Flare	$\sigma$	cont	curv	pressure	grad	ints	te	Snake
20th Jan 2001	4.0	1.00	1.00	5.54	0.834	0	0.5600	Upper
20th Jan 2001	4.0	1.00	1.00	5.31	0.625	0	0.9980	Lower
14th Jul 2000	1.5	1.00	1.20	5.00	0.400	0	0.9986	Upper
14th Jul 2000	1.5	1.00	1.00	4.50	0.400	0	0.9980	Lower
10th Apr 2001	4.2	1.00	1.14	5.00	1.60	0	0.2500	Upper
10th Apr 2001	4.2	1.00	3.71	15.0	5.71	0	0.9980	Lower
25th Jun 2000	4.0	1.00	1.02	9.60	1.60	1	0.9984	Upper
25th Jun 2000	4.0	1.00	3.71	17.9	5.71	0	0.9980	Lower
12th Nov 1999	5.0	1.00	1.00	11.4	2.85	0	0.9930	Upper
12th Nov 1999	5.0	1.00	1.00	8.89	2.23	0	0.9920	Lower
8th Feb 2000	5.0	1.00	2.33	8.33	3.33	1	0.9993	Upper
8th Feb 2000	5.0	1.00	10.00	50.0	20.0	4	0.9986	Lower

Table 4.1: Table showing the parameters used for the snake algorithm for different flares. The parameters cont, curv, pressure, grad and ints are all relative weights. For easy comparison these weights are shown relative to the weighting of the cont parameter. The  $\sigma$  parameter is the value used in the LoG filter, and the te parameter is the initial temperature used for simulated annealing.

## 4.4 Tracking Flare Ribbons Through the Image Sequence

We now take a look at the results obtained from the second stage of our algorithm, i.e. the tracking of the ribbons through the rest of the images in the sequence for each flare. Again we start with the flare from 20th January 2001, and use this as an example to run through the procedure we used to apply our algorithm to the flares presented here. As our snakes start close to the ribbons we do not apply SA for these images. If we were to apply SA, the snakes would move past the ribbons immediately and come to rest on the top and bottom of the image. It should also be noted that the start positions of the nodes of the snake are shifted away from the ribbon (either up or down) by five pixels from the previous snake result, before the snake is started on each image. Whether this shift should be included is debatable. Without the shift, with consecutive images that appear very similar with no real ribbon movement it would be difficult to tell whether the snake parameters are producing a snake that finds the ribbon or a snake that simply does not move. Without the shift, if a snake moves past a ribbon in one image, there is no chance of the snake locating this ribbon in any of the images remaining to be processed. The observed general behaviour of flare ribbons is to spread apart over time. Without the shift this property would be hard-coded into the snakes - they would only be able to move apart with time, with the shift it is possible for the snakes to move against this observed direction of ribbon motion from image to image.

### 4.4.1 Flare 20 January 2001, 20:46 - 21:16, M7.7, 1600 Å

Starting from the position of the ribbons from the last image in the sequence, the snake algorithm is applied to the remaining images in the sequence for this flare. There are 51 images in this sequence, numbered from 0 to 50, with image 0 representing the earliest image in time, and image 50 the latest. We used the parameter set obtained from applying our algorithm to image number 51, the last image, as described in Section 4.3.1, with difference of the SA initial temperature set to zero.

The tracking errors for this original result are shown in Figure 4.14. The errors in the upper snake are small for the last 20 images, but then show a substantial increase in the earlier images. The errors for the lower snake are a little less encouraging, the reason for this being that this ribbon appears much fainter, and the ribbon splits into two parallel sections of ribbon. This is discussed in more detail later on. By looking at the images and the associated edge images where the upper snake error is seen to increase (see Figure 4.16) the reason for the increase in error becomes apparent. The fainter and thinner sections of the upper ribbon do not appear in

the edge image, and so the snake is pushed down the image past the ribbons by the pressure function. The elasticity of the snake as a result of the model energy function results in the section of snake where no ribbon edges were present pulling part of the section of the snake where there are ribbon edges off the ribbon. The LoG filter has blurred the far right part of the ribbon into the background, so by using a lower value for the LoG  $\sigma$  parameter it was possible to prevent this from happening. The second run of the algorithm on this image sequence used a lower value for the LoG  $\sigma$ , with a much improved result for the upper ribbon.

The lower ribbon is split into two parallel parts, which present two different edges for the lower ribbon, with the lower snake tracking the outermost part of the ribbon when this is sufficiently bright, but when this fades the lower snake is seen to move past this part and onto the brighter section of ribbon behind it. An observer viewing the image sequence in order may decide to continue to specify this outer part of the ribbon as the leading edge after it has faded sufficiently to be ignored by the snake. In such cases it is not always clear, even to the observer, which part of the ribbon should be defined as the leading edge. As the snake starting position on a new image is shifted by 5 pixels, our algorithm retains the ability to track this leading edge of the flare ribbon, despite the fact that in later images in the sequence (which are processed first), the snake has already moved past this position.

Figures 4.17 to 4.19 show the snake tracking result with the revised parameter set on a selection of the images from the sequence. In general the results from the snake algorithm appear to fit the ribbons well, with the upper snake showing a better fit than the lower snake. This qualitative assessment is verified by the graph shown in Figure 4.15, where the error in the tracking result is shown for each image in the sequence. The upper snake remains consistently close to the manual tracking error, whilst the lower ribbon shows a much larger error, particularly in the last 20 images. The last 20 images show the lower ribbon considerably fainter than in the previous images, and the lower snake can be seen to locate the upper edge of this ribbon rather than the leading lower edge, which accounts for some of the error. Where the lower ribbon is brighter the lower snake locates the leading lower edge of the ribbon, and the error is visibly reduced. The error in the lower snake result is gradually reduced as the image number approaches zero, where the lower ribbon appears brighter and more uniform in shape. The result of algorithm on the first image in the sequence appears inconsistent, as the upper snake is longer than the upper ribbon. The extra length of the snake makes the result look untidy. Despite the poor appearance the error calculated for the snakes remains low. This is because only the sections of the snake and the manually traced ribbon that overlap each other in the x axis of the image are used for the calculation of the snake tracking error. It could be argued that this is a flaw in the measure of the snake tracking error,

however, it is not possible to compare the manual result with the snake result where they do not overlap. It would be possible to measure how close the start and end of the snake result is to the manual result, but as the start and end  $x$  coordinates of the snake are defined by the user, this makes little sense.

Figure 4.20 shows the snake tracking result from a number of images from this sequence overlaid onto the first image. The aim of this is to show the ribbon evolution, although where the tracking result is poor the image will be of little use. The tracking errors for this flare are low enough to make this “ribbon evolution image” interesting. The spreading of the ribbons over time is clear to see, but an increase or decrease in the complexity of the ribbons is not apparent. With the aid of the underlying image it is also possible to see the lengthening of the upper ribbon, despite the snake results not representing this change in length. It is also possible to observe that the upper ribbon appears to move toward and roughly takes the form of the edge of part of the network visible in this first image.

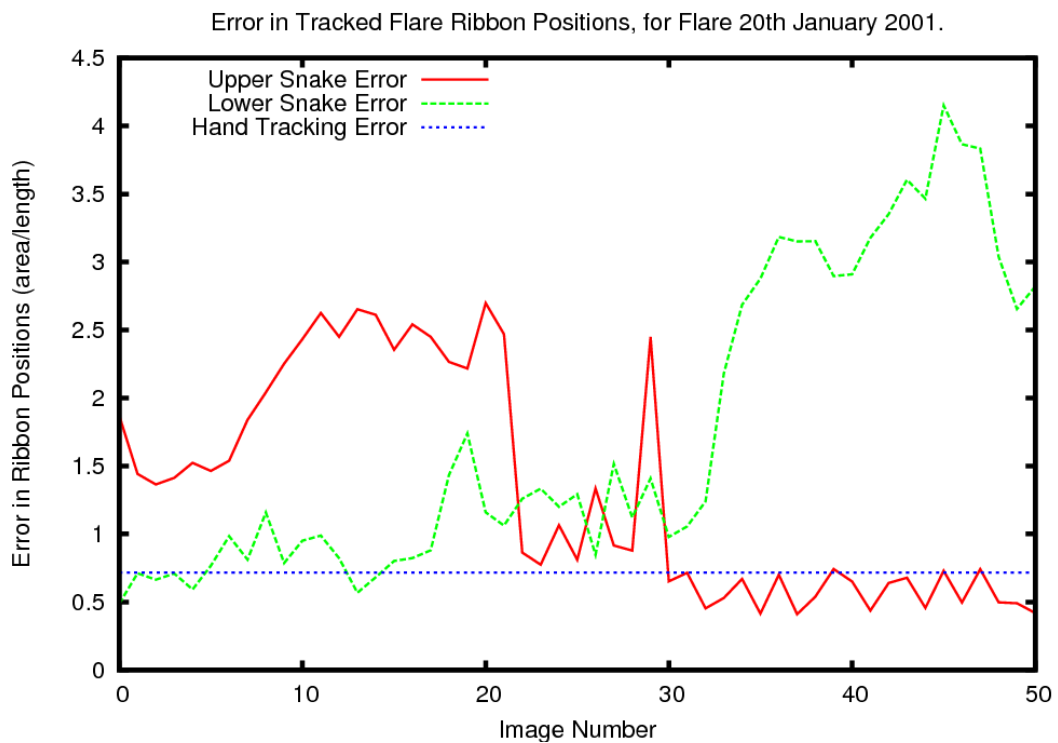


Figure 4.14: Graph showing the error in the upper and lower snake in tracking the upper and lower ribbon for images from the 20th January 2001 flare image sequence, second sequence. These results are from the first run where the parameters used for these results are: upper snake - cont = 1.0, curv = 1.0, pressure = 5.54, grad = 0.834, ints = 0.0; lower snake - cont = 1.0, curv = 1.0, pressure = 5.31, grad = 0.625, ints = 0.0. For both snakes  $\sigma = 4.0$ .

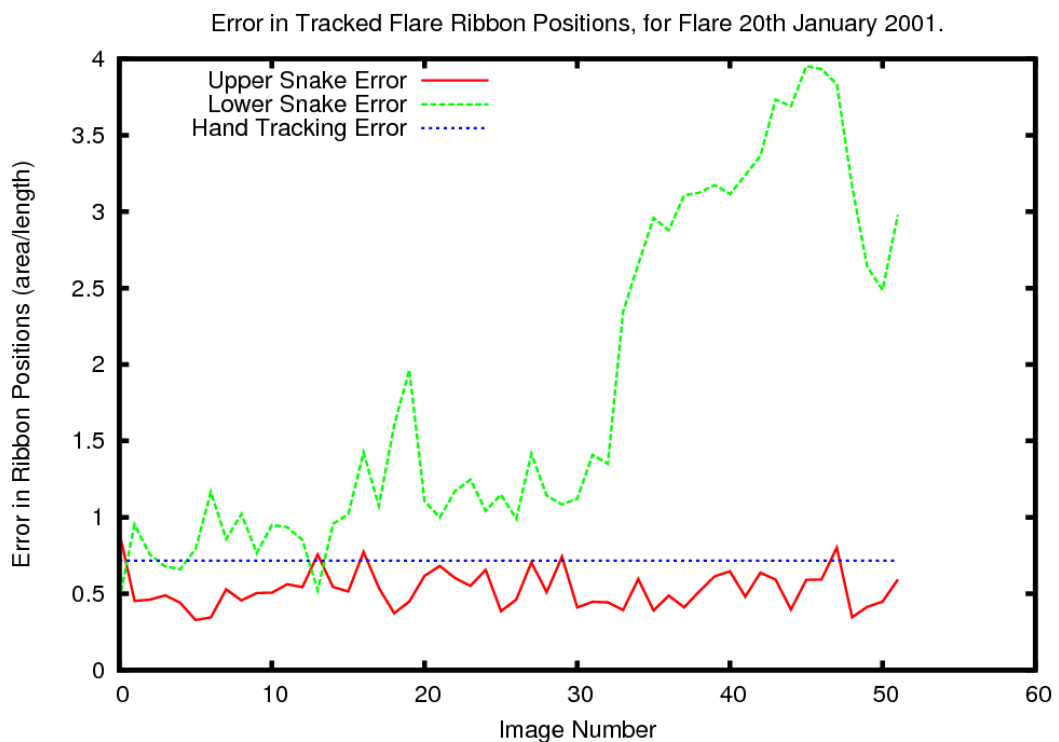
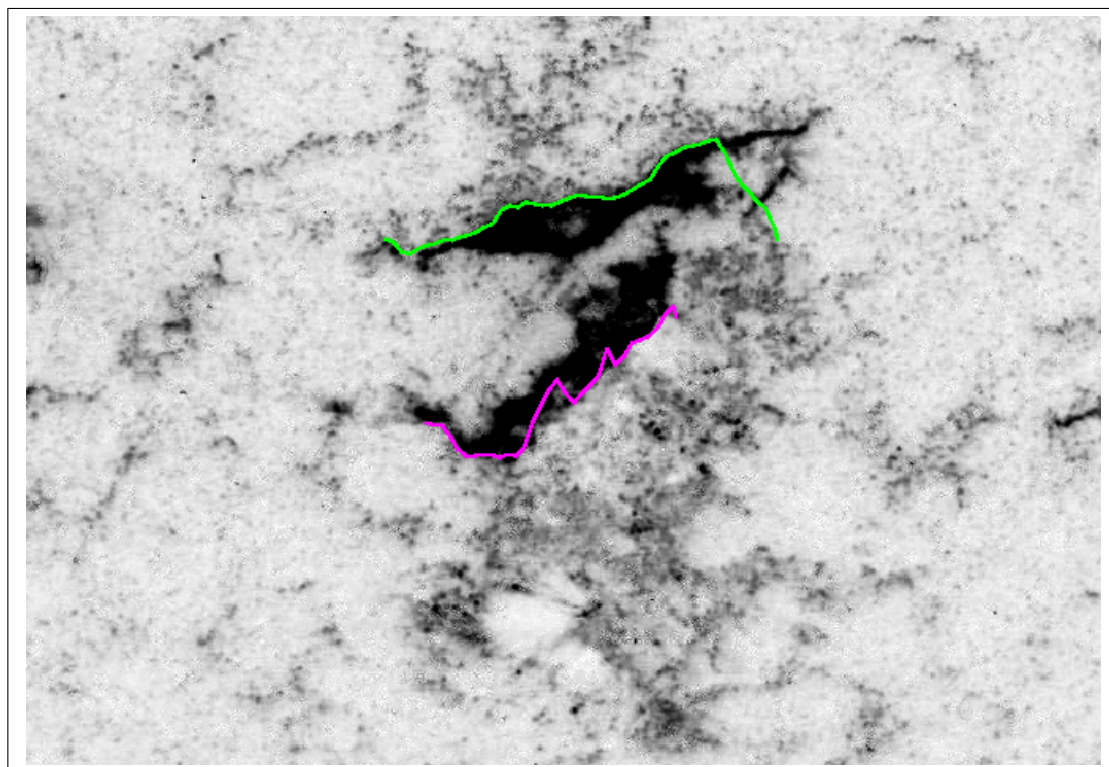
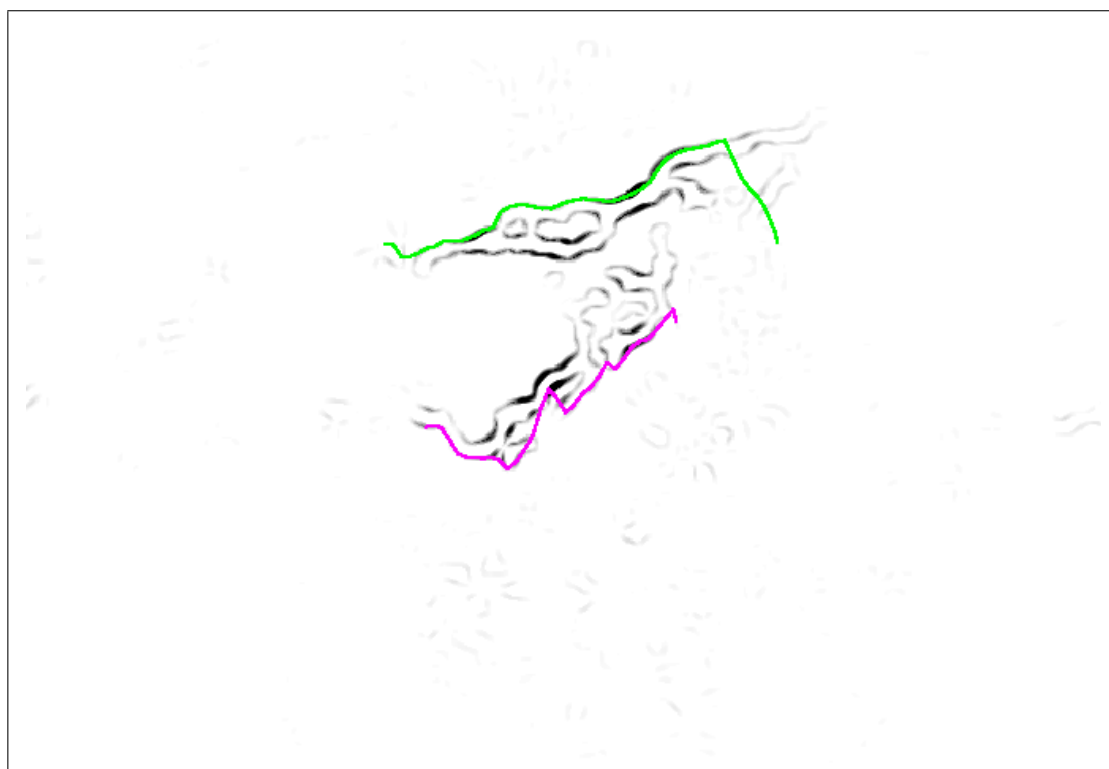


Figure 4.15: Graph showing the error in the upper and lower snake in tracking the upper and lower ribbon for images from the 20th January 2001 flare image sequence. These results are from the second run, which used a lower value for the LoG  $\sigma$  value, but otherwise an identical parameter set as the first run. The parameters used for these results are: upper snake - cont = 1.0, curv = 1.0, pressure = 5.54, grad = 0.834, ints = 0.0; lower snake - cont = 1.0, curv = 1.0, pressure = 5.31, grad = 0.625, ints = 0.0. For both snakes  $\sigma = 3.5$ .

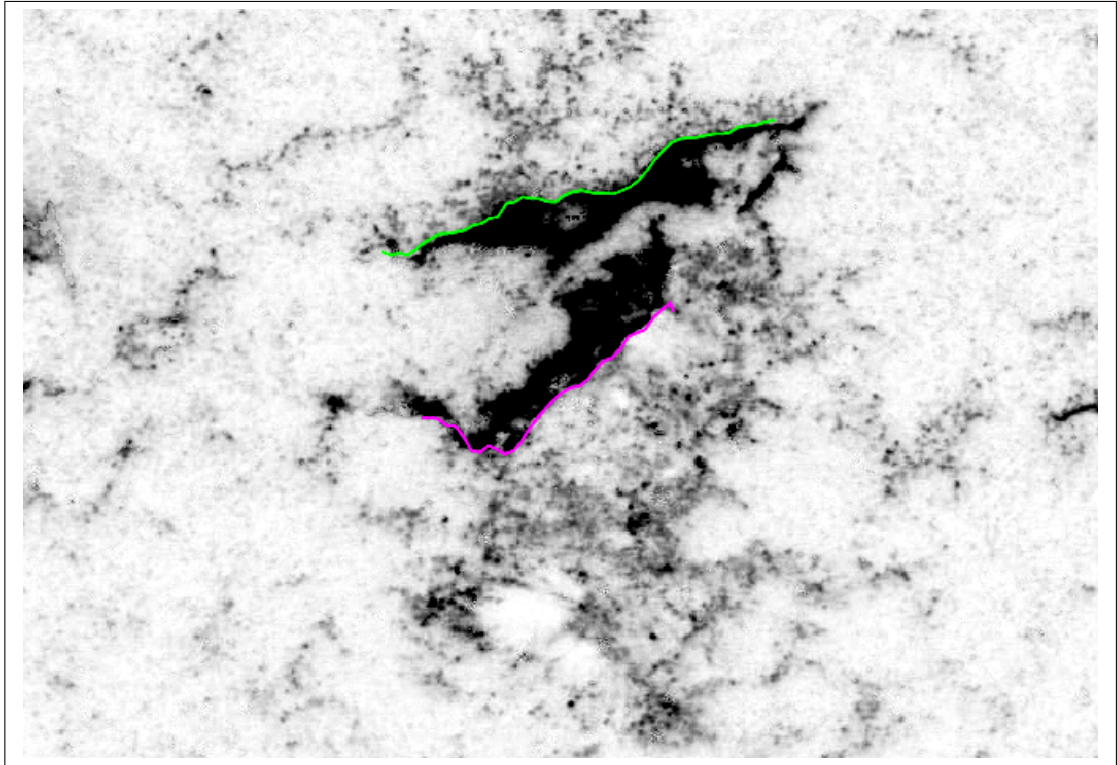


(a)

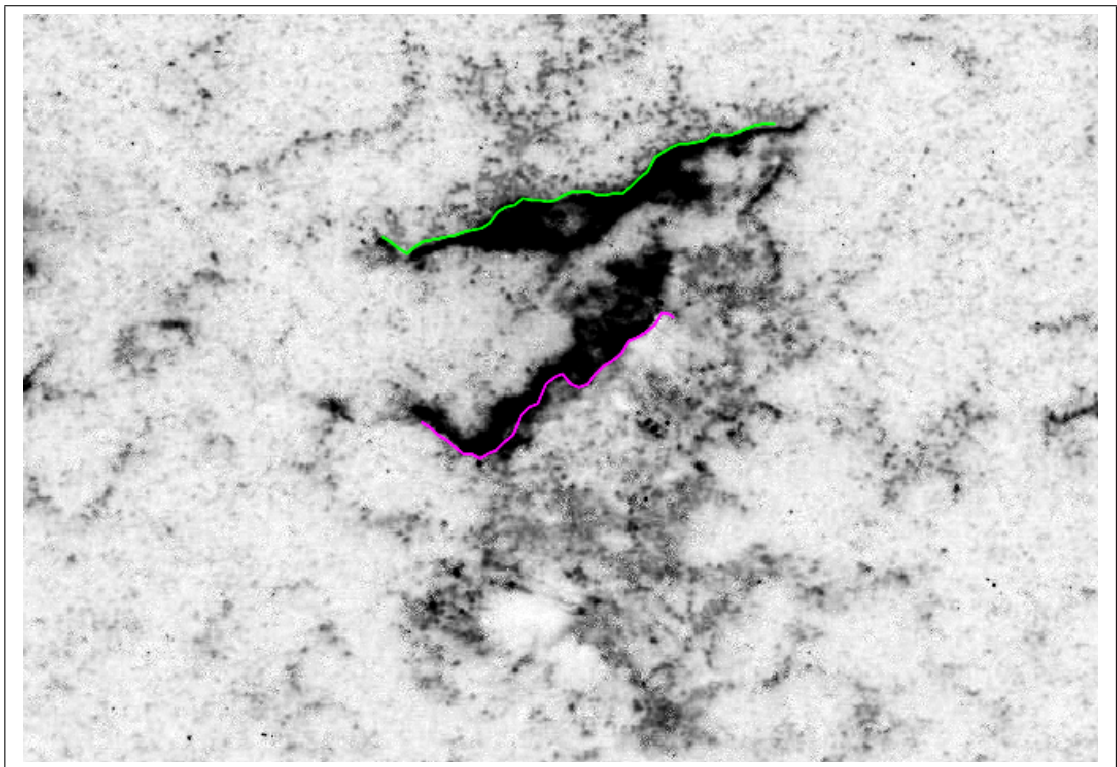


(b)

Figure 4.16: An image (a), and an edge image (b), showing the tracked ribbon positions for an image from the 20th January 2001 flare for the first application of the algorithm on the image sequence. The far right section of the upper ribbon can be seen to be missing in the edge image, and the upper snake is seen to therefore move past the location of this section of the ribbon.

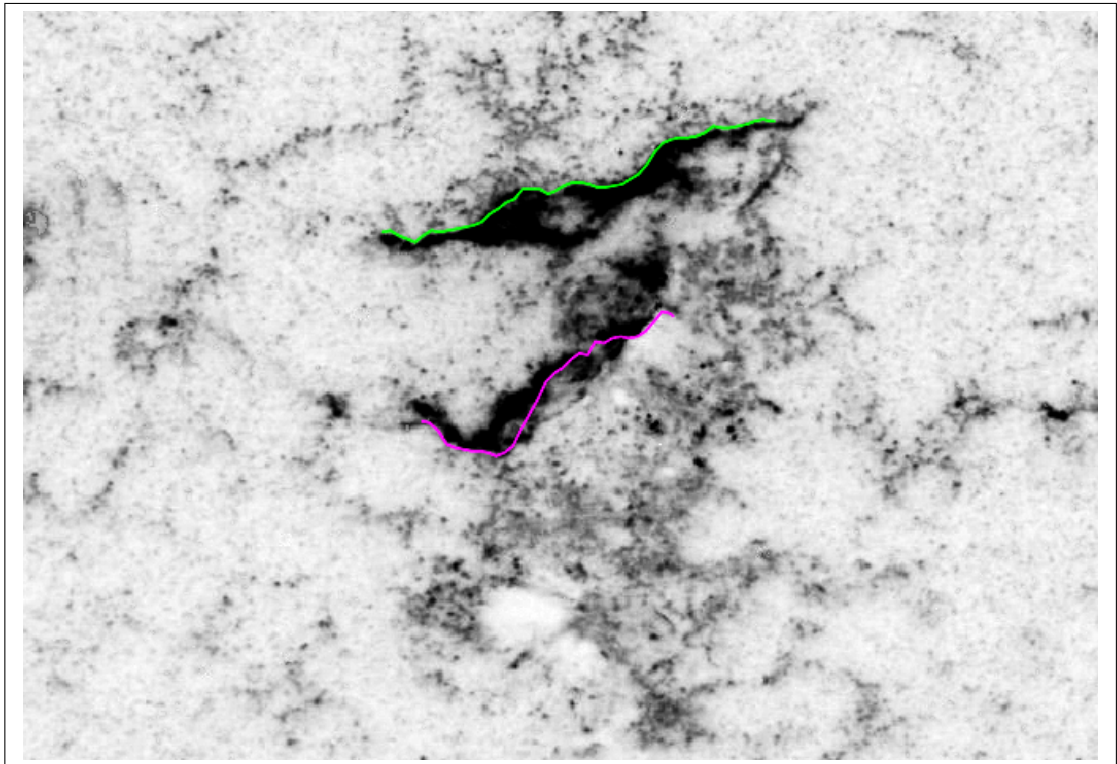


(a)

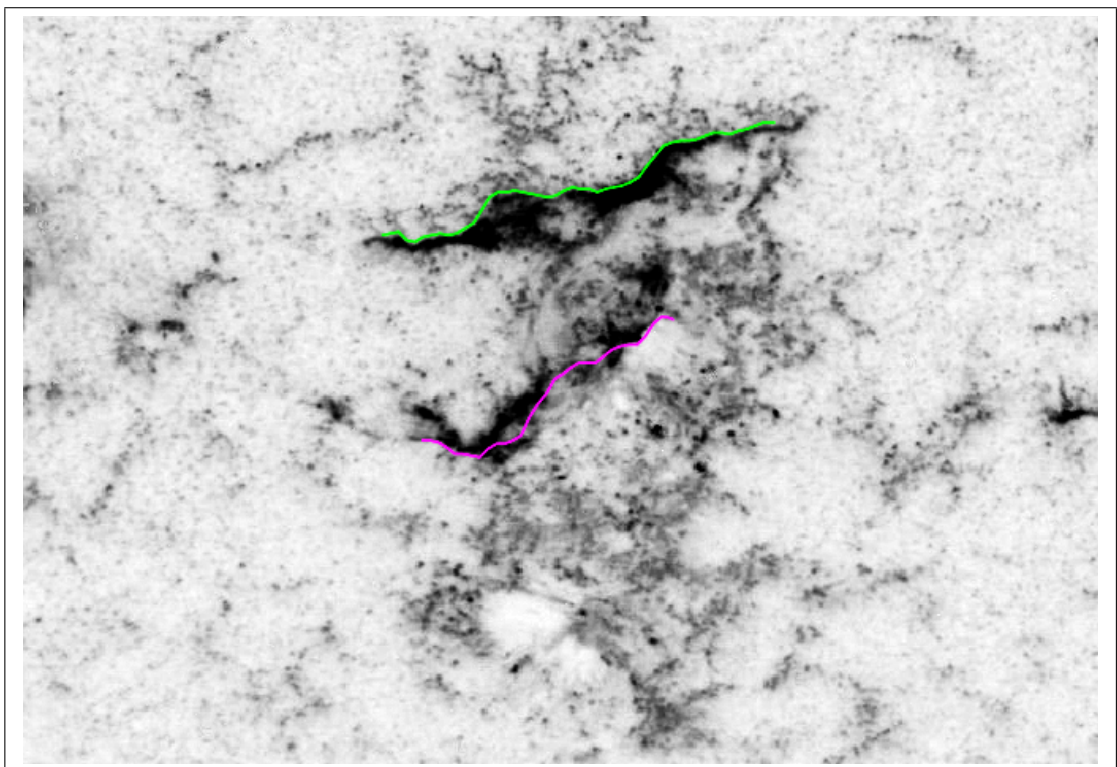


(b)

Figure 4.17: Images showing the tracked ribbon positions for images from the 20th January 2001 flare. Image (a) no. 005, (b) no. 010. The parameters used for these results are: upper snake - cont = 1.0, curv = 1.0, pressure = 5.54, grad = 0.834, ints = 0.0; lower snake - cont = 1.0, curv = 1.0, pressure = 5.31, grad = 0.625, ints = 0.0. For both snakes  $\sigma = 3.5$ .

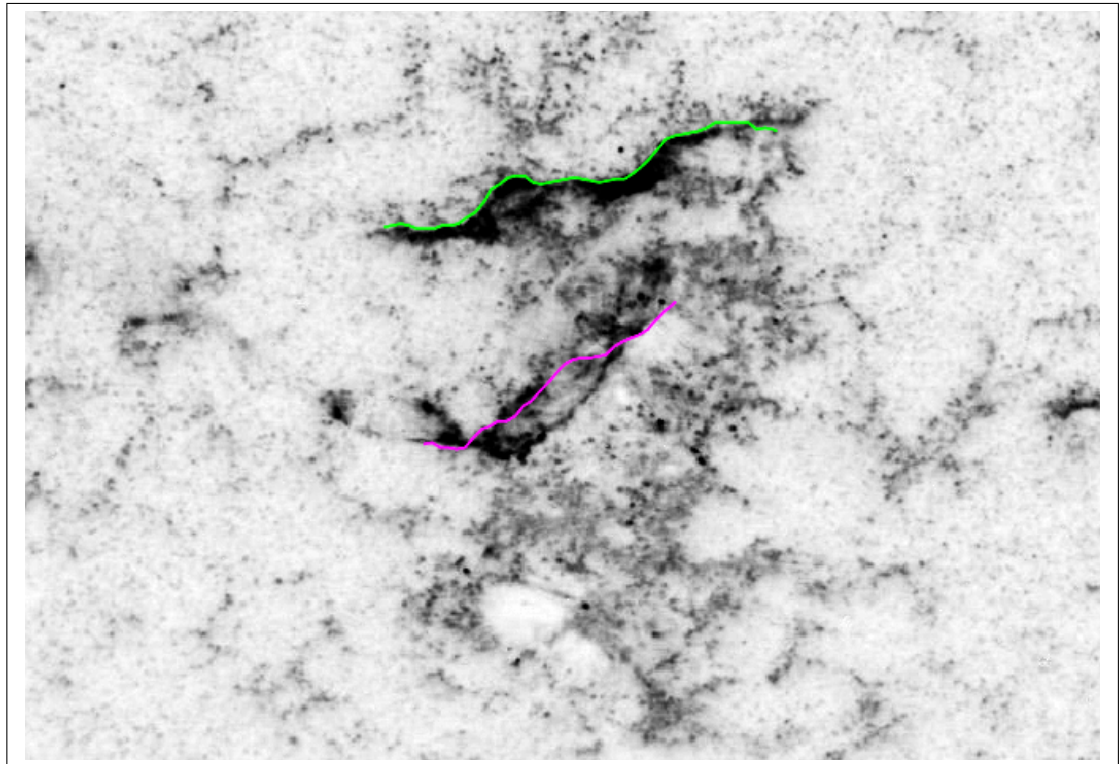


(a)

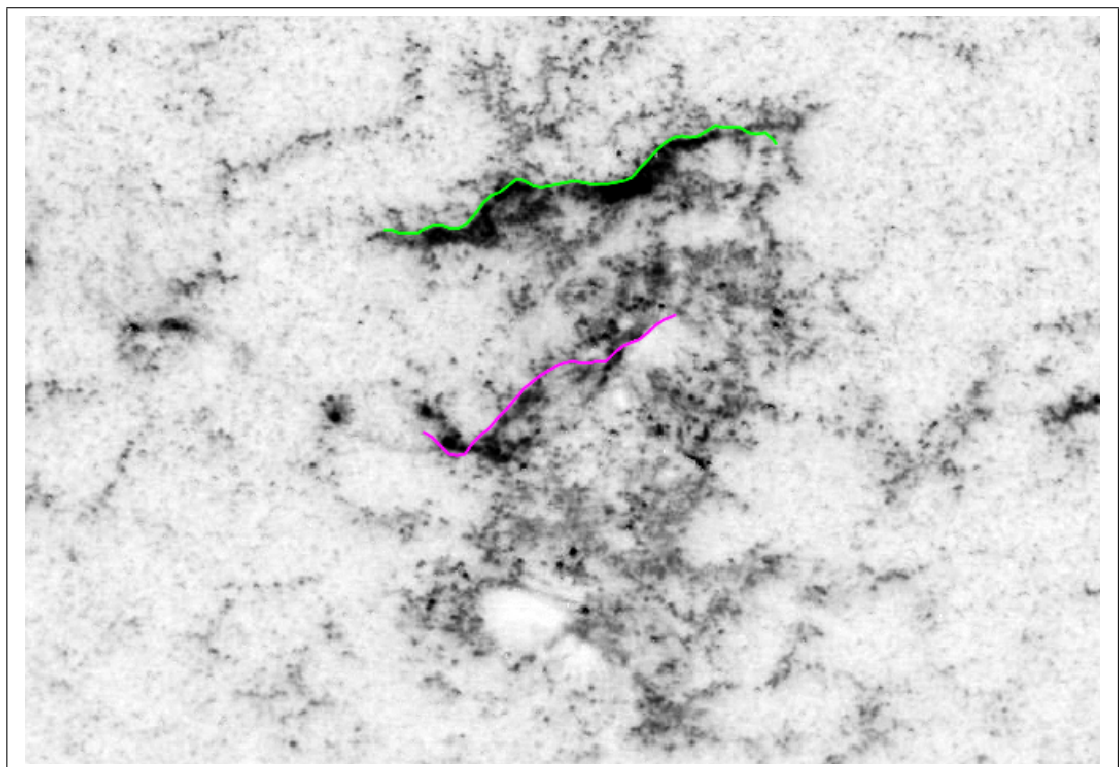


(b)

Figure 4.18: Images showing the tracked ribbon positions for images from the 20th January 2001 flare. Image (a) no. 020, (b) no. 030. The parameters used for these results are: upper snake - cont = 1.0, curv = 1.0, pressure = 5.54, grad = 0.834, ints = 0.0; lower snake - cont = 1.0, curv = 1.0, pressure = 5.31, grad = 0.625, ints = 0.0. For both snakes  $\sigma = 3.5$ .



(a)



(b)

Figure 4.19: Images showing the tracked ribbon positions for images from the 20th January 2001 flare. Image (a) no. 040, (b) no. 050. The parameters used for these results are: upper snake - cont = 1.0, curv = 1.0, pressure = 5.54, grad = 0.834, ints = 0.0; lower snake - cont = 1.0, curv = 1.0, pressure = 5.31, grad = 0.625, ints = 0.0. For both snakes  $\sigma = 3.5$ .

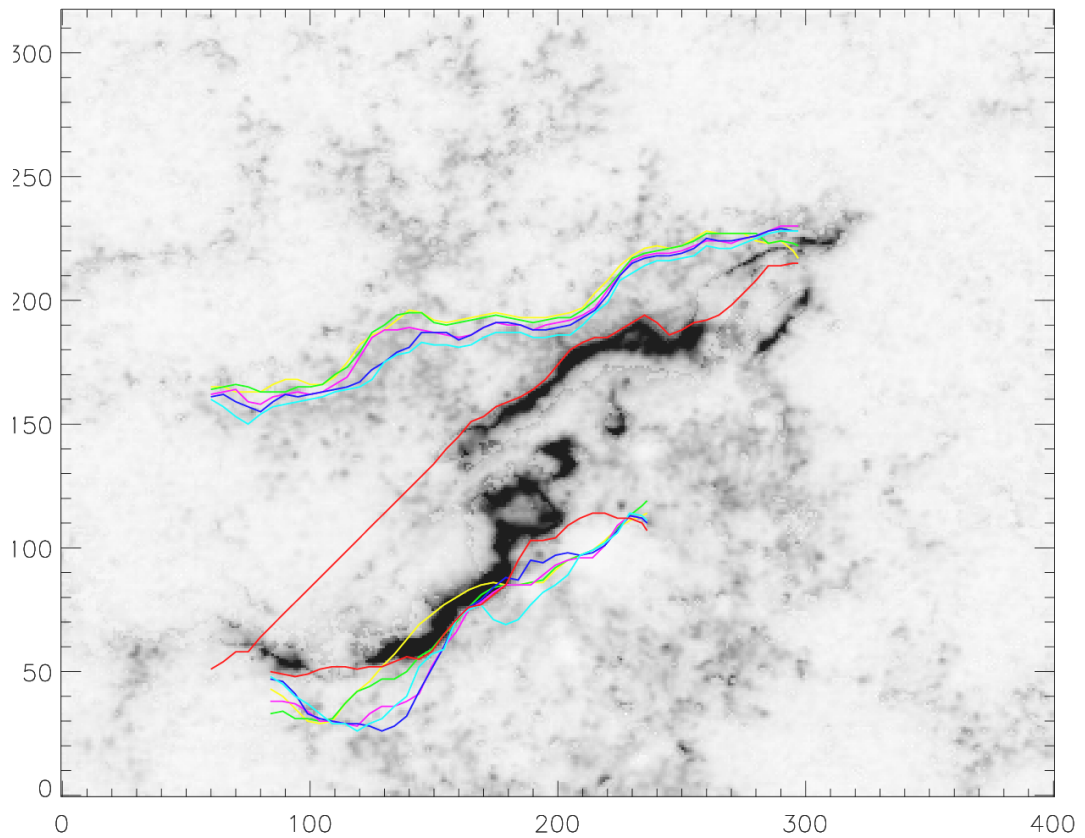


Figure 4.20: The first image of the 20th Jan 2001 flare sequence, with the tracked ribbon positions for images numbered 0, 10, 20, 30, 40 and 50 shown in red, cyan, blue, pink, green and yellow respectively. The parameters used for these results are: upper snake - cont = 1.0, curv = 1.0, pressure = 5.54, grad = 0.834, ints = 0.0; lower snake - cont = 1.0, curv = 1.0, pressure = 5.31, grad = 0.625, ints = 0.0. For both snakes  $\sigma = 3.5$ .

#### 4.4.2 Flare 14 July 2000, 09:43 - 11:02, X5.7, 195 Å

For this part of the snake algorithm a new method for producing edge images was trialled, the motivation for this being the difference between the 195 Å images and the 1600 Å images. With the 1600 Å images there are large amounts of network in the images causing potential problems for the snake algorithm. By producing an edge image where the strength of the edge is represented, the weaker edges that are generally formed by the network are less likely to trap the snake than the stronger edges formed by the flare ribbons. With the 195 Å images the lack of network and the presence of flare loops means that the stronger edges are generally produced by the flare loops, and the weaker edges are produced by the flare ribbons, thus producing an edge image where the snake is likely to move over the weaker edges of the ribbons and onto the stronger edges of the flare loops. Our new method for producing an edge image took the standard edge image, where pixels of higher intensity represent stronger edges in the original image, as an input. From this input the very weakest edges were completely removed through thresholding and all the remaining edges above this lower threshold were assigned one uniform intensity value. The idea is that the snake will no longer preferentially come to rest on the loop edges, as they are no longer shown in the edge image as stronger edges and so no longer represent a lower energy in the image gradient sub-function.

The tracking error results from the algorithm using both the standard and new edge image method can be seen in Figure 4.21. The errors for both methods appear very similar, but surprisingly the standard edge image method results in a snake with smaller tracking errors. The error for the upper snake for both edge image methods is close to the benchmark for the manual tracking error for most images. The lower snake tracking errors are significantly worse than the hand tracking error in all images. The reason for the poor snake tracking of the lower ribbon is that the far right section of the lower ribbon blends smoothly into the background, and therefore does not appear in the edge image. The lack of a strong ribbon edge results in the lower snake locating the lower edge of the flare loops rather than the lower ribbon. A human observer finds this much less of a problem and is able to intuitively trace the vague edge of this tenuous section of ribbon.

A qualitative comparison of the two results shows that the new method produces snakes that round off many of the sharp features of the ribbons, and generally lie close to the ribbons along most of their length without following the shape of the ribbons, see Figure 4.22. The new method does lie closer to the faint ribbon edge than the standard method in the tenuous right section of the lower ribbon. The result from the standard method shows a snake that has come to rest on the flare loop rather than the lower right section of the ribbon. In general the result from

the standard method shows a snake that is more able to deform to the shape of the ribbons than the snake from the new method, and it is this ability that produces a lower tracking error for the standard method.

The results from this flare, using the standard method for edge image production, are shown for a selection of images in Figures 4.23 to 4.26. The results in general are worse than for the 20th January 200 flare. Again the lower snakes are seen to have larger errors than the upper snakes. The larger errors for the lower snake are explained by the area to the far right of the lower ribbon, where the ribbon emission fades gradually into the background. Whether the snake tracking should be compared to this section of the flare can be questioned, but it is included nevertheless. The relative weight of the model energy function is set high in comparison to the data energy function for this flare in order to prevent sections of the snake being pulled past the ribbon onto the stronger edges of the flare loops. This weighting of the parameters has the disadvantage of preventing the snake from deforming to the finer structure of the flare ribbons (although the results from the standard method still show a better ability for this than the results from the new method).

The evolution of the ribbons over time is again shown on one image, Figure 4.27. The separation of the ribbons over time is apparent in the snake positions. The ribbons appear to be more contorted and complex earlier in the image sequence, although the snake positions in the earlier images are hard to distinguish from one another and also have significant associated errors. It can also be seen that the tracking of the right section of the lower ribbon has caused the algorithm considerable difficulty and the snake results show considerable errors here.

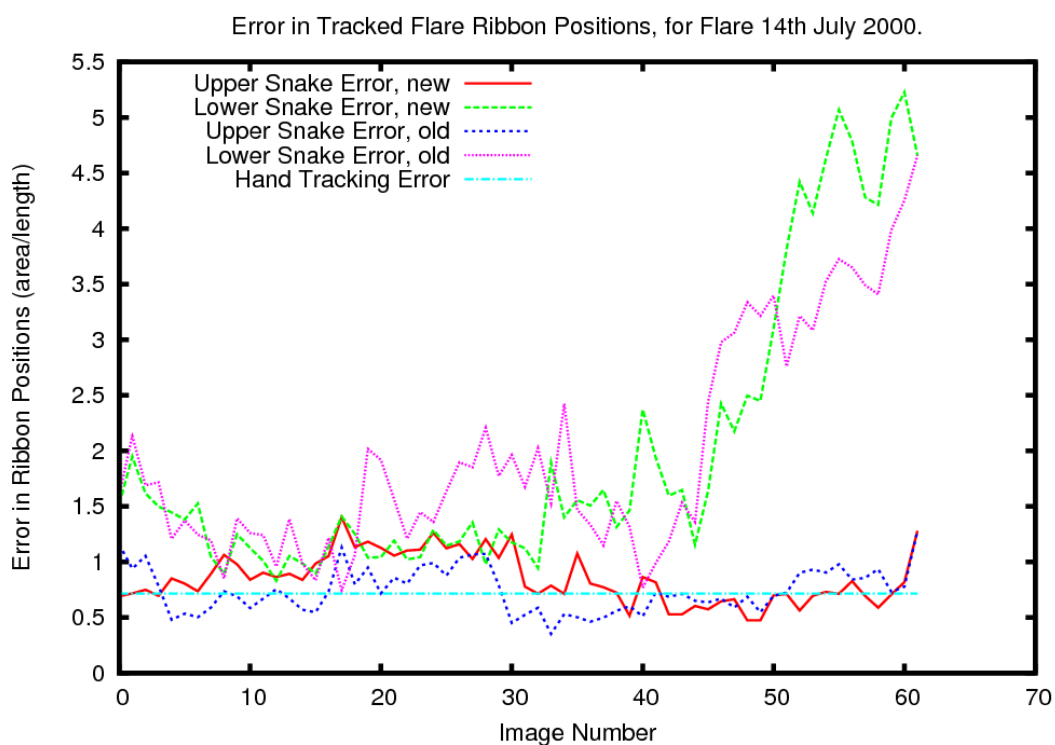
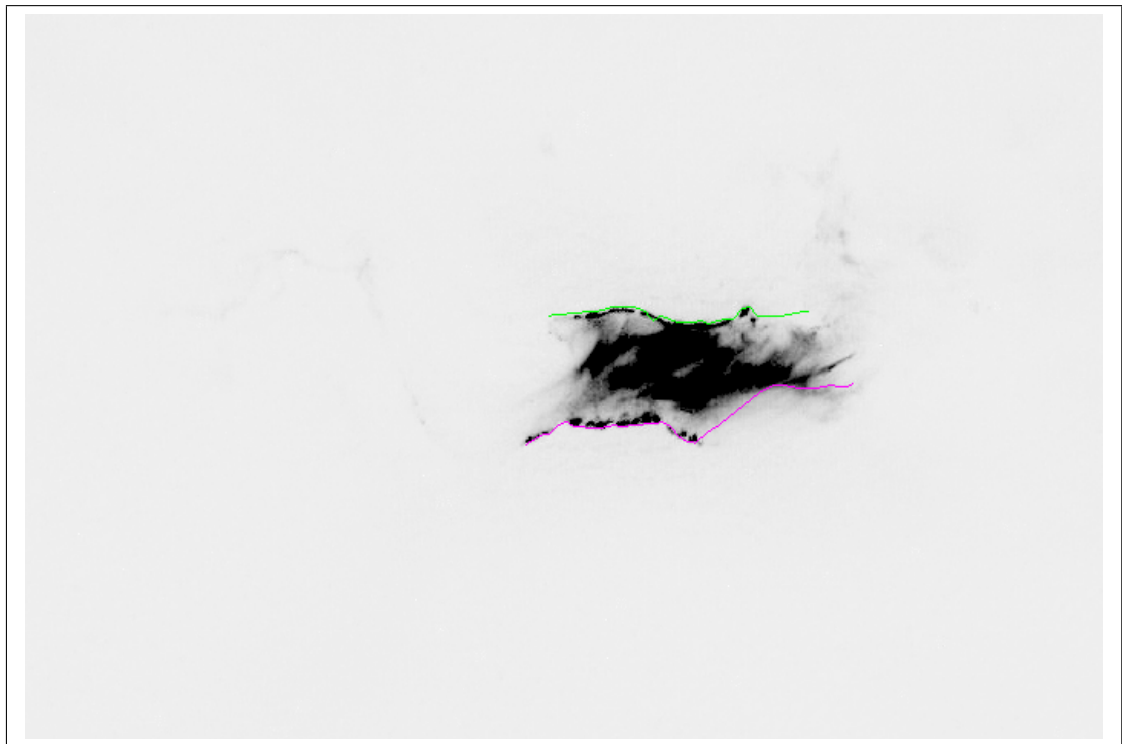
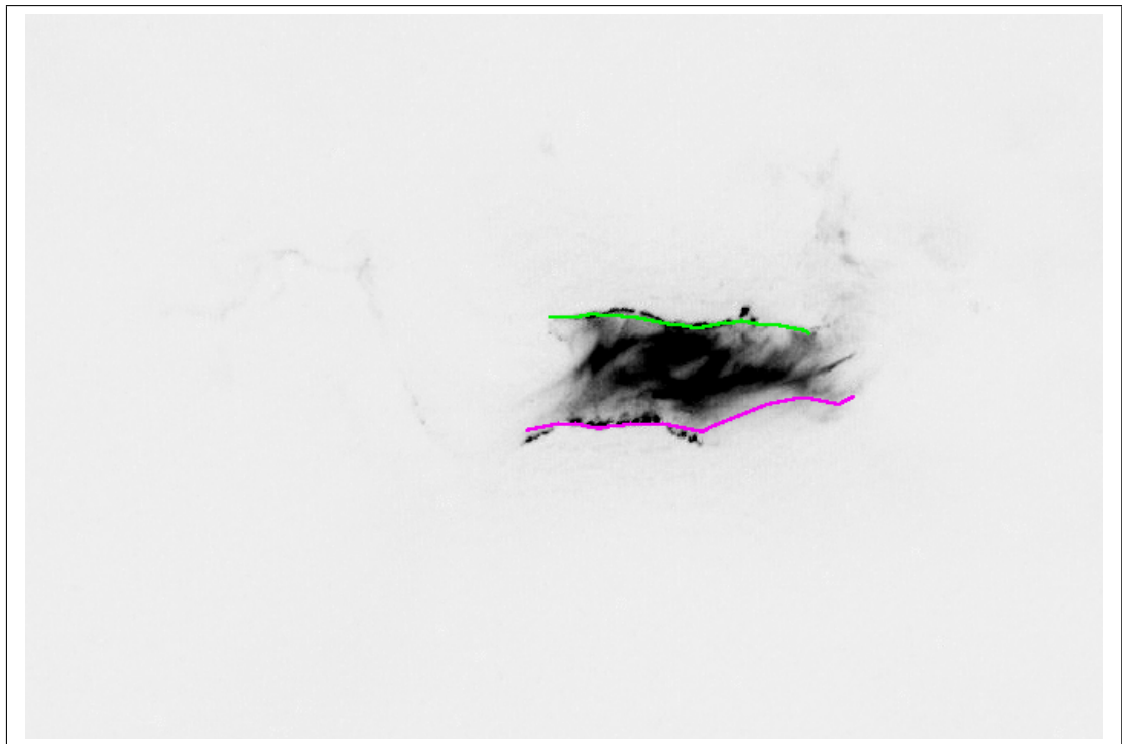


Figure 4.21: Graph showing the error in the upper and lower snake in tracking the upper and lower ribbon, for both the “new” and “standard” methods, for images from the 14th July 2000 flare image sequence.

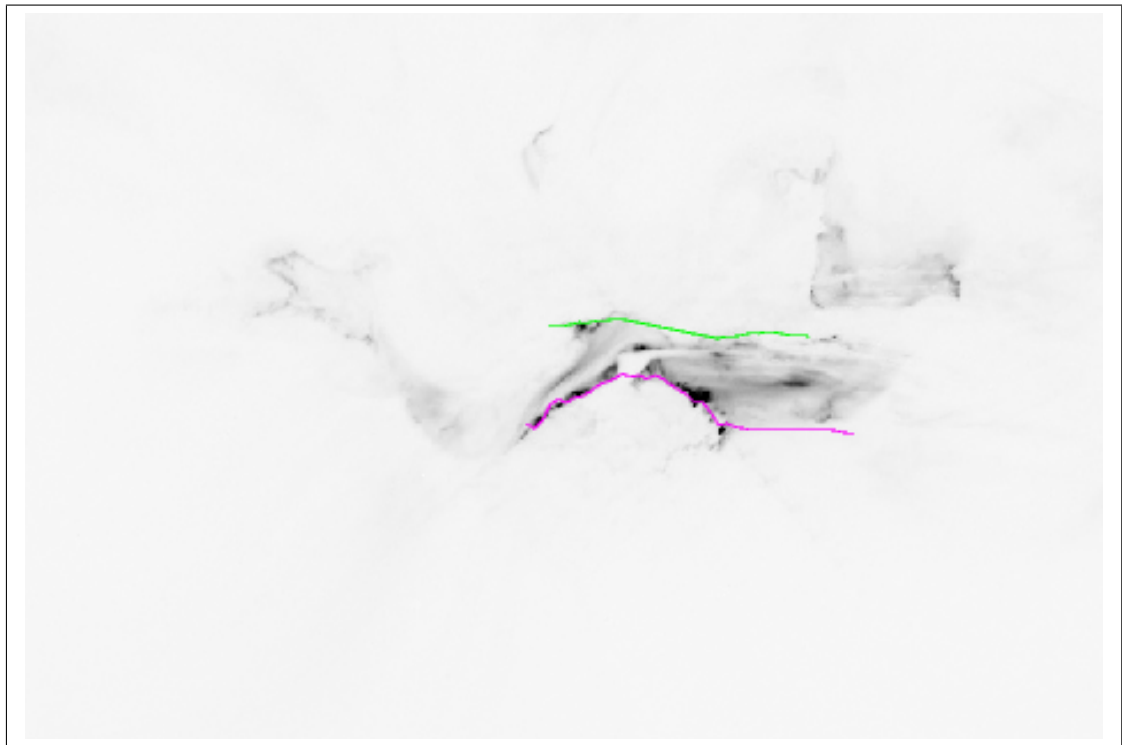


(a)

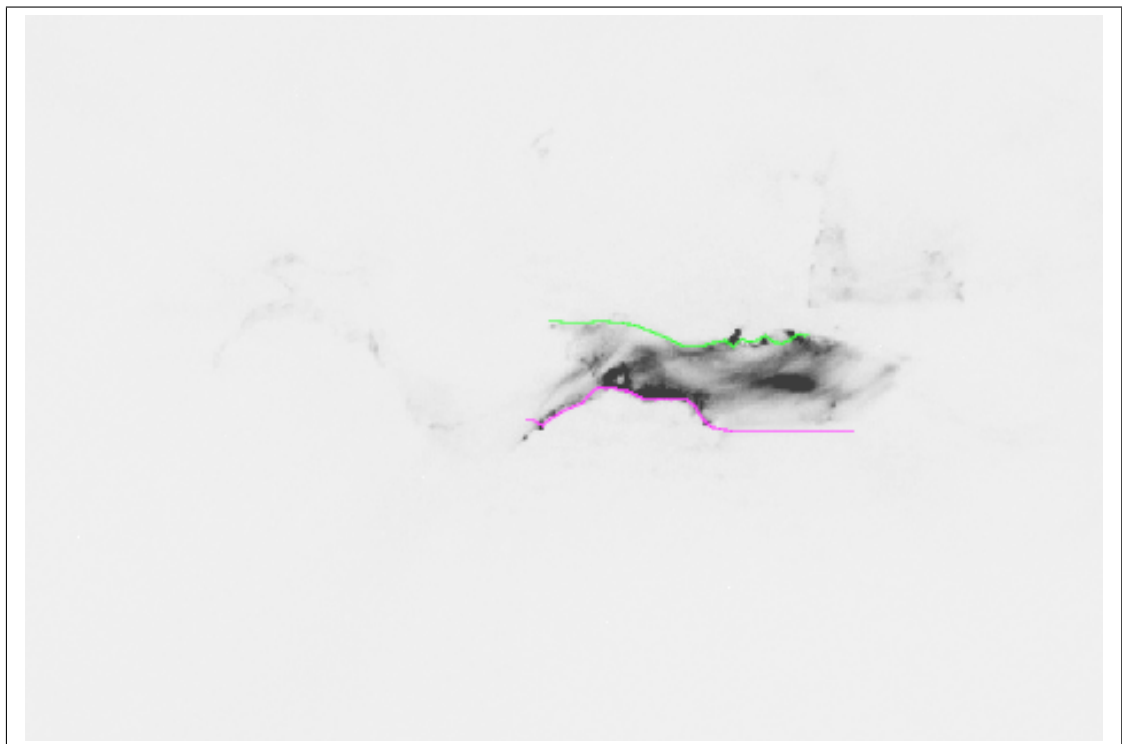


(b)

Figure 4.22: Images showing the tracked ribbon positions for images from the 14th July 2000 flare. Image (a) uses the “standard” method for edge image production, and image (b) uses the “new” method for edge image production.

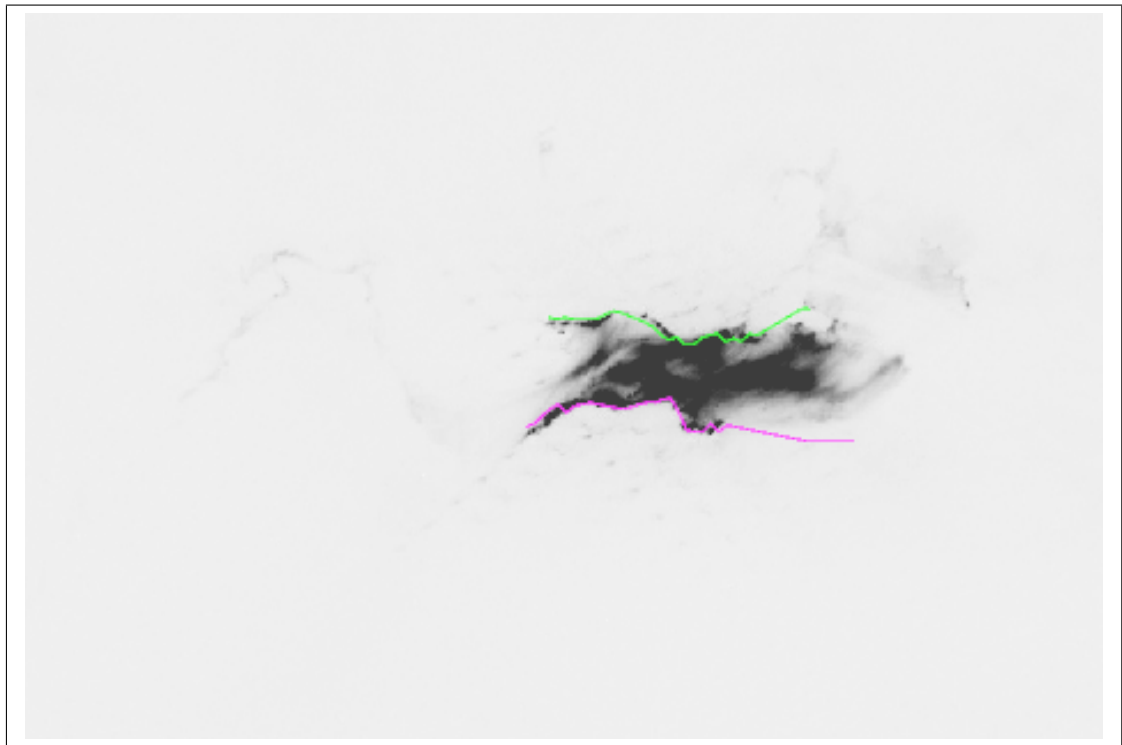


(a)

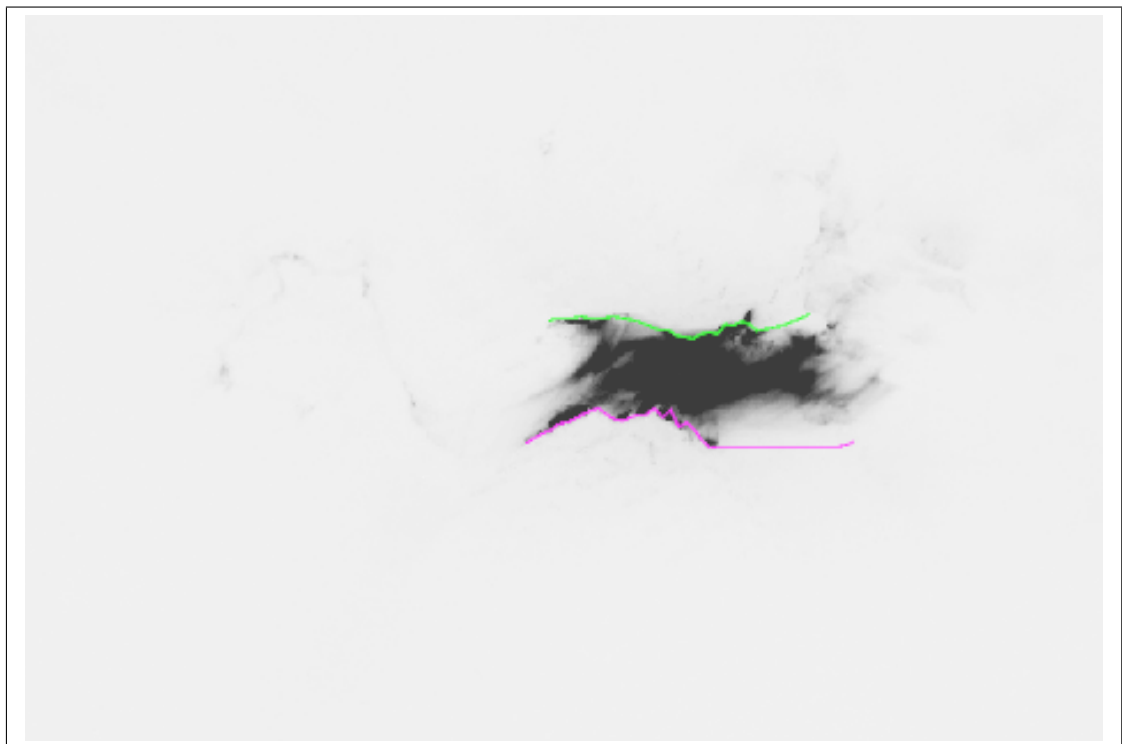


(b)

Figure 4.23: Images showing the tracked ribbon positions for images from the 14th July 2000 flare. Image (a) no. 000, (b) no. 010. The parameters used for these results are: upper snake - cont = 1.0, curv = 1.0, pressure = 0.0, grad = 0.250, ints = 0.250; lower snake - cont = 1.0, curv = 1.0, pressure = 0.0, grad = 0.219, ints = 0.219. For both snakes  $\sigma = 3.0$ .

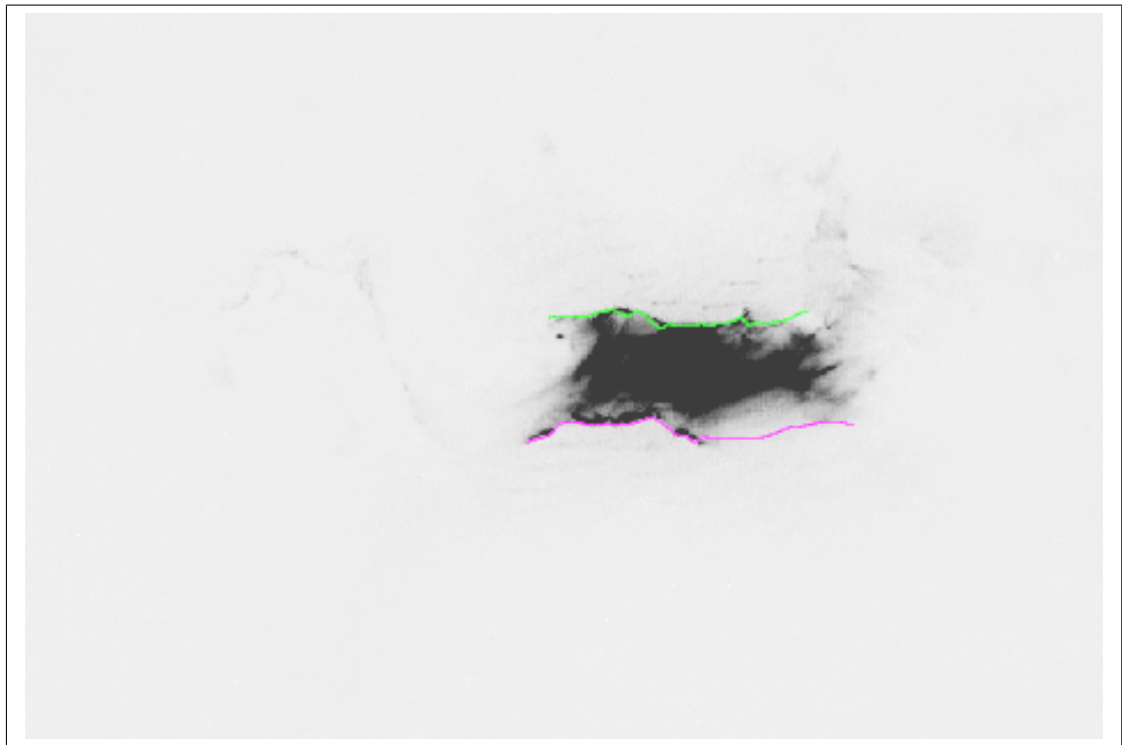


(a)

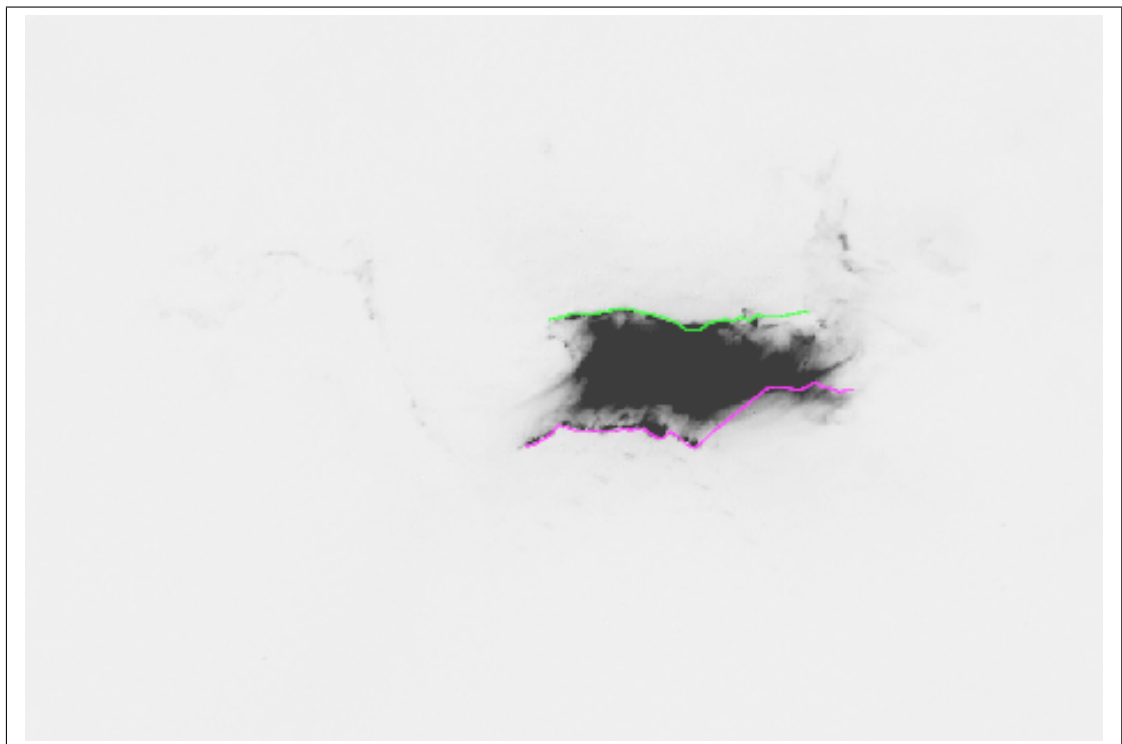


(b)

Figure 4.24: Images showing the tracked ribbon positions for images from the 14th July 2000 flare. Image (a) no. 020, (b) no. 030. The parameters used for these results are: upper snake - cont = 1.0, curv = 1.0, pressure = 0.0, grad = 0.250, ints = 0.250; lower snake - cont = 1.0, curv = 1.0, pressure = 0.0, grad = 0.219, ints = 0.219. For both snakes  $\sigma = 3.0$ .



(a)



(b)

Figure 4.25: Images showing the tracked ribbon positions for images from the 14th July 2000 flare. Image (a) no. 040, (b) no. 050. The parameters used for these results are: upper snake - cont = 1.0, curv = 1.0, pressure = 0.0, grad = 0.250, ints = 0.250; lower snake - cont = 1.0, curv = 1.0, pressure = 0.0, grad = 0.219, ints = 0.219. For both snakes  $\sigma = 3.0$ .

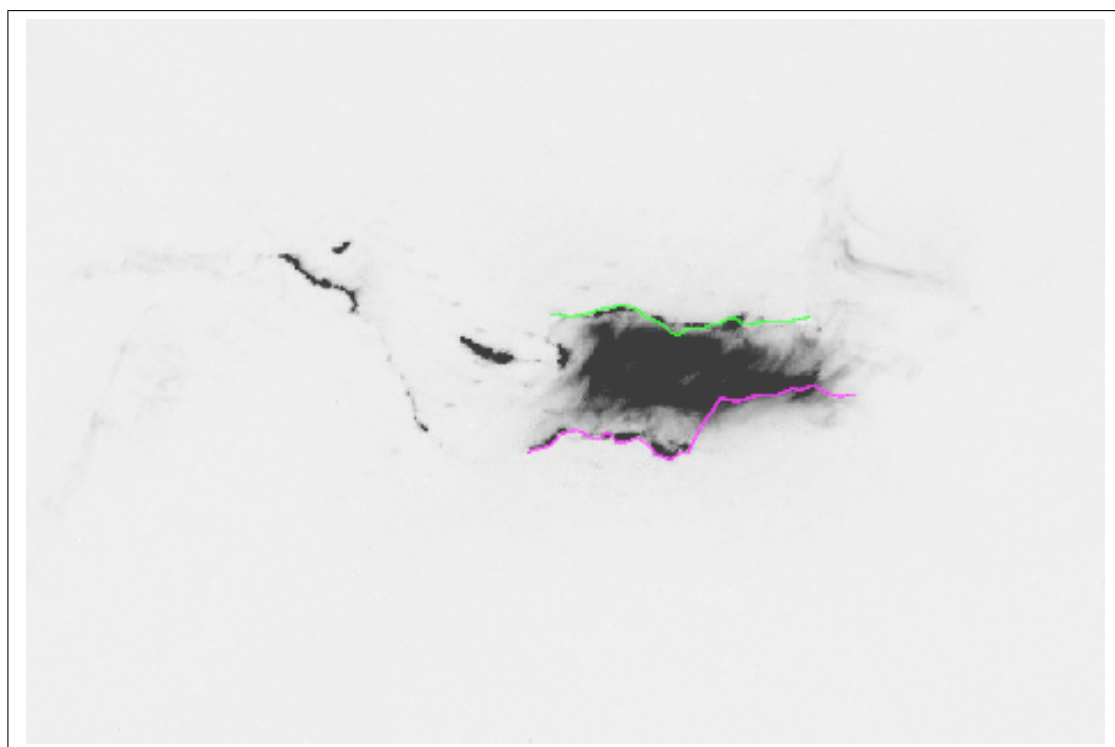


Figure 4.26: Image showing the tracked ribbon positions for image no. 060, from the 14th July 2000 flare. The parameters used for these results are: upper snake - cont = 1.0, curv = 1.0, pressure = 0.0, grad = 0.250, ints = 0.250; lower snake - cont = 1.0, curv = 1.0, pressure = 0.0, grad = 0.219, ints = 0.219. For both snakes  $\sigma = 3.0$ .

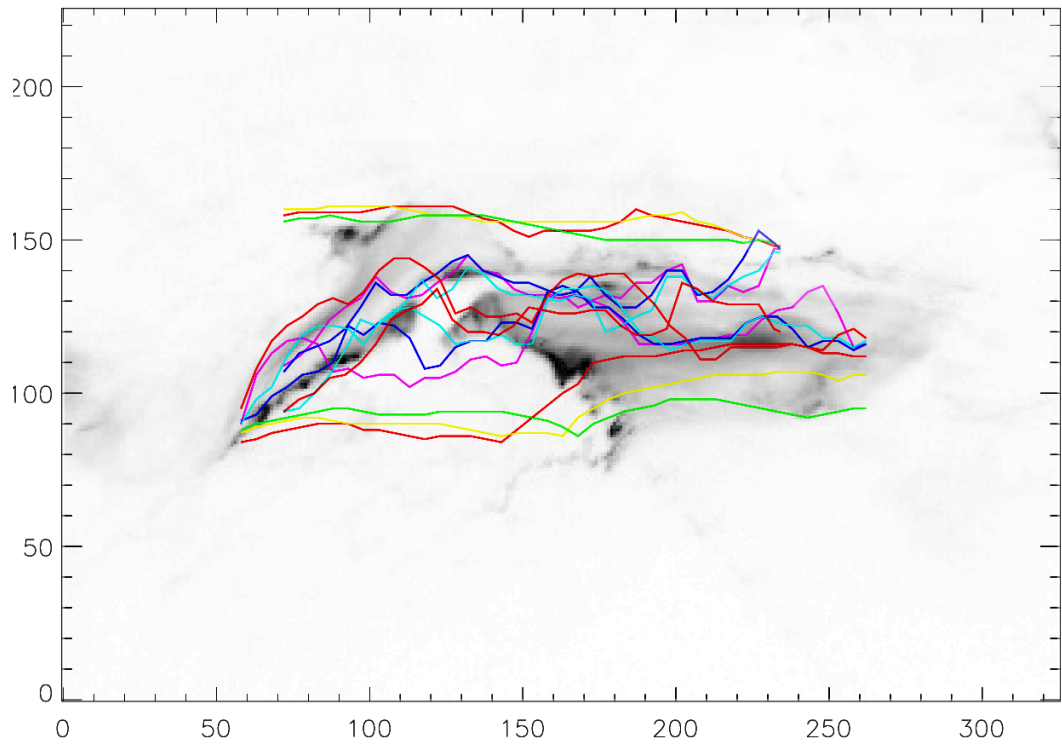


Figure 4.27: The first image of the 14th July 2000 flare sequence, with the tracked ribbon positions for images numbered 0, 10, 20, 30, 40, 50 and 60 shown in red, cyan, blue, pink, green, yellow and red respectively. The red line closest to the outside of the image is from image number 60. The parameters used for these results are: upper snake - cont = 1.0, curv = 1.0, pressure = 0.0, grad = 0.250, ints = 0.250; lower snake - cont = 1.0, curv = 1.0, pressure = 0.0, grad = 0.219, ints = 0.219. For both snakes  $\sigma = 3.0$ .

### 4.4.3 Flare 10th April 2001, 04:46 - 06:01, X2.3, 1600 Å

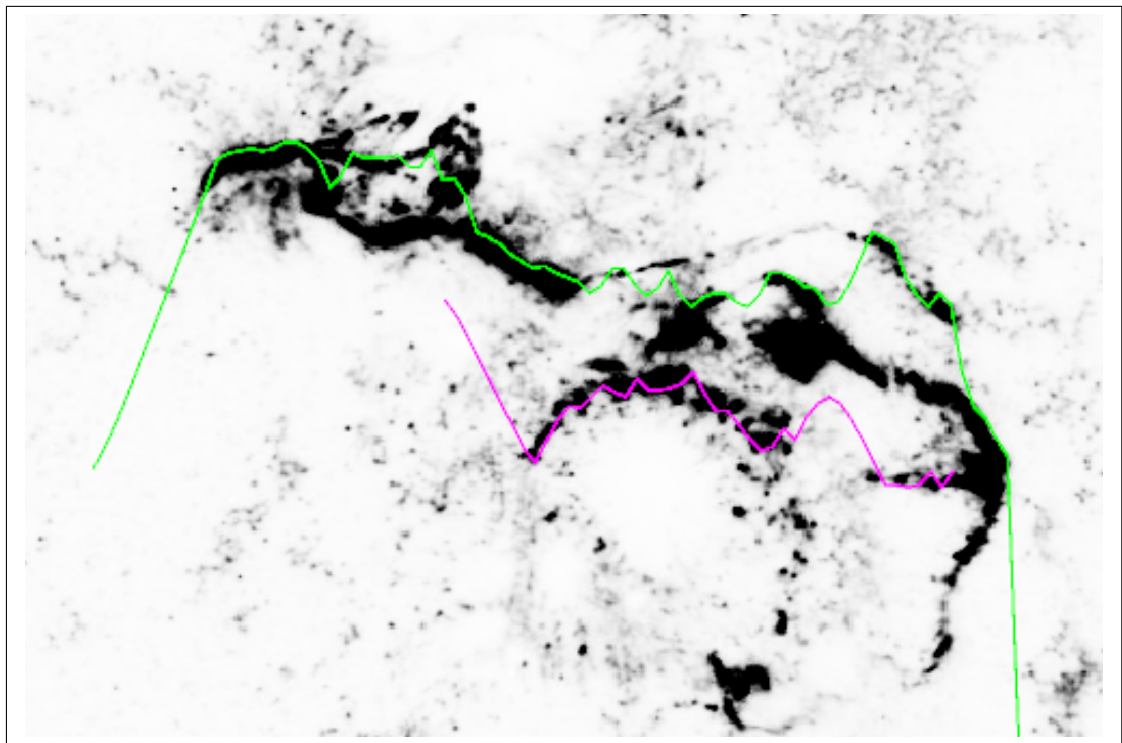
The results of the snake algorithm for tracking the flare ribbon in the 10th April 2001 flare are shown in Figures 4.29 to 4.31. Qualitatively the algorithm appears to perform well. Despite the complicated structure of the ribbons the snakes appear to lie close to the ribbons through all the images. There is large section of the lower ribbon (at coordinates 400, 200 to 400, 270 in Figure 4.29 (b)) that does not appear in the last image of the sequence, but does appear in the far right of the other images in the sequence. As this section of ribbon is particularly large, the 5 pixel shift of the snake starting position between images is not sufficient for the snake to move back over and then find its outer edge. This results in a large error for the lower snake and highlights a disadvantage of using the result from one image as the starting point of another. As this section shrinks over time the error in the lower ribbon decreases accordingly. Where this section of the ribbon is at its smallest the error for the lower snake is at its lowest, i.e. in the first image and in the last image. The error for the upper snake appears high for all the images of this flare, despite appearing qualitatively to give a good fit to the ribbon. This is perhaps due to the large value of the LoG  $\sigma$  parameter used in these images, as the edges of the ribbons have lost some of their detail in the edge image.

Again the snake result from the first image highlights the issue of truncating the snake correctly, the result looks poor due to the difference in lengths of the snakes and the ribbons. Although the snake length is allowed to change in the algorithm, the changes in the snake length do not happen quickly enough to keep pace with changes in the ribbon length, particularly in the early images of the flare, where the ribbons change in length dramatically.

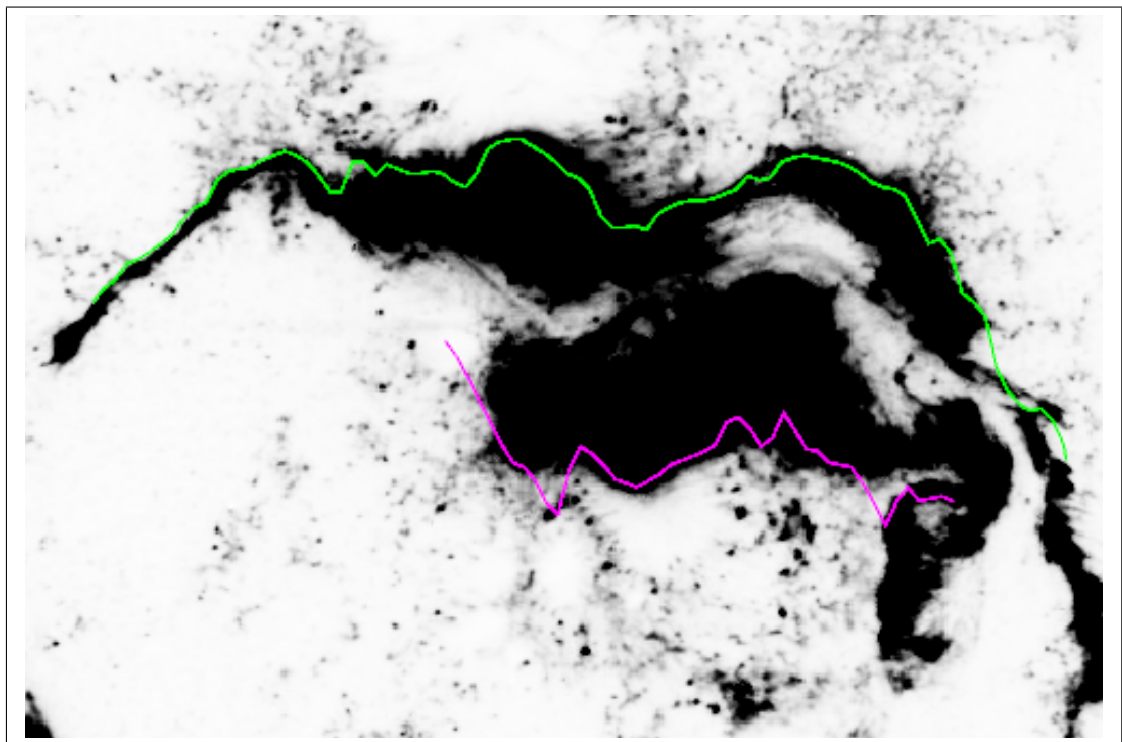
The snake tracking results are summarised on the first image of the sequence in Figure 4.32. In this image it is possible to observe a spreading of the ribbons and a slight smoothing out of the upper ribbon with time, as represented by the snake tracking results.



Figure 4.28: Graph showing the error in the upper and lower snake in tracking the upper and lower ribbon for images from the 10th April 2001 flare image sequence. The parameters used for these results are: upper snake - cont = 1.0, curv = 0.10, pressure = 0.0, grad = 0.08, ints = 0.0; lower snake - cont = 1.0, curv = 0.4, pressure = 7.0, grad = 1.20, ints = 0.0. For both snakes  $\sigma = 3.0$ .

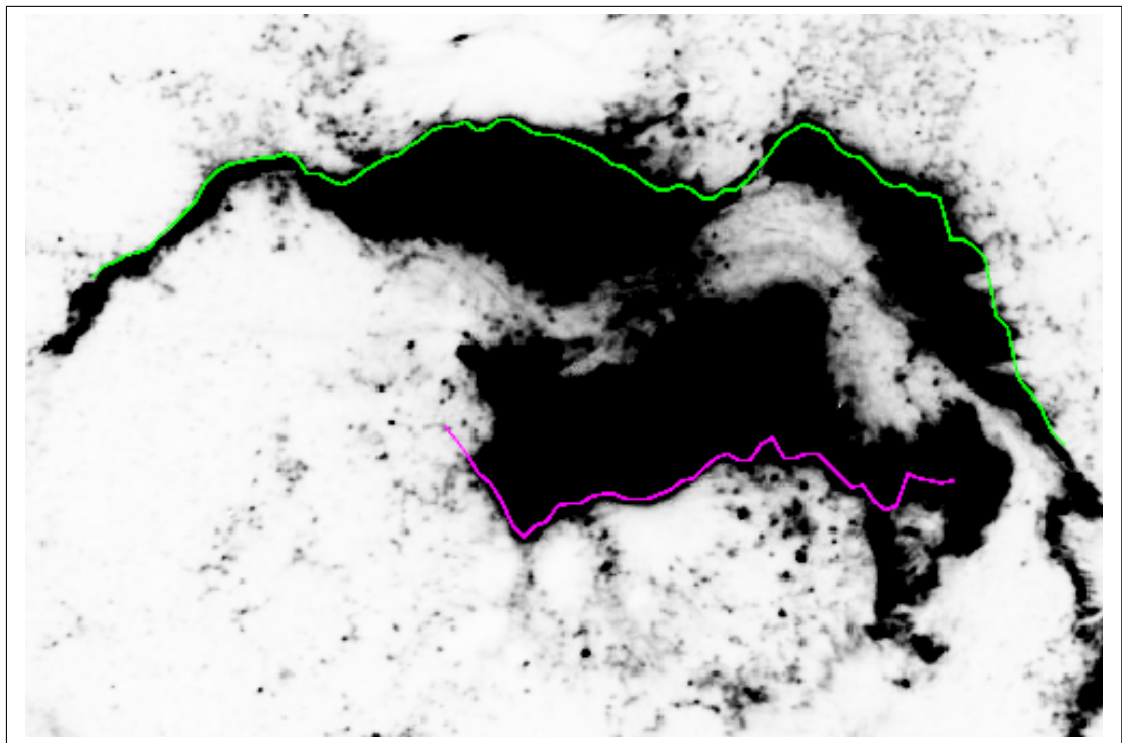


(a)

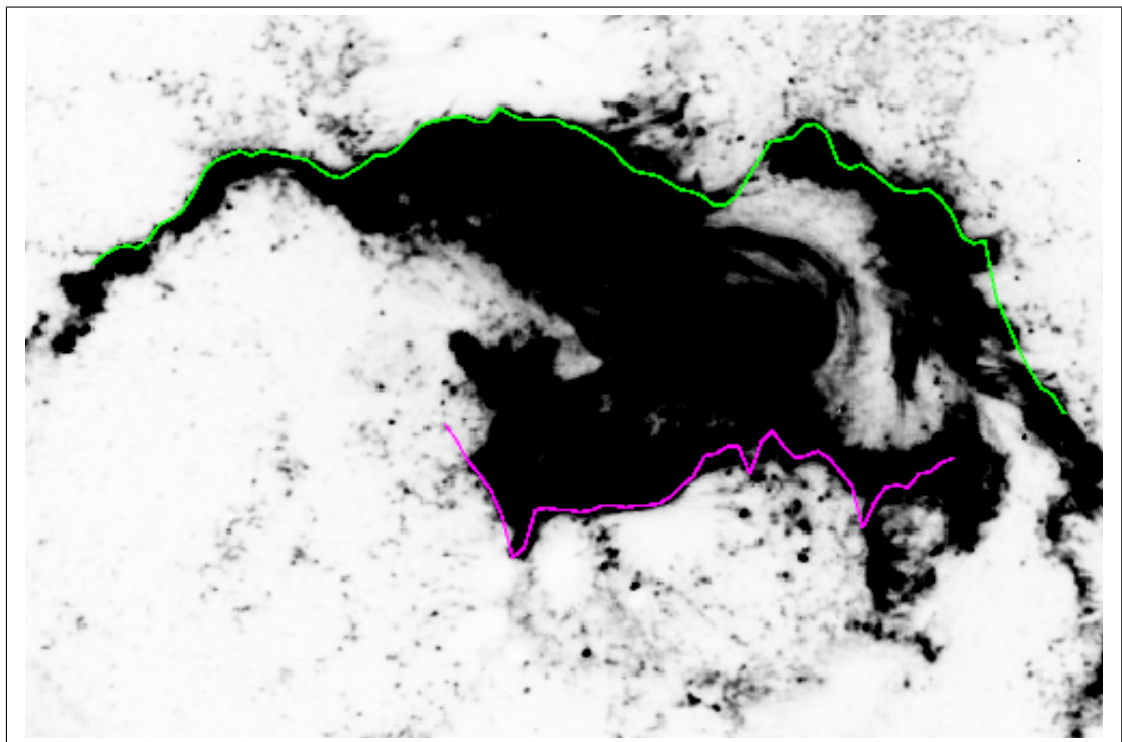


(b)

Figure 4.29: Images showing the tracked ribbon positions for images from the 10th April 2001 flare. Image (a) no. 000, (b) no. 001. The parameters used for these results are: upper snake - cont = 1.0, curv = 0.10, pressure = 0.0, grad = 0.08, ints = 0.0; lower snake - cont = 1.0, curv = 0.4, pressure = 7.0, grad = 1.20, ints = 0.0. For both snakes  $\sigma = 3.0$ .



(a)



(b)

Figure 4.30: Images showing the tracked ribbon positions for images from the 10th April 2001 flare. Image (a) no. 002, (b) no. 003. The parameters used for these results are: upper snake - cont = 1.0, curv = 0.10, pressure = 0.0, grad = 0.08, ints = 0.0; lower snake - cont = 1.0, curv = 0.4, pressure = 7.0, grad = 1.20, ints = 0.0. For both snakes  $\sigma = 3.0$ .

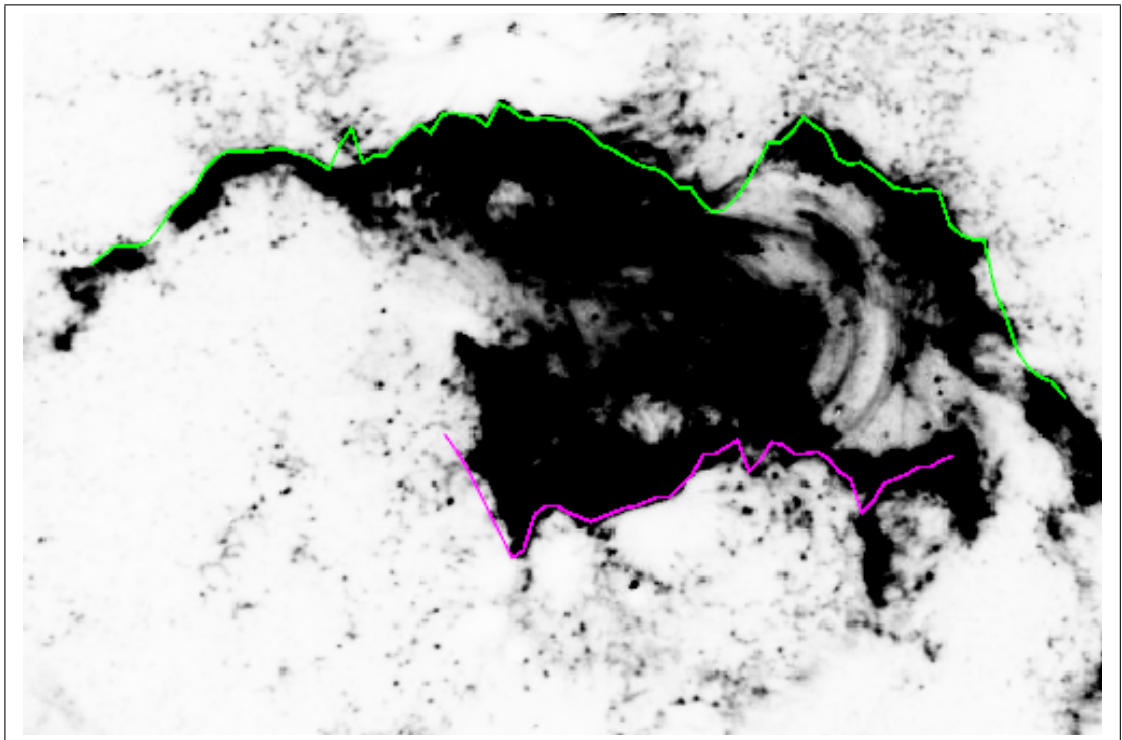


Figure 4.31: Image showing the tracked ribbon positions for image no. 004, from the 10th April 2001 flare.

Image showing the tracked ribbon positions for image no. 004, from the 10th April 2001 flare. The parameters used for these results are: upper snake - cont = 1.0, curv = 0.10, pressure = 0.0, grad = 0.08, ints = 0.0; lower snake - cont = 1.0, curv = 0.4, pressure = 7.0, grad = 1.20, ints = 0.0. For both snakes  $\sigma = 3.0$ .

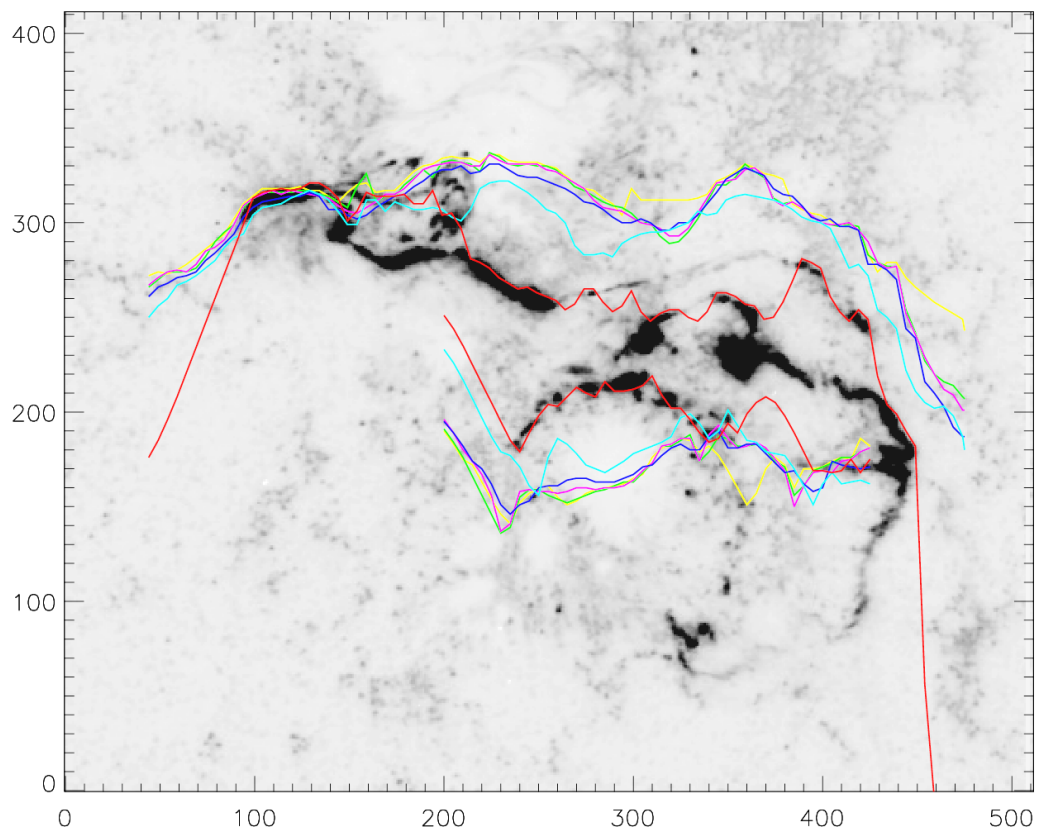


Figure 4.32: The first image of the 10th April 2001 flare sequence, with the tracked ribbon positions for images numbered 0, 1, 2, 3, 4, 5 and 6 shown in red, cyan, blue, pink, green and yellow respectively. The parameters used for these results are: upper snake - cont = 1.0, curv = 0.10, pressure = 0.0, grad = 0.08, ints = 0.0; lower snake - cont = 1.0, curv = 0.4, pressure = 7.0, grad = 1.20, ints = 0.0. For both snakes  $\sigma = 3.0$ .

#### 4.4.4 Flare 25 June 2000, 07:36 - 08:40, M1.9, 1600 Å

The result of the snake algorithm on the image sequence from the 25th June 2000 flare are shown for a selection of images in Figures 4.34 to 4.37. The general fit of the snakes to the ribbons is satisfactory. The snakes track the general shape and position of both ribbons throughout the image sequence, as we have now come to expect. The errors in the snake tracking are shown for each image in graphical format in Figure 4.33. The result is worse than manual methods for accuracy. The snakes generally follow the finer detail of the ribbons. The upper snake finds the lower edge of the far right section of the upper ribbon rather than the upper edge. In image (b) of Figure 4.37, the upper snake can be seen to be held away from the ribbon by a point like feature which is blown up and pointed out in the image. The same feature can be seen in the last image of the sequence in Section 4.3. The error in the lower snake is seen to gradually increase as the image number approaches 0 from a very low error in the last image of the sequence. A large error in the lower snake can be seen in the first image in the sequence, see image (a) of Figure 4.34, where the lower snake has moved past the weak right-most section of the lower ribbon and come to rest on a new feature in the image sequence appearing to be jet material. The error in the upper snake is particularly large in the first 5 images of the sequence: in image (a) and image (b) of Figure 4.34 different sections of the upper ribbon can be clearly seen appearing above the snake, which will add significant contributions to the error for these images. The upper ribbon in later images presents a problem for tracking, as a bright area of emission appears slightly above the main ribbon in its centre, at coordinates (400, 350). In earlier images this area is attached to the main part of the ribbon, but in these later images it is not obvious whether this area should be regarded as the outer edge of the ribbon or not. The upper snake is seen to locate part of this area in images (a) and (b) from Figure 4.37, but not in images (a) and (b) from Figure 4.36. Where there is some ambiguity regarding whether a certain area of emission should be classified as belonging to the ribbon or not, it is likely that the snake algorithm will produce errors compared to a manually traced ribbon position.

Figure 4.38 shows the snake tracking results from a number of different images in the sequence overlaid onto the first image in the sequence for this flare. This image shows the separation of the ribbons over time and in the lower ribbon it is also possible to see a simplification in the structure of the ribbon with passing time.

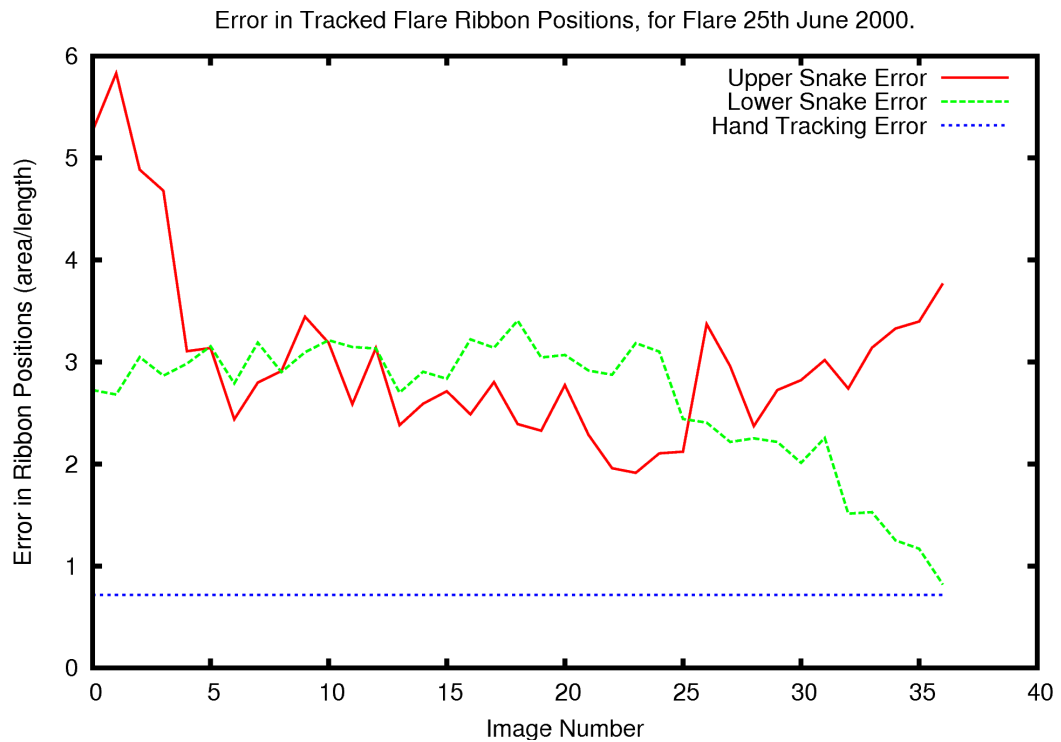
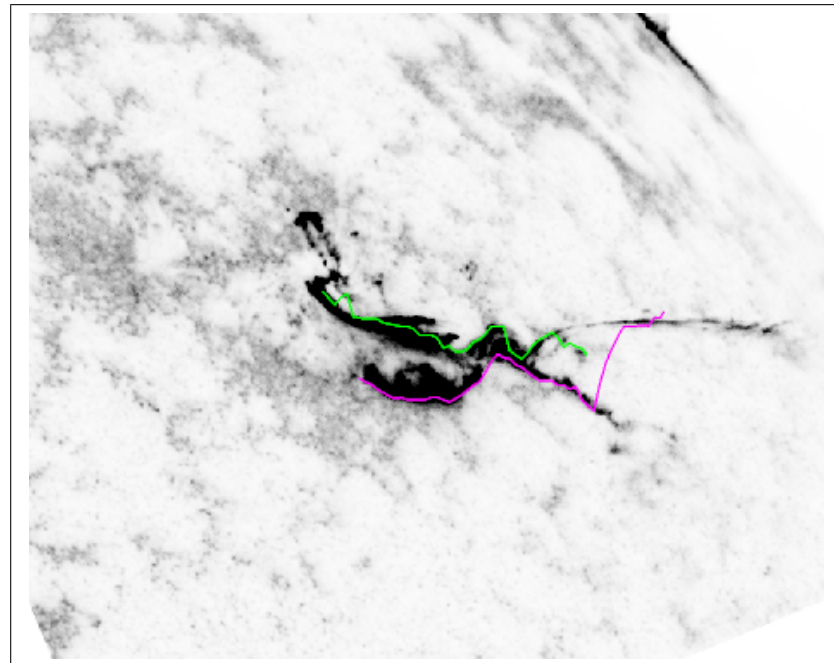
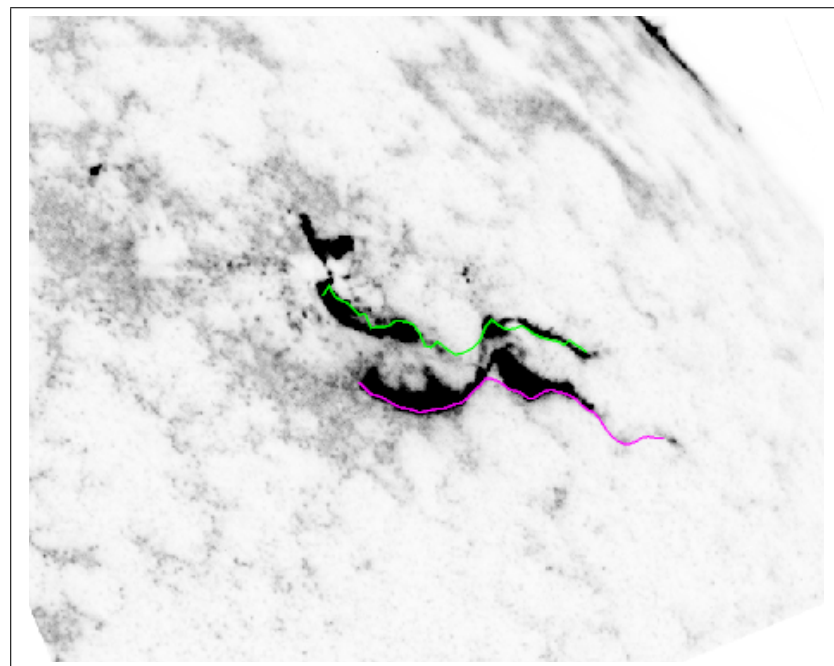


Figure 4.33: Graph showing the error in the upper and lower snake in tracking the upper and lower ribbon for images from the 25th June 2000 flare image sequence. The parameters used for these results are: upper snake - cont = 1.0, curv = 0.80, pressure = 18.0, grad = 16.0, ints = 1.0; lower snake - cont = 1.0, curv = 3.0, pressure = 0.0, grad = 0.156, ints = 0.0. For both snakes  $\sigma = 3.0$ .

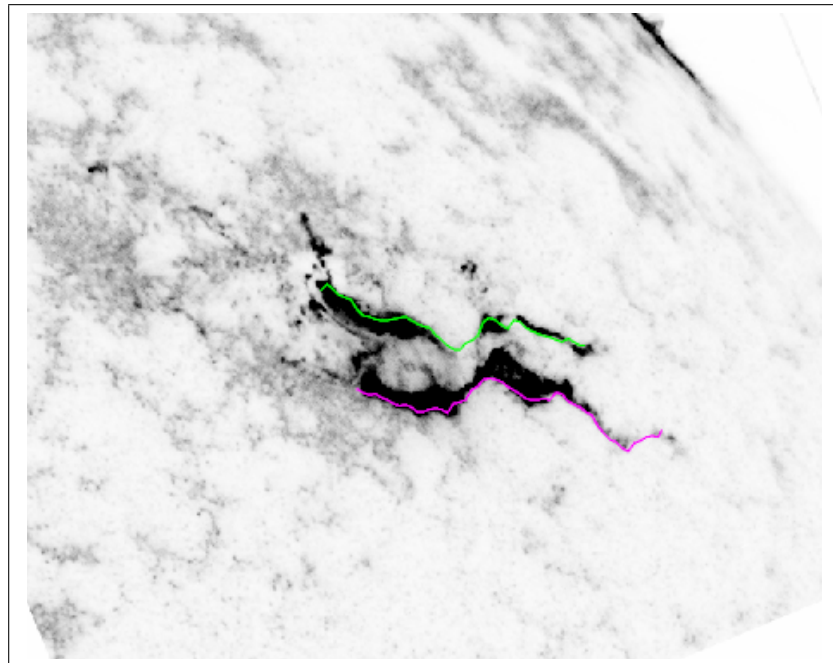


(a)

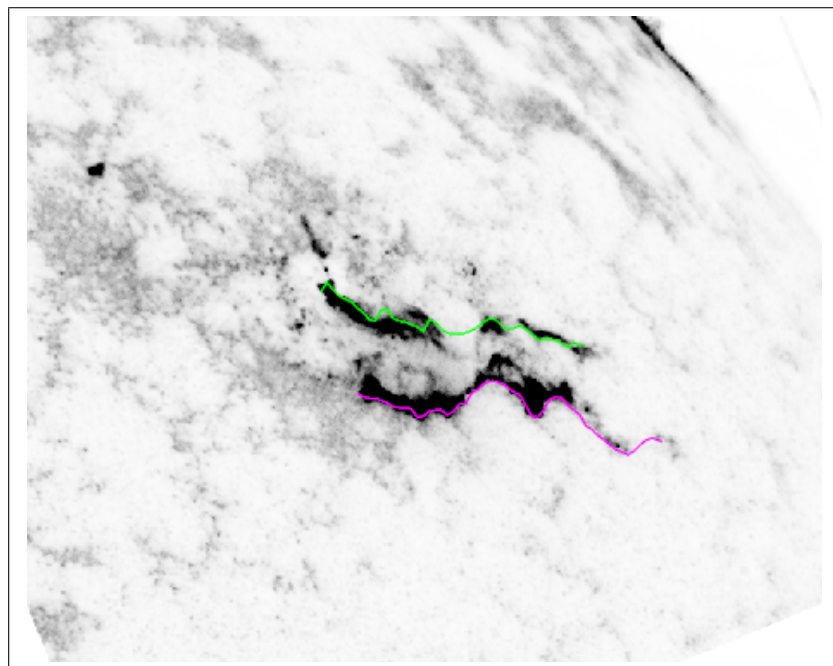


(b)

Figure 4.34: Images showing the tracked ribbon positions for images from the 25th June 2000 flare. Image (a) no. 000, (b) no. 005. The parameters used for these results are: upper snake - cont = 1.0, curv = 0.80, pressure = 18.0, grad = 16.0, ints = 1.0; lower snake - cont = 1.0, curv = 3.0, pressure = 0.0, grad = 0.156, ints = 0.0. For both snakes  $\sigma = 3.0$ .

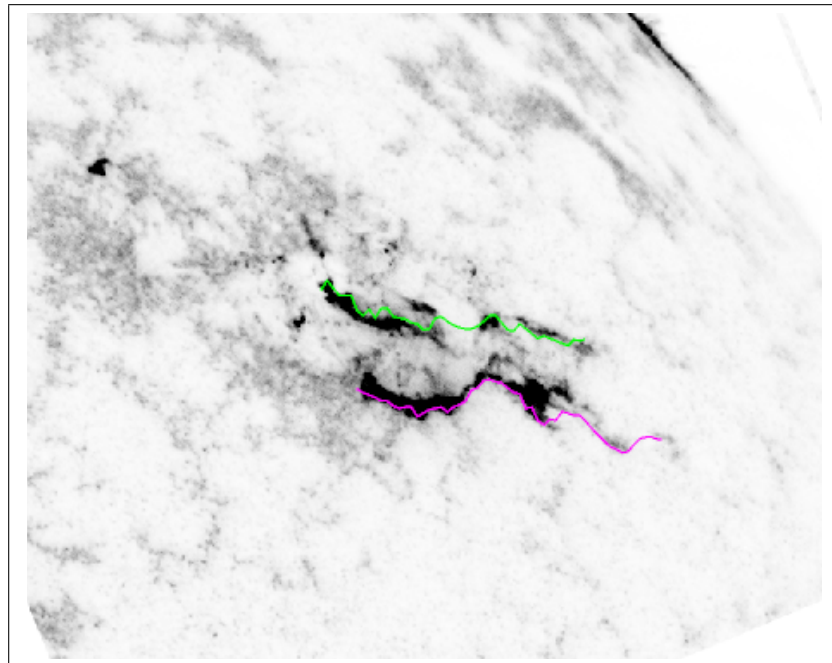


(a)

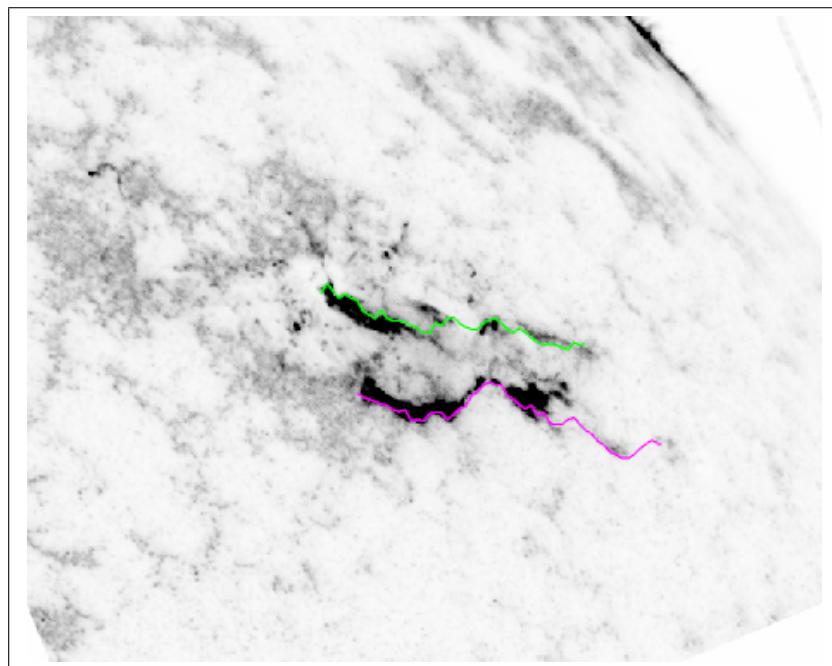


(b)

Figure 4.35: Images showing the tracked ribbon positions for images from the 25th June 2000 flare. Image (a) no. 010, (b) no. 015. The parameters used for these results are: upper snake - cont = 1.0, curv = 0.80, pressure = 18.0, grad = 16.0, ints = 1.0; lower snake - cont = 1.0, curv = 3.0, pressure = 0.0, grad = 0.156, ints = 0.0. For both snakes  $\sigma = 3.0$ .

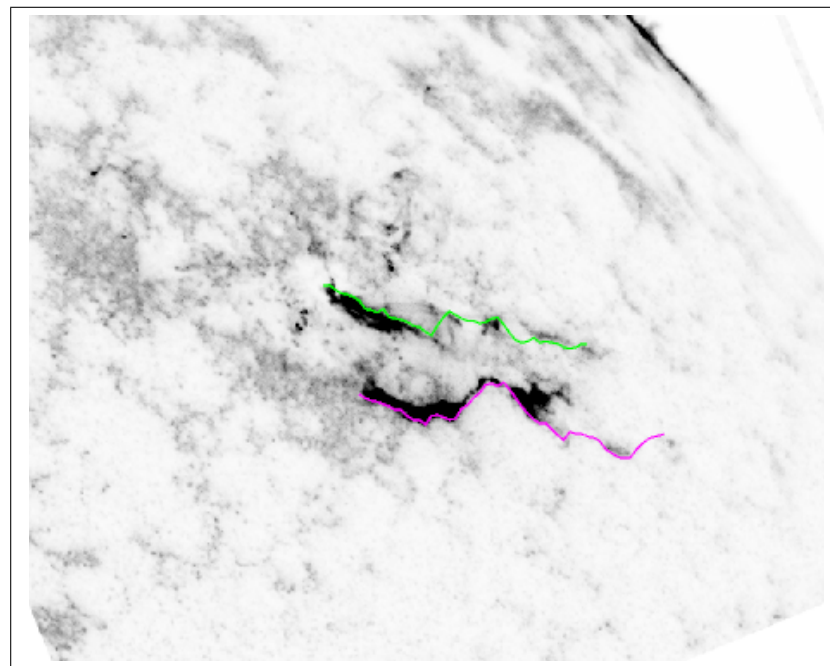


(a)

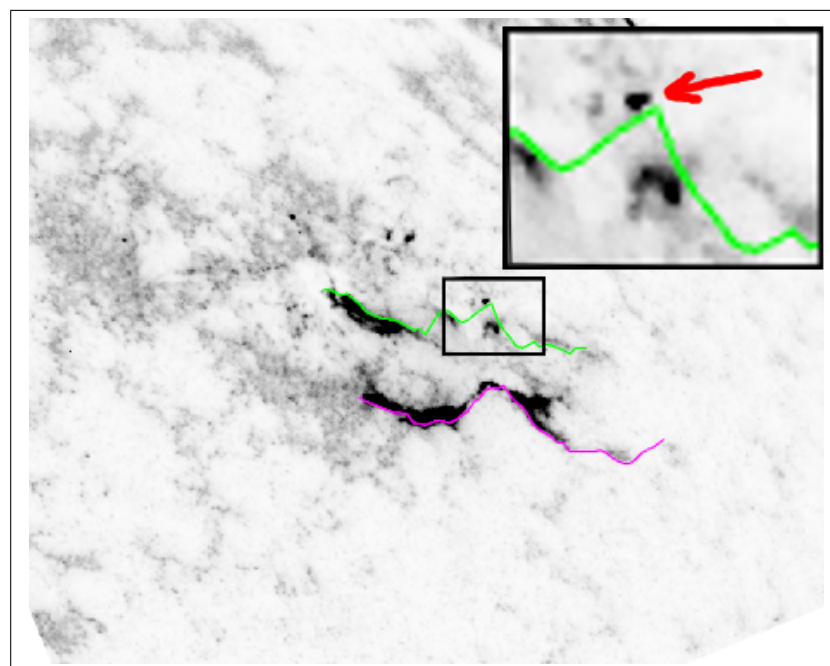


(b)

Figure 4.36: Images showing the tracked ribbon positions for images from the 25th June 2000 flare. Image (a) no. 020, (b) no. 025. The parameters used for these results are: upper snake - cont = 1.0, curv = 0.80, pressure = 18.0, grad = 16.0, ints = 1.0; lower snake - cont = 1.0, curv = 3.0, pressure = 0.0, grad = 0.156, ints = 0.0. For both snakes  $\sigma = 3.0$ .



(a)



(b)

Figure 4.37: Images showing the tracked ribbon positions for images from the 25th June 2000 flare. Image (a) no. 030, (b) no. 035. The inset in image (b) shows how the upper snake is held away from the ribbon by a point-like feature. The parameters used for these results are: upper snake - cont = 1.0, curv = 0.80, pressure = 18.0, grad = 16.0, ints = 1.0; lower snake - cont = 1.0, curv = 3.0, pressure = 0.0, grad = 0.156, ints = 0.0. For both snakes  $\sigma = 3.0$ .

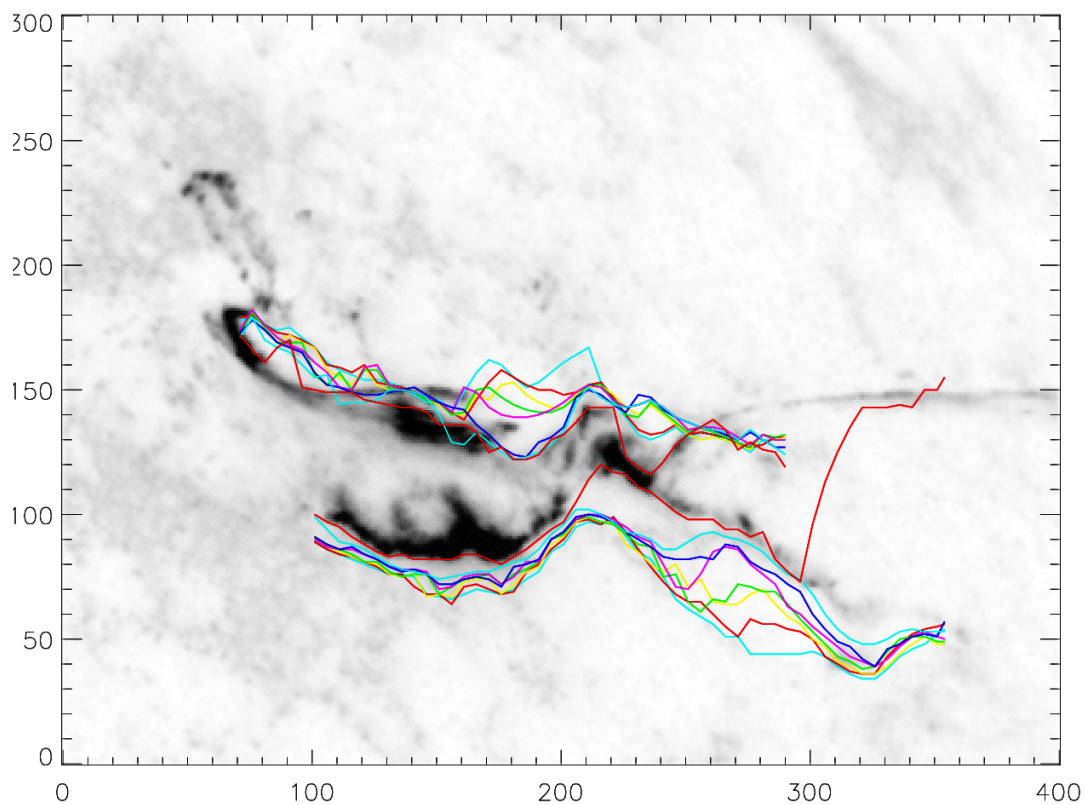


Figure 4.38: The first image of the 25th June 2000 flare sequence, with the tracked ribbon positions for images numbered 0, 5, 10, 15, 20, 25, 30 and 35 shown in red, cyan, blue, pink, green, yellow, red and cyan respectively. The red and cyan lines closest to the outside of the image are from image numbers 30 and 35. The parameters used for these results are: upper snake - cont = 1.0, curv = 0.80, pressure = 18.0, grad = 16.0, ints = 1.0; lower snake - cont = 1.0, curv = 3.0, pressure = 0.0, grad = 0.156, ints = 0.0. For both snakes  $\sigma = 3.0$ .

#### 4.4.5 Flare 12 November 1999, 08:39 - 09:49, M1.7, 1600 Å

The results of the snake algorithm for the image sequence of the 12th November 1999 flare are shown in Figures 4.40 to 4.44, with the snake tracking error for each image in the sequence shown in Figure 4.39. The errors for both snakes are the largest errors, by a considerable amount, of any flare used for testing this algorithm. The upper snake shows a very good fit to the ribbons from around image 53 upwards, with the exception of a few images around image 65, where the error is seen to rise sharply. Image no. 65 is shown in Figure 4.43, where it is possible to observe a smaller secondary part of the ribbon that appears above the main body of the ribbon. The upper snake has become trapped on this secondary part of the ribbon, and this is responsible for the sharp increase in the tracking error over these images. The upper ribbon shows further smaller spikes in its error around images 50, 30 and 10. The increases in error around images 10 and 30 are where the upper snake has passed over the upper ribbon in regions where it appears thin. This can be seen in Figures 4.40 and 4.41. In the areas where the ribbon appears thin, the LoG filter has blurred the ribbon into the background, resulting in the lack of an edge to stop the snakes progress down the image. The increase in error around image 50 is the result of ribbon bifurcation, where the snake tracks the outer secondary part of the ribbon, and the manual tracing of the ribbons tracks the stronger main part of the ribbon. The ribbon bifurcation can be seen in image (b) of Figure 4.42. The overall high error in the lower snake tracking reflects its poor performance throughout the image sequence. The lower ribbon of this flare is particularly contorted and complex, with many different possible interpretations of the leading edge of the lower ribbon. It is also not clear that there is only one lower ribbon, as there are 3 separate main sections of emission, and many areas of emission in front of others. The larger spikes in the lower snake error are associated with areas where the snake tracks one feature, and the manual result tracks another that is either in front of or behind the feature the snake is tracking.

Figure 4.45 shows the snake tracking result from a number of the images in the sequence on the first image for this flare. The snake tracking result for the lower ribbon has considerable errors associated with it and as such there is not much to discern from the lower snake result in this image. The upper snake has smaller associated tracking errors and the usual pattern of ribbon separation is apparent in these results.

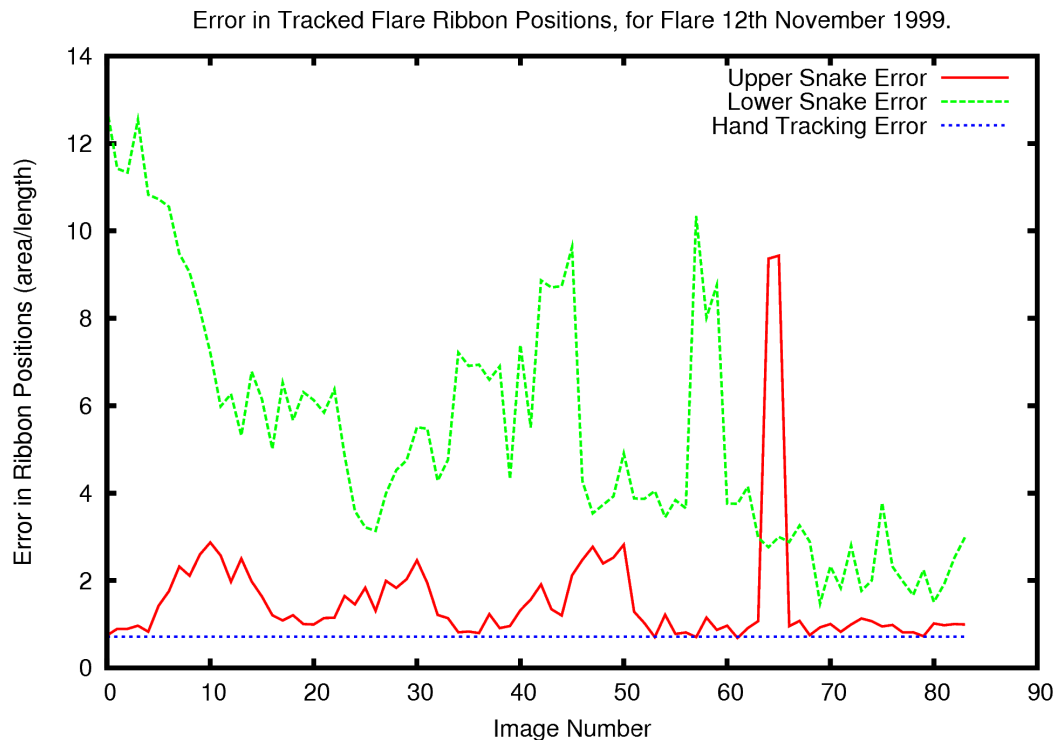
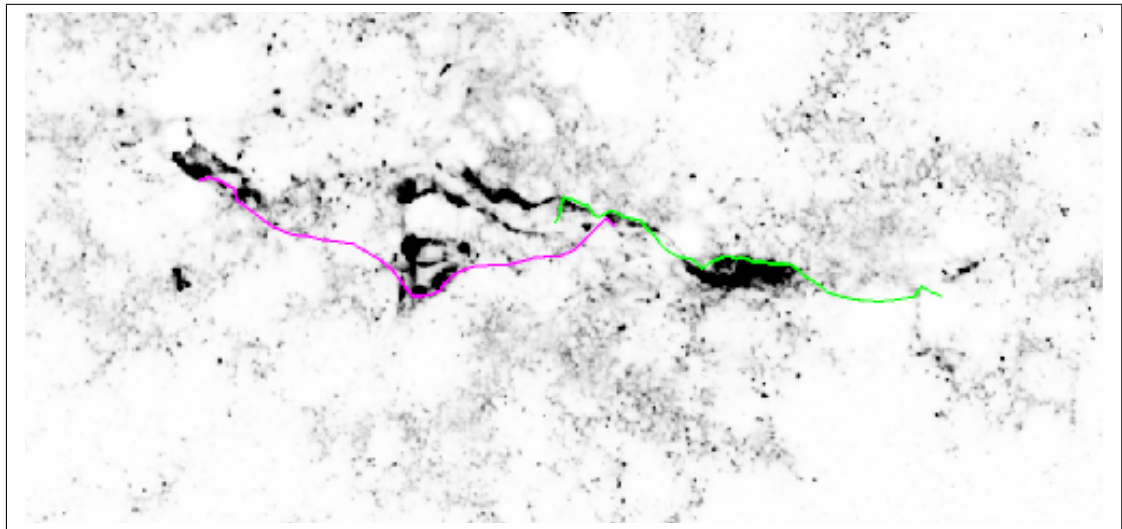
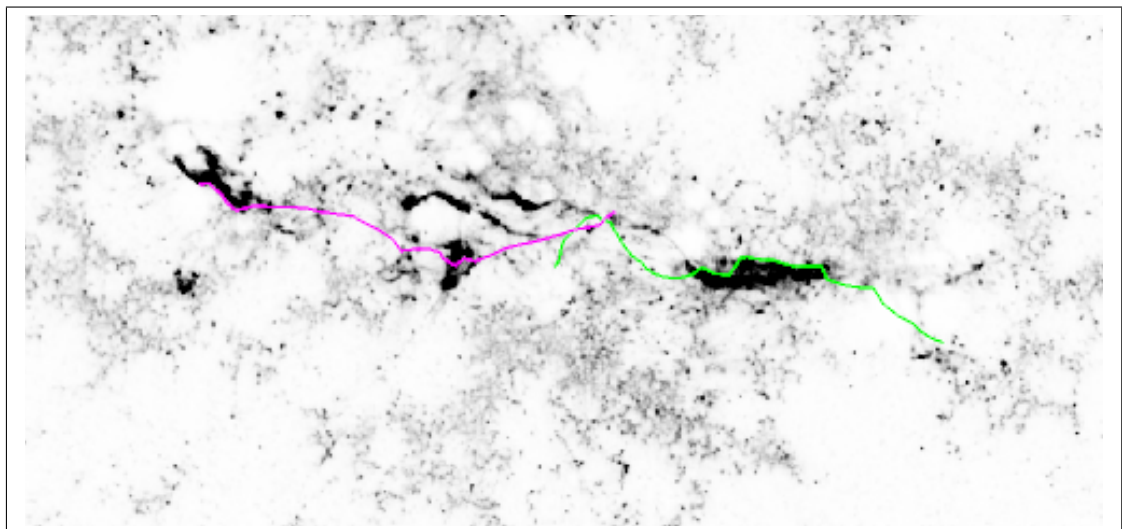


Figure 4.39: Graph showing the error in the upper and lower snake in tracking the upper and lower ribbon for images from the 12th November 1999 flare image sequence. The parameters used for these results are: upper snake - cont = 1.0, curv = 1.0, pressure = 7.14, grad = 2.86, ints = 0.286; lower snake - cont = 1.0, curv = 1.0, pressure = 7.5, grad = 2.5, ints = 0.0. For both snakes  $\sigma = 3.5$ .

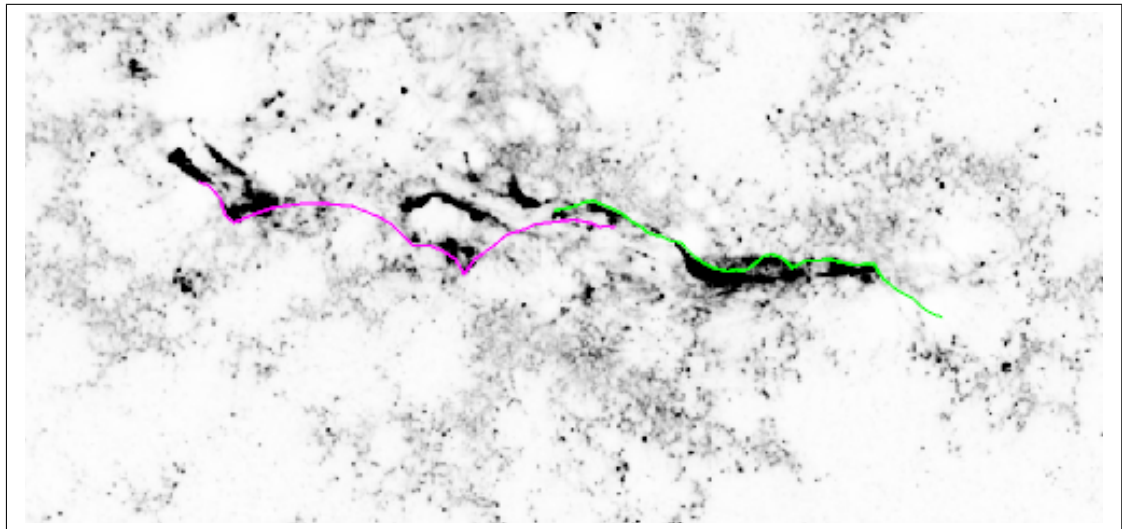


(a)

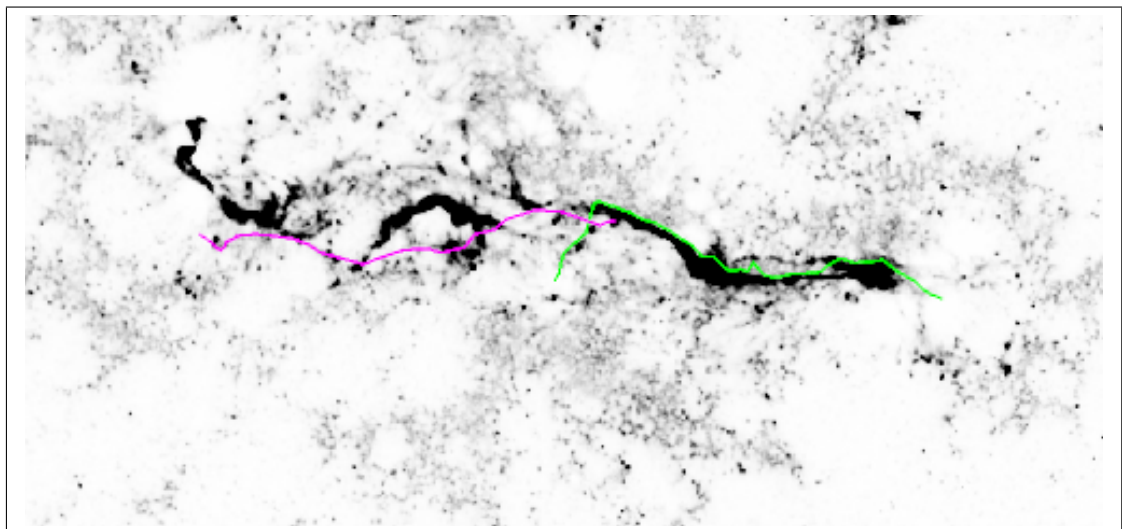


(b)

Figure 4.40: Images showing the tracked ribbon positions for images from the 12th November 1999 flare. Image (a) no. 000, (b) no. 010. The parameters used for these results are: upper snake - cont = 1.0, curv = 1.0, pressure = 7.14, grad = 2.86, ints = 0.286; lower snake - cont = 1.0, curv = 1.0, pressure = 7.5, grad = 2.5, ints = 0.0. For both snakes  $\sigma = 3.5$ .

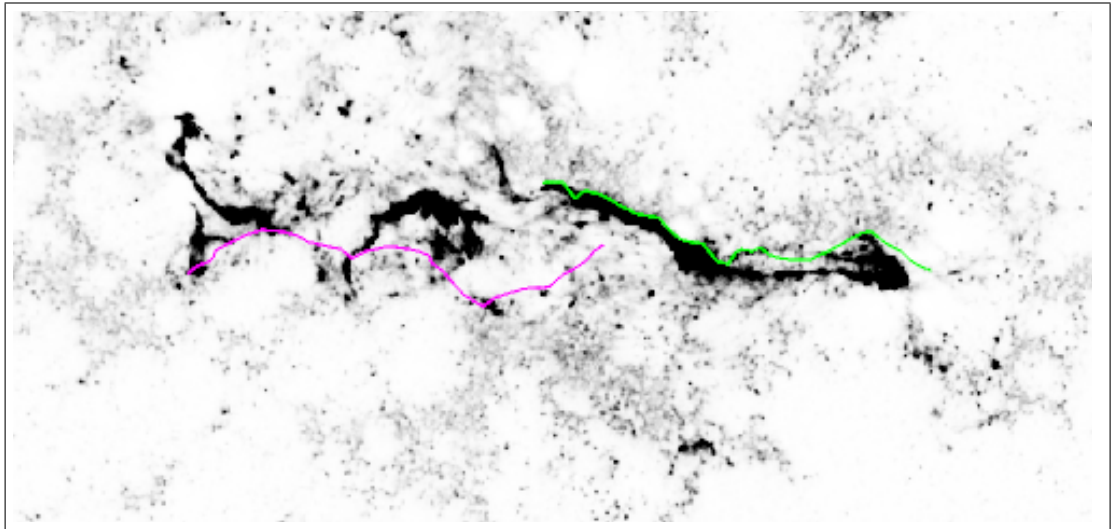


(a)

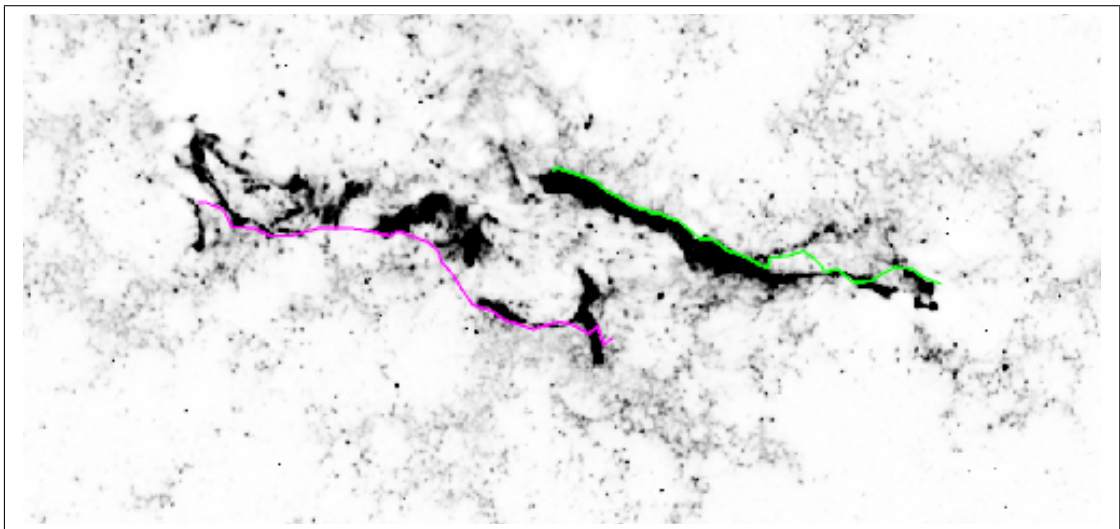


(b)

Figure 4.41: Images showing the tracked ribbon positions for images from the 12th November 1999 flare. Image (a) no. 020, (b) no. 030. The parameters used for these results are: upper snake - cont = 1.0, curv = 1.0, pressure = 7.14, grad = 2.86, ints = 0.286; lower snake - cont = 1.0, curv = 1.0, pressure = 7.5, grad = 2.5, ints = 0.0. For both snakes  $\sigma = 3.5$ .



(a)



(b)

Figure 4.42: Images showing the tracked ribbon positions for images from the 12th November 1999 flare. Image (a) no. 040, (b) no. 050. The parameters used for these results are: upper snake - cont = 1.0, curv = 1.0, pressure = 7.14, grad = 2.86, ints = 0.286; lower snake - cont = 1.0, curv = 1.0, pressure = 7.5, grad = 2.5, ints = 0.0. For both snakes  $\sigma = 3.5$ .

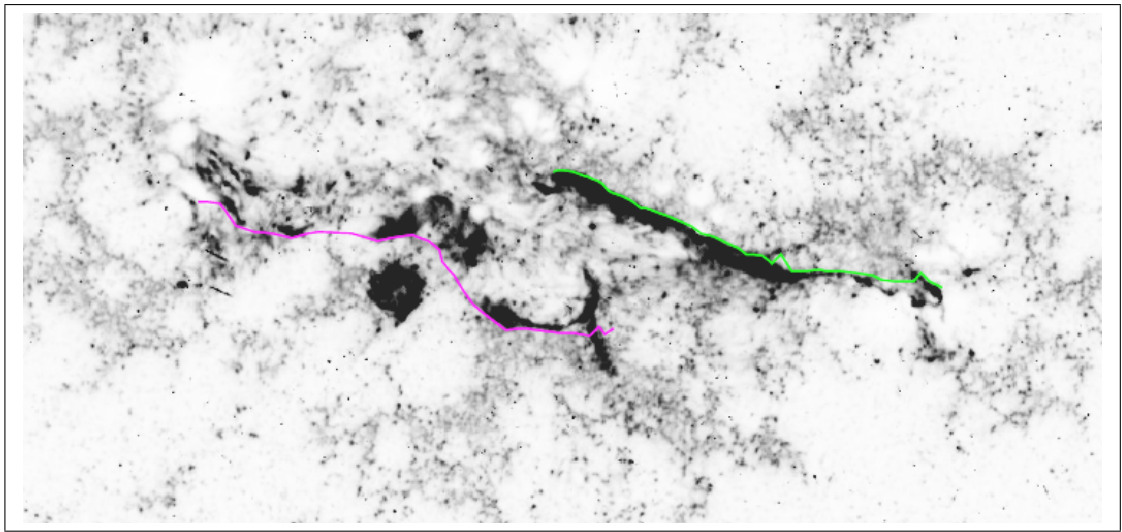
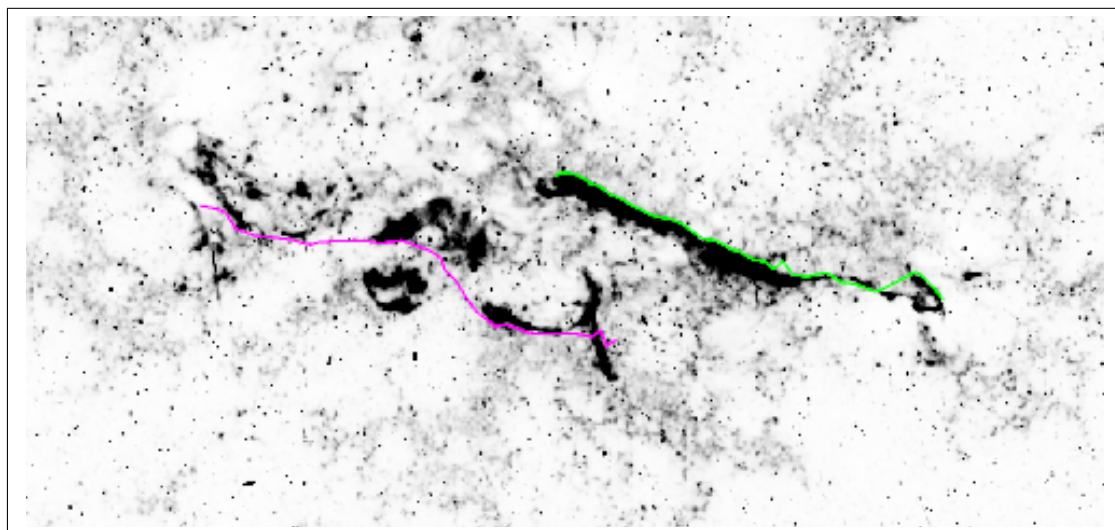
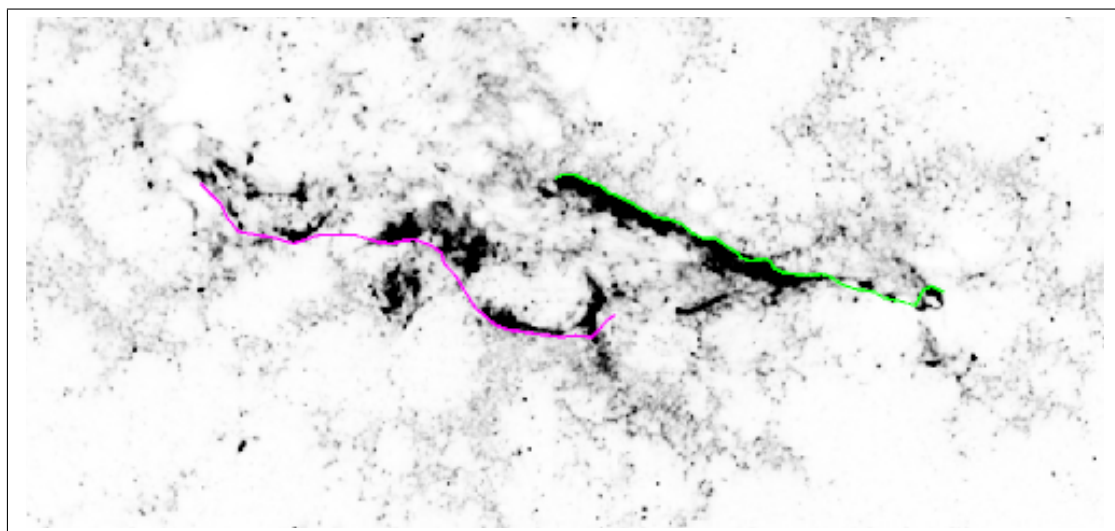


Figure 4.43: Image no. 065 from the 12th November 1999 flare, showing the tracked ribbon positions. The upper snake is shown in green, and the lower snake is shown in red. Part of the upper snake in the central part of the ribbon can be seen to be trapped above the main ribbon by a smaller secondary part of the ribbon forming a peaked shape. The parameters used for these results are: upper snake - cont = 1.0, curv = 1.0, pressure = 7.14, grad = 2.86, ints = 0.286; lower snake - cont = 1.0, curv = 1.0, pressure = 7.5, grad = 2.5, ints = 0.0. For both snakes  $\sigma = 3.5$ .



(a)



(b)

Figure 4.44: Images showing the tracked ribbon positions for images from the 12th November 1999 flare. Image (a) no. 060, (b) no. 070. The parameters used for these results are: upper snake - cont = 1.0, curv = 1.0, pressure = 7.14, grad = 2.86, ints = 0.286; lower snake - cont = 1.0, curv = 1.0, pressure = 7.5, grad = 2.5, ints = 0.0. For both snakes  $\sigma = 3.5$ .

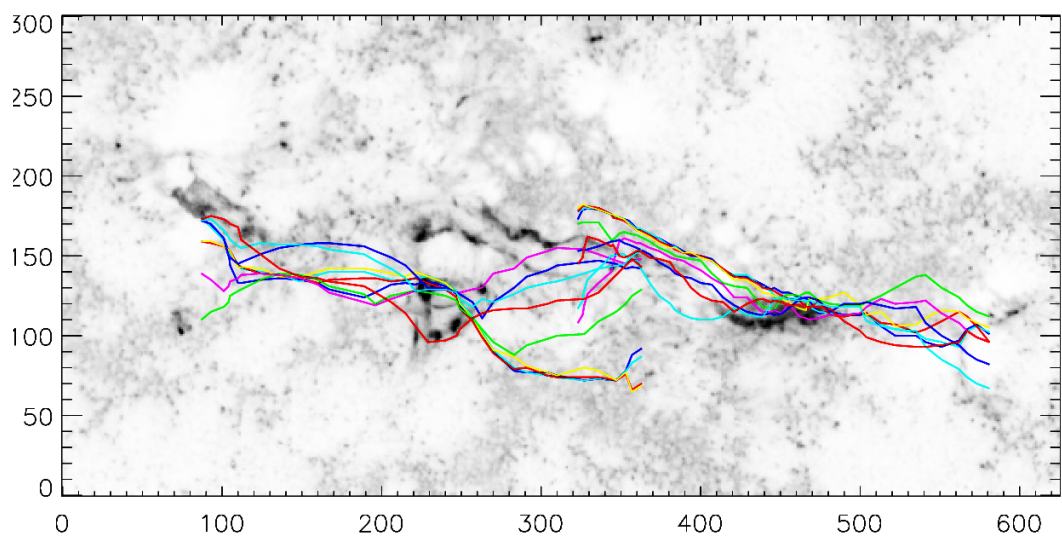


Figure 4.45: The first image of the 12th November 1999 flare sequence, with the tracked ribbon positions for images numbered 0, 10, 20, 30, 40, 50, 60, 70 and 80 shown in cyan, blue, pink, green, yellow, red, cyan and blue respectively. The cyan and blue lines closest to the outside of the image are from image numbers 70 and 80. The parameters used for these results are: upper snake - cont = 1.0, curv = 1.0, pressure = 7.14, grad = 2.86, ints = 0.286; lower snake - cont = 1.0, curv = 1.0, pressure = 7.5, grad = 2.5, ints = 0.0. For both snakes  $\sigma = 3.5$ .

#### 4.4.6 Flare 8th February 2000, 08:33 - 09:37, M1.3, 1600 Å

The final flare used for testing the snake algorithm is the 8th February 2000 flare, the results of the snake tracking are shown in Figures 4.47 to 4.50, with the error in the snake's tracking shown for each image in Figure 4.46. It is important to remember that the algorithm failed to adequately locate the upper ribbon in the last image of the sequence, as discussed in Section 4.3.6. As a result of this the hand tracking result is used as the starting positions for the snakes in image no 35 of this sequence. As the hand traced result consists of more nodes than the snake result, the snakes used for this flare have a higher density of nodes than the snakes used in the other flares. The errors in the snakes remain low for most of the image sequence, and visually the snakes appear to fit the ribbons well. The exception is the last few images in the sequence, i.e. the first few frames of the flare in time, where the tracking error rises sharply. Visual inspection of these images shows most of the lower ribbon seen in the other images is not present, and where there is some evidence of the lower ribbon, it appears very close to the upper ribbon. The upper snake is drawn to the lower ribbon in places, and the lower snake is drawn to the upper ribbon in places, and it is this behaviour that results in the large tracking errors for these first two images in the sequence. It is also possible to see that the snakes in the first image are too long for the ribbons. This remains a problem for the algorithm. Figure 4.51 shows the snake tracking result for a number of the images overlaid onto the first image in the sequence. The usual pattern of ribbon separation is clearly represented, and the lower snake result is seen to straighten out over time also. The upper snake is seen to follow a part of the network visible in this earlier image.

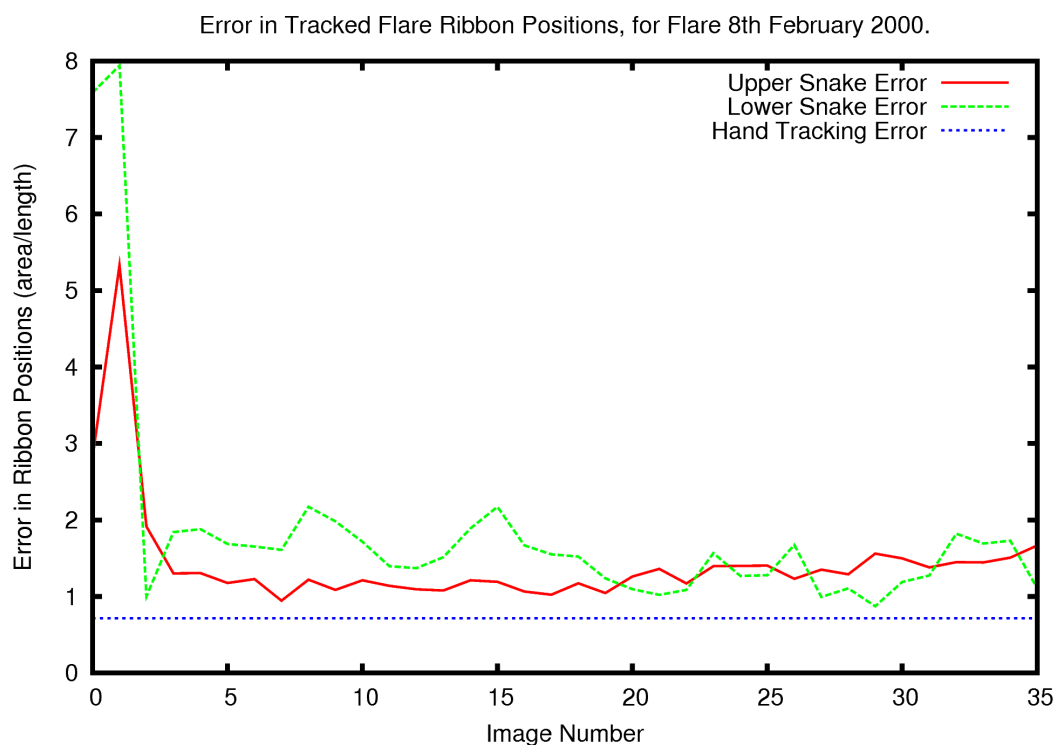
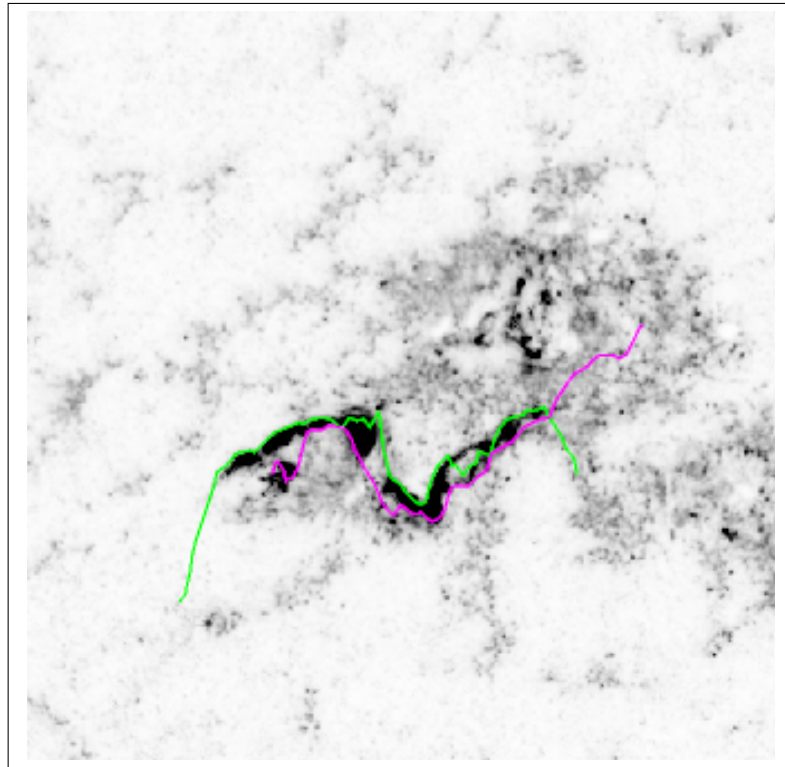
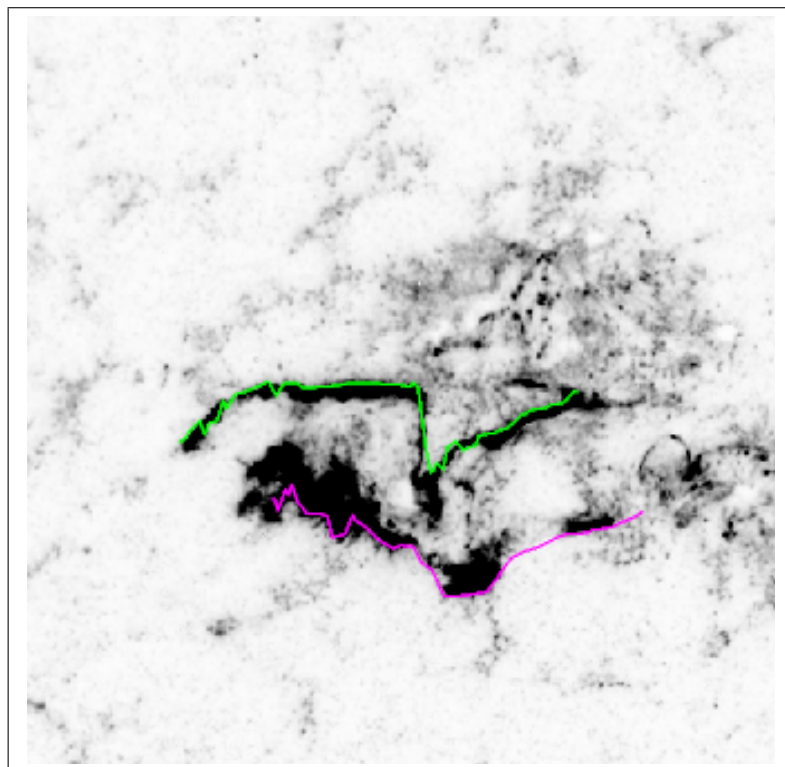


Figure 4.46: Graph showing the error in the upper and lower snake in tracking the upper and lower ribbon for images from the 8th February 2000 flare image sequence. The parameters used for these results are: upper snake - cont = 1.0, curv = 1.0, pressure = 9.0, grad = 1.06, ints = 0.0; lower snake - cont = 1.0, curv = 1.0, pressure = 7.0, grad = 1.6, ints = 0.0. For both snakes  $\sigma = 3.7$ .

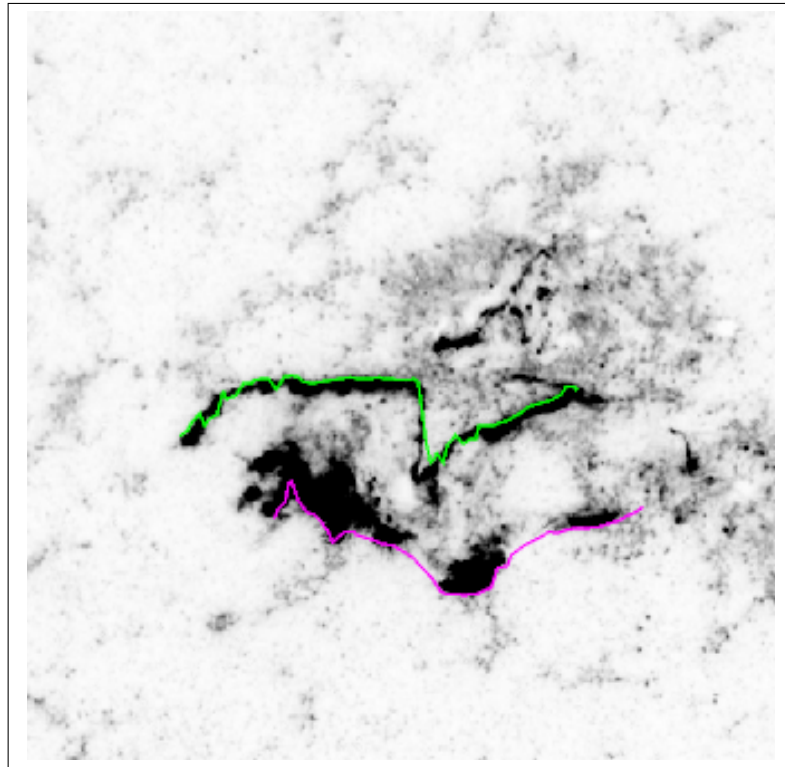


(a)

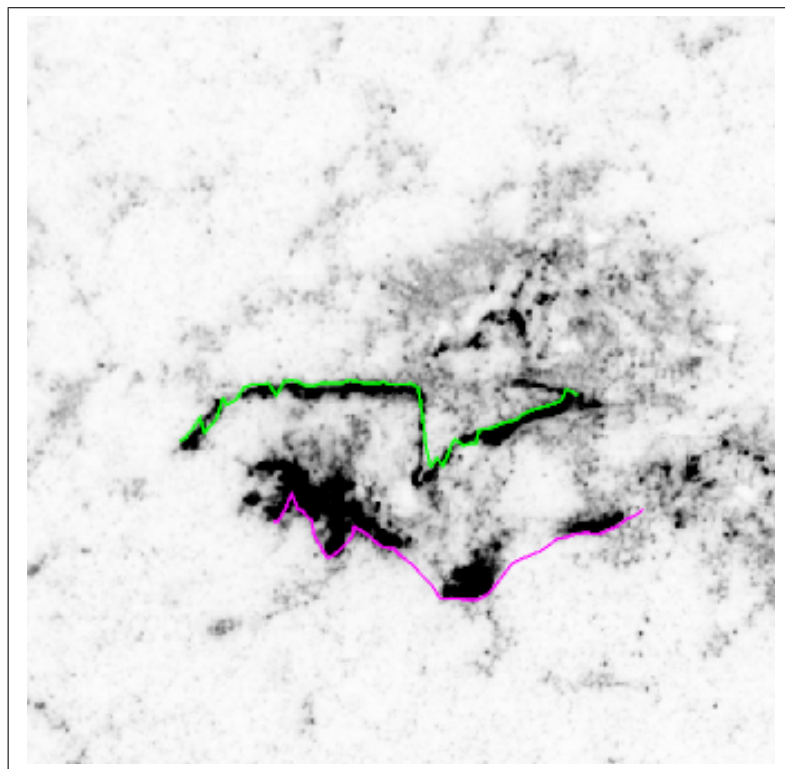


(b)

Figure 4.47: Images showing the tracked ribbon positions for images from the 8th February 2000 flare. Image (a) no. 000, (b) no. 005. The parameters used for these results are: upper snake - cont = 1.0, curv = 1.0, pressure = 9.0, grad = 1.06, ints = 0.0; lower snake - cont = 1.0, curv = 1.0, pressure = 7.0, grad = 1.6, ints = 0.0. For both snakes  $\sigma = 3.7$ .

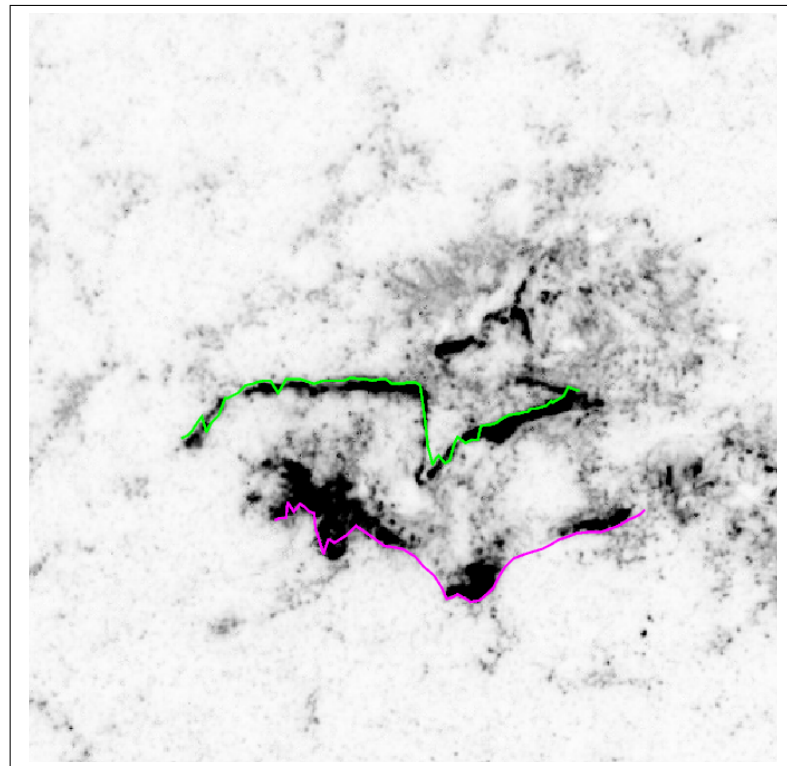


(a)

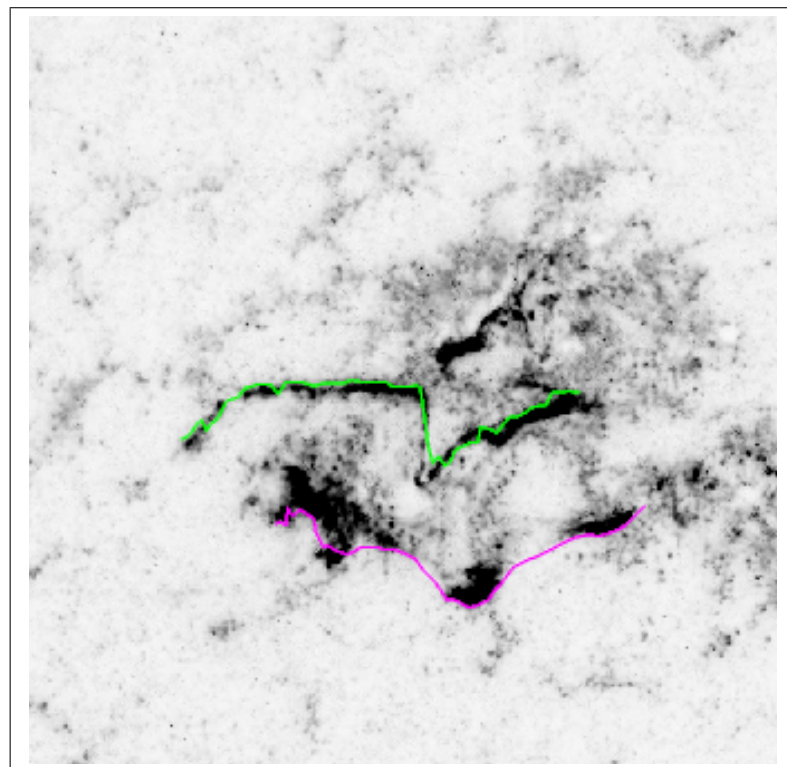


(b)

Figure 4.48: Images showing the tracked ribbon positions for images from the 8th February 2000 flare. Image (a) no. 010, (b) no. 015. The parameters used for these results are: upper snake - cont = 1.0, curv = 1.0, pressure = 9.0, grad = 1.06, ints = 0.0; lower snake - cont = 1.0, curv = 1.0, pressure = 7.0, grad = 1.6, ints = 0.0. For both snakes  $\sigma = 3.7$ .

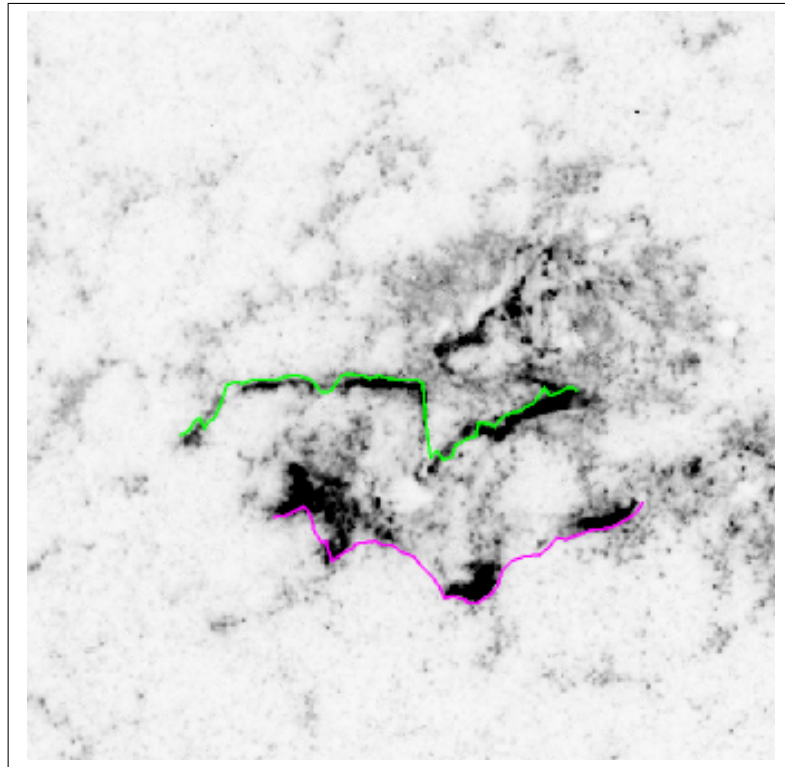


(a)

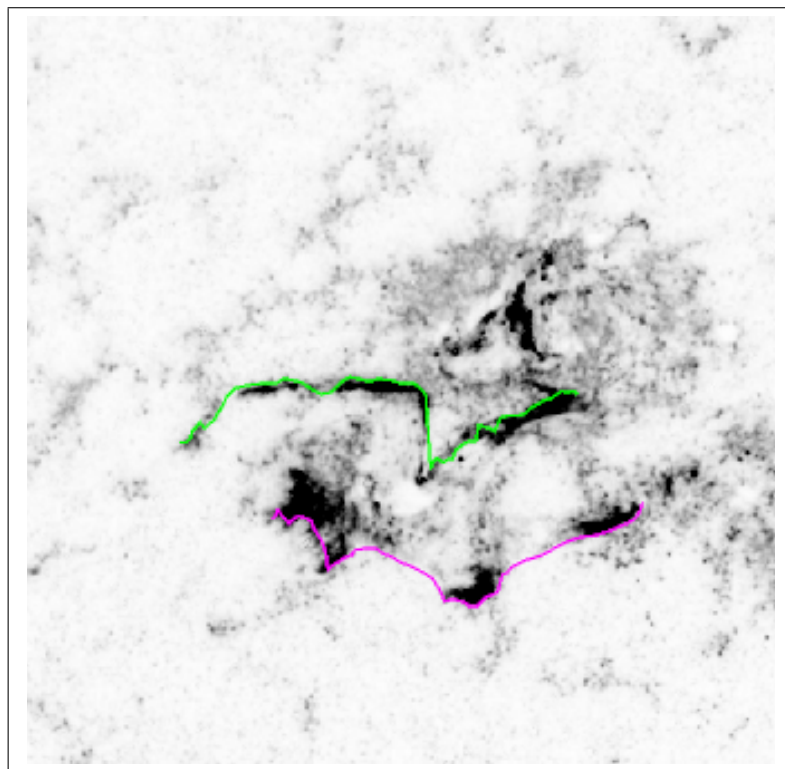


(b)

Figure 4.49: Images showing the tracked ribbon positions for images from the 8th February 2000 flare. Image (a) no. 020, (b) no. 025. The parameters used for these results are: upper snake - cont = 1.0, curv = 1.0, pressure = 9.0, grad = 1.06, ints = 0.0; lower snake - cont = 1.0, curv = 1.0, pressure = 7.0, grad = 1.6, ints = 0.0. For both snakes  $\sigma = 3.7$ .



(a)



(b)

Figure 4.50: Images showing the tracked ribbon positions for images from the 8th February 2000 flare. Image (a) no. 030, (b) no. 035. The parameters used for these results are: upper snake - cont = 1.0, curv = 1.0, pressure = 9.0, grad = 1.06, ints = 0.0; lower snake - cont = 1.0, curv = 1.0, pressure = 7.0, grad = 1.6, ints = 0.0. For both snakes  $\sigma = 3.7$ .

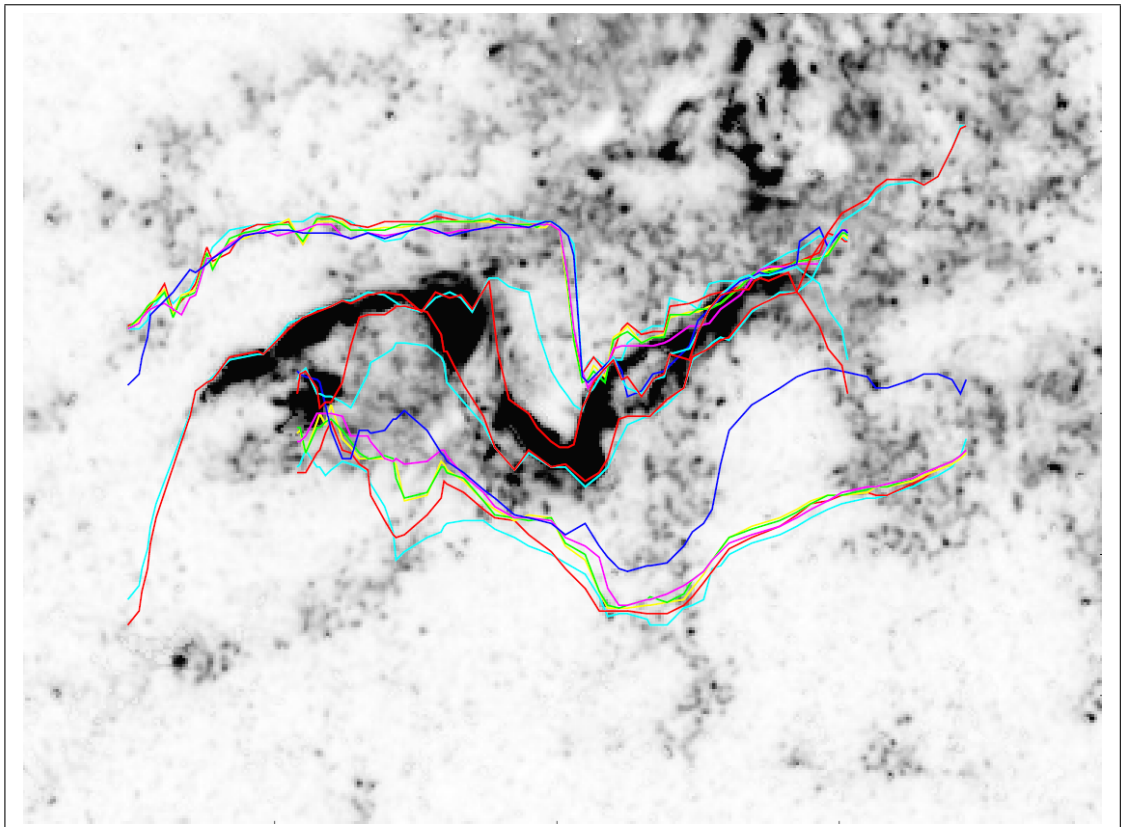


Figure 4.51: The first image of the 8th February 2000 flare sequence, with the tracked ribbon positions for images numbered 0, 1, 2, 3, 4, 5, 15 and 35 shown in red, cyan, blue, pink, green, yellow, red and cyan respectively. The red and cyan lines closest to the outside of the image are from image number 15 and 35. The parameters used for these results are: upper snake - cont = 1.0, curv = 1.0, pressure = 9.0, grad = 1.06, ints = 0.0; lower snake - cont = 1.0, curv = 1.0, pressure = 7.0, grad = 1.6, ints = 0.0. For both snakes  $\sigma = 3.7$ .

#### 4.4.7 Image Characteristics that Affect the Parameters Used

The parameters of the algorithm used for each flare are summarised in Table 4.2, with the exception of  $\sigma$ , these parameters are the relative weights applied to the individual energy sub-functions. For ease the weights are listed relative to the weight for the “cont” sub-function. The different values of  $\sigma$  used for the different flares are all within a relatively small range from 3.0 to 3.7, suggesting that the scale of the structure of the ribbons is not too different from flare to flare. This also strongly makes the case for starting with a LoG  $\sigma$  value in this range for any future work with new flare data with this algorithm. The range of values for  $\sigma$  here is much smaller than the range of values used for finding the ribbons in the last image of each flare, see Table 4.1. This is because the  $\sigma$  values here must suit all images in the image sequence reasonably well, where as the  $\sigma$  values from Table 4.1 can be tailored to one image. Of the six flares, only one flare used a weighting of zero for the pressure parameter, in all other flares at least one of the two snakes used a non-zero weighting for the pressure parameter. It is significant that the flare which used a zero weighting for both snakes was the 14th July 2000 flare, as the images for this flare were taken in the 195 Å passband and were devoid of network emission. In the images of the other flares taken in the 1600 Å passband, the emission from the network resulted in edge images with pixels from the network as well as the flare ribbons. The pressure sub-function of the snake was therefore required to “push” the snake over the weaker pixels in the edge image from the network. Where the pressure weighting was set to zero for individual snakes run on flare images in the 1600 Å passband, the ribbon being sought was sufficiently devoid of strong surrounding ribbon emission. The wide spread of the relative weighting of the “cont =”, “curv”, “pressure”, “grad” and “ints” parameters reflects the variation in the ribbons from different flares. For example, in images of the 12th November 1999 the flare ribbons appear very strong and are very complicated in structure, therefore the “grad” and “ints” parameters are much greater than for the “cont” and “curv” parameters as large “cont” and “curv” parameters would prevent the snake from deforming to the complicated structure of the ribbons. In most cases there is some correlation between the weights for the upper and lower snake of the same flare, which relates to the overall characteristics of the flare and images in question, e.g. how big is the flare, how bright do the ribbons appear relative to the background, is there strong network emission. The difference between parameter weights for different snakes used on the same flare is due to the differences in the ribbons, e.g. one ribbon may have a more complex contorted structure than the other, or one ribbon may appear thicker than the other. It is also possible to observe that the more energetic flares, based on the GOES classification, generally correspond to a

Flare	$\sigma$	Cont	Curv	Pressure	Grad	Ints	Snake	GOES class
20th Jan 2001	3.5	1.0	1.0	5.54	0.834	0.834	Upper	M7.7
20th Jan 2001	3.5	1.0	1.0	5.31	0.625	0.625	Lower	M7.7
14th Jul 2000	3.0	1.0	1.0	0.0	0.250	0.250	Upper	X5.7
14th Jul 2000	3.0	1.0	1.0	0.0	0.219	0.219	Lower	X5.7
10th Apr 2001	3.0	1.0	0.10	0.0	0.080	0.0	Upper	X2.3
10th Apr 2001	3.0	1.0	0.40	7.0	1.20	0.0	Lower	X2.3
25th Jun 2000	3.0	1.0	0.8	18.0	16.0	1.0	Upper	M1.9
25th Jun 2000	3.0	1.0	3.0	0.0	0.156	0.0	Lower	M1.9
12th Nov 1999	3.5	1.0	1.0	7.14	2.86	0.286	Upper	M1.7
12th Nov 1999	3.5	1.0	1.0	7.50	2.50	0.0	Lower	M1.7
8th Feb 2000	3.7	1.0	1.0	9.0	1.06	0	Upper	M1.3
8th Feb 2000	3.7	1.0	1.0	7.0	1.6	0	Lower	M1.3

Table 4.2: Table showing the parameters used for the snake algorithm for different flares. The parameters cont, curv, pressure, grad and int are the relative weightings applied to the continuity, curvature, pressure, image gradient and image intensity sub-functions. For easy comparison these weights are shown relative to the weighting of the cont parameter. The  $\sigma$  parameter is the value of sigma used in the LoG filter.

higher “grad” parameter. This can be explained by linking a more energetic flare with flare ribbons which appear in higher contrast with the chromospheric network and therefore appear clear and well defined in images. The more well defined the ribbons appear in the images the less the model sub-functions are needed to produce a good snake result, hence the observed relationship between more energetic flares and a higher “grad” parameter.

## 4.5 General Rules for Application

The following forms some guidelines for the application of our algorithm for finding flare ribbons. First select an appropriate Log  $\sigma$  value, finding a value that reduces the edges from other sources as much as possible without losing important detail from the ribbons, or blurring away sections of the ribbons. The simulated annealing temperatures should be set so that both snakes can get close to their respective ribbons. The weight of the pressure sub-function can be increased to push the snakes over weaker edges close to the ribbons (at large distances from the ribbons SA should be used to do this), or decreased if the ribbon edges appear faint and the snake is being pushed over them. The relative weighting of the model and data functions can be changed to influence the final fit of the snake to the ribbon. Generally where a ribbon is well defined in the edge image the data function can be weighted higher, but where the ribbon edge is not so well defined, or has gaps, the model function will be increasingly required to impart some rigidity on the snake.

The model function should not be weighted too highly, such that the snake comes to rest as it forms an optimal shape rather than finding the flare ribbons. The intuitive adjustment of the snake parameters to find a suitable parameter set in this way was found to be quicker than a systematic approach trialling a number of combinations of different parameter values.

## 4.6 Summary

In this chapter we have presented the results from the snake algorithm on a number of image sequences from different flares. We have qualitatively and quantitatively examined the performance of the snake algorithm on these images, and outlined particular features that present a problem for the algorithm. In the final chapter, we draw some conclusions from these results, and discuss to what extent we have achieved the initial goal of producing an autonomous algorithm for tracking flare ribbons in UV and EUV TRACE images.

All flare images analysed are saved with the snake results overlaid as .eps files on a CD included with this thesis and can also be found online at <http://www.astro.gla.ac.uk/users/cg9v/>.

# Chapter 5

## Discussion and Conclusions

### 5.1 Was the Aim Accomplished?

The aim of this project was to produce a software tool to enable the automated tracking of solar flare ribbons. The snake algorithm produced has not met the goal of full automation, as user intervention is required for a number of key tasks, such as defining the  $x$  coordinates for the ends of the snakes, and adjusting the algorithms parameters to produce a reasonable result. These tasks are fundamental to achieving any sensible tracking result with the algorithm. The task of adjusting the parameters of the algorithm requires a user to check all the results of the algorithm, and reapply it if necessary. This checking further undermines the aim of automation.

Although not implicitly stated as our aim, the accuracy of the algorithm was intended to be comparable to manually tracking methods. This has been achieved for some of the flares tested in Chapter 4, but for others the accuracy of the algorithm's result was far from that achievable by manual methods. Where the flare ribbons are simple in structure the algorithm produces an accurate result, see Figure 4.16, but where the ribbons are more complex in nature the accuracy of the algorithm is substantially reduced, see Figure 4.42. A useful comparison would be with the results from another automated algorithm on the same flare data, but unfortunately this has not been possible.

The more encouraging of the results from Chapter 4 suggest that there is some potential for the use of active contours for tracking solar flare ribbons. For many images the algorithm has met the benchmark detailed in Section 4.2. However the problems outlined in Section 5.2 would need to be addressed before such an algorithm could be successfully employed for automated or semi-automated processing of flare images.

## 5.2 Problems Encountered

Of the problems encountered applying the snake algorithm, one of the most fundamental is in correctly determining the range of  $x$  coordinates over which to initialise the snake, referred to as the “truncation of the snake” in Section 3.2.6. Both the initial methods discussed in Section 3.2.6, and the alternative semi-automated approach discussed in Section 4.1 failed to accurately perform this task. Any future application of active contours for this application should address this issue first and foremost.

Another of the principal drawbacks of the snake algorithm approach is the need to fine tune the algorithm’s parameters for the different flares. As demonstrated in Section 4.3.1, changing the parameters of the algorithm can vastly change the resulting final positions of the snakes. If the search for suitable parameters becomes the lengthy “circular trial and error approach” as described by Xu et al. (1994), the whole benefit of using the algorithm is negated and one labour intensive time consuming task is simply swapped for another. The key to avoid these circumstances is producing an edge image where the ribbons appear strong and clearly defined with as little noise from other sources as possible. A set of good default parameters applicable to different flares would also help avoid this scenario; although as the parameters reflect the different properties of the images and the flare ribbons, and these properties are extremely diverse, there is unlikely to be such a set of parameters applicable to a wide range of different flares. It is also the case that some parameters suit some of the images in the sequence, but not all, and also that some parameters may suit parts of the ribbons in an image but not others. An example of this is the LoG  $\sigma$  parameter, where for most of a ribbon a high value for  $\sigma$  is suitable, but for a thinner part of the ribbon the high value of  $\sigma$  blurs the ribbon into the background. This example can also be applied to different images in a sequence, where the ribbons may appear thick and strong in some images, but appear fainter and thinner in others, in this case using one value for the LoG  $\sigma$  parameter produces a compromise rather than an optimal result.

Another of the limitations of the algorithm is its inability to move into concave regions of the flare ribbons, this is seen in the results from the 8th of February flare in Section 4.3.6. A solution to this problem is discussed in Section 5.4.

Many of the larger errors in the snake tracking reported in Chapter 4 were the result of ribbons that did not appear as one coherent structure. This occurred where the ribbon either splits into parallel sections (bifurcation), see Figures 4.16 and 4.42, or there appears separate areas of emission, see Figures 4.41 and 4.50. It is not always apparent what the ideal behaviour of the algorithm should be in these circumstances. Future approaches to this problem need to determine a set of

rules to summarise the ideal behaviour of an automated tracking algorithm in these situations, and then seek to implement this behaviour in the algorithm.

Where features in the edge image appear close to the edge of a ribbon, it is possible that nodes of the snake will move off the ribbon edge and onto the other edge feature, if the maximum distance that the nodes can travel in one iteration is equal to or greater than the distance between the edge of the ribbon and the other edge feature. As a result nodes of the snake can be seen to move onto other ribbons when they are close by, or onto the edges of flare loops.

Similar automated solar feature tracking algorithms have the benefit of large manually compiled catalogues recording the evolution of the tracked features, i.e. the CDAW catalogue for CMEs that is used for comparison with a CME automated detection and tracking algorithm in (Olmedo et al. 2008). The absence of such catalogues for solar flare ribbons presents a considerable barrier to the verification of an automated ribbon tracking algorithm over large datasets.

### 5.3 Different TRACE Passbands

The fundamental differences between flare images in the TRACE 1600 Å and 195 Å passbands were thought to require a different approach, but as discussed in Section 4.4.2, the alternative approach to edge image production trialled produced a tracking result that appeared both qualitatively and quantitatively worse than the result using the standard edge image method. The appearance of bright loop emission in the 195 Å images means that the flare ribbons can appear as fainter edges in the edge images, and that the ribbon edges are likely to appear as the outermost edges in the edge image. An edge image where pixel values indicate they either belong to an edge or do not belong to an edge, rather than pixel values that have a grey level value that shows how strong the edge is, was thought to be advantageous for use with 195 Å images. In reality rather than producing an algorithm where the snake is more likely to settle on the first edge it comes to in the image (i.e. the flare ribbons), this method meant that the snake could move to any edge pixel in the image without altering its data energy and therefore the snake settled along edge pixels that lay in a roughly straight line (i.e. represented a minimum configuration for the model energy function). Whilst the particular alternative approach trialled was not a success, it is likely that a different alternative approach to 195 Å images could produce a more accurate tracking algorithm, but we are unable to conclude from the work carried out for this thesis what this different approach should be.

## 5.4 Future Work and Improvements

Many of the issues with the snake algorithm are a result of images containing features other than the flare ribbons, an issue which is not likely to be resolved at image capture for solar flare monitoring instruments. However big improvements to the snake algorithm could be made with additional pre-processing steps to reduce the other features present in the images (i.e. flare loops and chromospheric network), prior to establishing the ribbon positions.

The use of running difference images, which are formed by subtracting one image from the next, could be just such a pre-processing step to reduce other features in the images. These were intended to be used in this algorithm, but unfortunately this did not get suitably tested or implemented because of time constraints. The aim of implementing such images is to significantly reduce the appearance of network in the 1600 Å images, the only danger being that if the ribbons do not move sufficiently between images, they will be removed along with the network.

One of the more simple improvements for this algorithm would need to be made if it were to be applied autonomously. The images from the flares on the 10th April 2001, and the 25th June 2000 were rotated so that the ribbons lay roughly horizontal, ensuring that the motion of the snakes was perpendicular to the flare ribbons. This was carried out external to the algorithm, with the amount of rotation determined manually. This process could be automated by using the edge orientation information output from a Sobel edge detection filter. The resulting edge image from the Sobel edge detector could be thresholded to leave only the strongest edge pixels, the mean angle at the edge pixels can then be calculated to give an approximation of the ribbons orientation and the images rotated accordingly. This method would not work with the 195 Å TRACE images, as strong edges also appear due to the flare loops, and these edges are usually at right angles to the ribbon edges.

As the snake algorithm relies heavily on the edge image, it is possible to make improvements to the algorithm by improving the edge detection. One way in which this could be achieved is with the use of a method to link discontinuous edges, such as the canny edge detection method. It may also be advantageous to perform the thresholding of the edge image with an adaptive or regional threshold rather than a global threshold. This will retain edges that represent a large local image gradient that may appear weak in the global context. Where flare ribbons appear weaker in places this method could prevent these sections from appearing as gaps in the edge image. Such a development would need to be made carefully to ensure that more edges from the network in 1600 Å images do not appear in the edge image as a result.

The Gradient Vector Flow (GVF) snake development was discussed briefly in

Section 2.1.3 as a solution to the initialisation and concavity problems associated with snakes. Although the initialisation problem is mitigated with the use of the pressure function for our snake algorithm, the issue of snakes moving into concave regions of the flare ribbons remains a problem. By implementing a GVF snake algorithm this issue may be resolved, but perhaps equally importantly the sensitivity of the snake to its parameters could be reduced (Xu & Prince 1998).

Future work is needed to resolve the issue of snake truncation. This may be achieved with further experimentation with the current method described in Section 4.1. This current method fails due to the large number of weaker edge pixels present in the edge image that appear outside of the  $x$  coordinate range of the ribbons. These edge pixels appear in the image columns immediately inside the outer limits set by the user, and hence the algorithm does not reduce the limits of the snake further (refer back to Section 4.1). Producing a secondary edge image that has a higher threshold can reduce these weak edge pixels, and so allow the algorithm to reduce the outer limits for the snakes. Other approaches to this problem could use thresholding and region growing in the original image or the edge image, but in these cases the process of defining the outer limits for the snake start to appear in the early stages of ribbon detection, as in Saba et al. (2006) and Qu et al. (2004b).

The information that is available with the TRACE images includes the time that the images were captured. This information could be used together with the difference in ribbon positions to calculate an estimate of the ribbon's velocity, which could then be used to predict the position of the ribbon in following images. This may be particularly useful where the ribbons have moved by a large amount between images. Although this is not a major problem with our algorithm, as the pressure function pushes the snakes onto the ribbons when they have moved by large amounts, this may provide an improved result.

Qu et al. (2004b) use both edge based and region based image segmentation methods together in their approach to flare ribbon tracking, this seems to be a good idea. The possible drawback is computation time, but provided any computational cost is acceptable it would seem sensible to use both approaches to the problem. The crux of their method is to use the region based methods to establish the positions of the flare ribbons, and then use the edge based methods to determine the borders of the flare ribbons, thus neatly utilising the strengths for flare images of both approaches. It is possible for a similar approach using snakes as the edge based method.

The final recommendation for future work concerns the creation of the default parameter set for the algorithm. The trial and error method employed here produced a reasonable result and fitted into the development stages of this project. A more rigorous approach to producing a default set of parameters could use a large dataset

of flares, provided a suitable goodness of fit measure is available. The problem of finding the optimum parameters can then be approached as an optimisation problem using methods such as simulated annealing or genetic algorithms.

## 5.5 Summary

The use of snakes (active contours) for tracking solar flare ribbons in UV and EUV images has been shown to be possible. We have shown that given the right conditions our algorithm is able to track flare ribbons over a sequence of images with an accuracy comparable to manual tracking methods. The extent to which this approach lends itself to full automation remains to be seen, with a number of significant problems needing to be addressed before such an algorithm can be used in a fully autonomous nature. A semi-automated approach may be a more realistic goal for this type of algorithm in the short term, with a fully automated approach possibly using a number of different image processing methods for accomplishing certain key tasks.

With the imminent launch of NASA's SDO (Campion & Pruettt 2009), vast volumes of high spatial and temporal resolution data will soon be available to the solar research community. Algorithms such as the one whose development is detailed in this thesis will be crucial to extracting the maximum amount of scientific information from this data.

# Bibliography

- Abouadarham, J., Scholl, I., Fuller, N., et al. 2008, *Annales Geophysicae*, 26, 243
- Anon. 2009a, SDO, Solar Dynamics Observatory, Mission Overview, [http://sdo.gsfc.nasa.gov/epo/101/mission/mission\\_overview.php](http://sdo.gsfc.nasa.gov/epo/101/mission/mission_overview.php)
- Anon. 2009b, Solar Image Processing, <http://www.sipwork.org>
- Asai, A., Yokoyama, T., Shimojo, M., Masuda, S., & Shibata, K. 2006, *Journal of Astrophysics and Astronomy*, 27, 167
- Aschwanden, M. J. 2004, *Physics of the Solar Corona. An Introduction (Physics of the Solar Corona)*
- Aschwanden, M. J., Hudson, H., Kosugi, T., & Schwartz, R. A. 1996a, *Astrophys. J.* , 464, 985
- Aschwanden, M. J. & Schwartz, R. A. 1995, *Astrophys. J.* , 455, 699
- Aschwanden, M. J., Schwartz, R. A., & Alt, D. M. 1995, *Astrophys. J.* , 447, 923
- Aschwanden, M. J., Wills, M. J., Hudson, H. S., Kosugi, T., & Schwartz, R. A. 1996b, *Astrophys. J.* , 468, 398
- Benz, A. O. 1993, *Plasma Astrophysics: Kinetic Processes in Solar and Stellar Coronae (Kulwer Academic Publishers)*
- Bernasconi, P. N., Rust, D. M., & Hakim, D. 2005, *Solar Phys.* , 228, 97
- Brodrick, D., Tingay, S., & Wieringa, M. 2005, *Journal of Geophysics*, 110
- Brown, J. C. 1973, *Solar Phys.* , 31, 143
- Brown, J. C., Karlicky, M., MacKinnon, A. L., & van den Oord, G. H. J. 1990, *Astrophys. Suppl.* , 73, 343
- Brown, J. C., Spicer, D. S., & Melrose, D. B. 1979, *Astrophys. J.* , 228, 592

- Campion, E. & Pruet, A. 2009, NASA's Solar Dynamics Observatory Arrives at Kennedy Space Center, [http://www.nasa.gov/mission\\_pages/sdo/news/sdo\\_arrival.html](http://www.nasa.gov/mission_pages/sdo/news/sdo_arrival.html)
- Carmichael, H. 1964, in *The Physics of Solar Flares*, ed. W. N. Hess, 451–+
- Chapman, G. A., Cookson, A. M., & Hoyt, D. V. 1994, *Solar Phys.* , 149, 249
- Chapman, G. A. & Groisman, G. 1984, *Solar Phys.* , 91, 45
- Cohen, L. 1991, 53, 211
- Colak, T. & Qahwaji, R. 2008, *Solar Phys.* , 248, 277
- Conlon, P. A., Gallagher, P. T., McAteer, R. T. J., et al. 2008, *Solar Phys.* , 248, 297
- Curto, J., Blanca, M., & Sol, J. 2003, in *Solar Image Recognition Workshop*
- Czaykowska, A., Alexander, D., & De Pontieu, B. 2001, *Astrophys. J.* , 552, 849
- Davatzikos, C. & Prince, J. 1995, *Medical Imaging, IEEE Transactions on*, 14, 65
- Davies, E. R. 2005, *Machine Vision; theory, algorithms, practicalites*, 3rd edn. (Elsevier)
- Delouille, V., de Patoul, J., Hochedez, J. F., Jacques, L., & Antoine, J. P. 2005, *Solar Phys.* , 228, 301
- Dennis, B. R. & Schwartz, R. A. 1989, *Solar Phys.* , 121, 75
- Emslie, A. G. & Brown, J. C. 1985, *Astrophys. J.* , 295, 648
- Feldman, U., Landi, E., & Schwadron, N. A. 2005, *Journal of Geophysical Research (Space Physics)*, 110, 7109
- Fletcher, L. & Hudson, H. 2001, *Solar Phys.* , 204, 69
- Fletcher, L. & Hudson, H. S. 2008, *Astrophys. J.* , 675, 1645
- Fletcher, L., Pollock, J. A., & Potts, H. E. 2004, *Solar Phys.* , 222, 279
- Freeland, S. L. & Handy, B. N. 1998, *Solar Phys.* , 182, 497
- Gallagher, P. T., McAteer, R. T. J., Young, C. A., et al. 2007, in *Astrophysics and Space Science Library*, Vol. 344, *Space Weather : Research Towards Applications in Europe 2nd European Space Weather Week (ESWW2)*, ed. J. Liliensten, 15–+

- Gallagher, P. T., Moon, Y.-J., & Wang, H. 2002, *Solar Phys.* , 209, 171
- Gao, J., Wang, H., & Zhou, M. 2002, *Solar Phys.* , 205, 93
- Golub, L., Bookbinder, J., Deluca, E., et al. 1999, *Physics of Plasmas*, 6, 2205
- Gonzalez, R. C. & Woods, R. E. 2007, *Digital Image Processing*, 3rd edn. (Pearson Prentice Hall)
- Handy, B. N., Acton, L. W., Kankelborg, C. C., et al. 1999, *Solar Phys.* , 187, 229
- Henoux, J. C. & Rust, D. 1980, *Astron. Astrophys.* , 91, 322
- Hewett, R. J., Gallagher, P. T., McAteer, R. T. J., et al. 2008, *Solar Phys.* , 248, 311
- Hirayama, T. 1974, *Solar Phys.* , 34, 323
- Hori, K., Yokoyama, T., Kosugi, T., & Shibata, K. 1997, *Astrophys. J.* , 489, 426
- Hurlburt, N. E., Cheung, M., Schrijver, K., & HEK development team. 2009, in *AAS/Solar Physics Division Meeting*, Vol. 40, *AAS/Solar Physics Division Meeting*, 15.11–+
- Kass, M., Witkin, A., & Terzopoulos, D. 1988, *International Journal of Computer Vision*, 321
- Kirkpatrick, S., Gelatt, C. D., & Vecchi, M. P. 1983, 220, 671
- Kopp, R. A. & Pneuman, G. W. 1976, *Solar Phys.* , 50, 85
- Kurokawa, H. 1989, *Space Science Reviews*, 51, 49
- Leighton, R. B., Noyes, R. W., & Simon, G. W. 1962, *Astrophys. J.* , 135, 474
- Leroy, B., Herlin, I., & D., C. L. 1996, in *12th International Conference on Analysis and Optimization of Systems*, 58–65
- Marshall, S., Fletcher, L., & Hough, K. 2006, *Astron. Astrophys.* , 457, 729
- Martens, P. C., Angryk, R. A., Bernasconi, P. N., et al. 2009, in *AAS/Solar Physics Division Meeting*, Vol. 40, *AAS/Solar Physics Division Meeting*, 17.11–+
- Menet, S., Saint-Marc, P., & Medioni, G. 1990, *Systems, Man and Cybernetics*, 1990. *Conference Proceedings*, IEEE International Conference on, 194
- Michalitsanos, A. G. & Kupferman, P. 1974, *Solar Phys.* , 36, 403

- Olmedo, O., Zhang, J., Wechsler, H., Poland, A., & Borne, K. 2008, *Solar Phys.* , 248, 485
- Parker, E. N. 1963, *Astrophys. Suppl.* , 8, 177
- Paton, L., Cirtain, J., & Grant, P. 2008, in *Society of Photo-Optical Instrumentation Engineers (SPIE) Conference Series*, Vol. 7019, *Society of Photo-Optical Instrumentation Engineers (SPIE) Conference Series*
- Petschek, H. E. 1964, in *The Physics of Solar Flares*, ed. W. N. Hess, 425–+
- Preminger, D. G., Walton, S. R., & Chapman, G. A. 2001, *Solar Phys.* , 202, 53
- Qiu, J., Lee, J., Gary, D. E., & Wang, H. 2002, *Astrophys. J.* , 565, 1335
- Qu, M., Shih, F., Jing, J., & Wang, H. 2004a, in *Bulletin of the American Astronomical Society*, Vol. 36, *Bulletin of the American Astronomical Society*, 760–+
- Qu, M., Shih, F., Jing, J., & Wang, H. 2004b, *Solar Phys.* , 222, 137
- Qu, M., Shih, F. Y., Jing, J., Denker, C., & Wang, H. 2005, *AGU Spring Meeting Abstracts*, A6+
- Revathy, K., Lekshmi, S., & Nayar, S. R. P. 2005, *Solar Phys.* , 228, 43
- Robbrecht, E. & Berghmans, D. 2004, *Astron. Astrophys.* , 425, 1097
- Robbrecht, E., Berghmans, D., & van der Linden, R. A. M. 2006, *Advances in Space Research*, 38, 475
- Robbrecht, E., Berghmans, D., & Van der Linden, R. A. M. 2009, *Astrophys. J.* , 691, 1222
- Saba, J. L. R., Gaeng, T., & Tarbell, T. D. 2006, *Astrophys. J.* , 641, 1197
- Sakao, T. 1994, PhD thesis, (University of Tokyo), (1994)
- Scholl, I. F. & Habbal, S. R. 2008, *Solar Phys.* , 248, 425
- Schrijver, C. J. & Tarbell, T. D. 2004
- Schrijver, C. J., Title, A. M., Berger, T. E., et al. 1999, *Solar Phys.* , 187, 261
- Shih, F. Y. & Kowalski, A. J. 2003, *Solar Phys.* , 218, 99
- Simon, G. W. & Leighton, R. B. 1964, *Astrophys. J.* , 140, 1120
- Smith, D. F. & Lilliequist, C. G. 1979, *Astrophys. J.* , 232, 582

- Steinegger, M., Brandt, P. N., Schmidt, W., & Pap, J. 1990, *Astrophys. Spa. Sci.* , 170, 127
- Stenborg, G. & Cobelli, P. J. 2003, *Astron. Astrophys.* , 398, 1185
- Stix, M. 2004, *The Sun* (Springer)
- Sturrock, P. A. 1966, *Nature*, 211, 695
- Sturrock, P. A., Kaufman, P., Moore, R. L., & Smith, D. F. 1984, *Solar Phys.* , 94, 341
- Su, Y. N., Golub, L., van Ballegooijen, A. A., & Huang, G. L. 2006, in *IAU Symposium*, Vol. 233, *Solar Activity and its Magnetic Origin*, ed. V. Bothmer & A. A. Hady, 409–410
- Svestka, Z. 1976, *Solar Flares* (Solar Flares. Svestka, Z., pp. 415. ISBN 90-277-0662-X. Springer-Verlag Berlin Heidelberg 1976)
- Tandberg-Hanssen, E. & Emslie, G. 1988, *The Physics of Solar Flares* (Cambridge University Press)
- Tek, H. & Kimia, B. 1995, *Computer Vision, 1995. Proceedings., Fifth International Conference on*, 156
- Wang, H., Qiu, J., Jing, J., & Zhang, H. 2003, *Astrophys. J.* , 593, 564
- Warren, H. P. 2001, *AGU Spring Meeting Abstracts*, 42
- Williams, D. J. & Shah, M. 1990, in *Third International Conference on Computer Vision, Proceedings*, 592–595
- Xu, C. & Prince, J. 1998, *Image Processing, IEEE Transactions on*, 7, 359
- Xu, G., Wa, E., & S., T. 1994, *Pattern Recognition*, 27, 879
- Zharkov, S., Zharkova, V. V., & Ipson, S. S. 2005, *Solar Phys.* , 228, 377
- Zirin, H. 1988, *Astrophysics of the Sun* (Cambridge University Press)